Passively Mode-Locked Tm-Lasers for All-Fiber High-Energy Nonlinear Chirped Pulse Amplification

A thesis accepted by the Faculty of Aerospace Engineering and Geodesy of the University of Stuttgart in fulfilment of the requirements for the degree of Doctor of Natural Sciences (Dr. rer. nat.)

by
Florian Graf
born in
Freudenstadt, Germany

Main referee:	Prof. Dr. rer. nat. Thomas Dekorsy
Co-referee:	Prof. Dr. rer. nat. Marc Eichhorn
Day of the exam:	23.06.2023

Institute of Aerospace Thermodynamics (ITLR)
University of Stuttgart

2023

Contents

Abstract **6**

Kurzzusammenfassung **8**

1 Introduction **10**

2 Concepts of Ultrashort Pulse Propagation in Optical Fibers **13**

2.1 The Optical Fiber as Dielectric Waveguide 13

2.2 Properties of Thulium-Doped Fibers as Active Medium 16

2.2.1 Energy Level Structure and Transfer Processes 17

2.2.2 Rate Equation Based Calculation of Laser Amplification 18

2.2.3 Determination of the Heat Load and Temperature Along the Fiber 22

2.3 Pulse Propagation in Optical Fibers 23

3 Concepts of Fiber-Based Generation and Amplification of Ultrashort Optical Pulses **27**

3.1 Locking of Longitudinal Resonator Modes 28

3.2 Saturable Absorbers 30

3.2.1 The Nonlinear Amplifying Loop Mirror as Artificial Saturable Absorber 31

3.3 Survey of Pulse Formation Regimes 42

3.3.1 Soliton Fiber Lasers . . . 42
3.3.2 Dispersion Managed Soliton Fiber Lasers . . . 46
3.3.3 Self-Similar Fiber Lasers . . . 47
3.3.4 Dissipative-Soliton Fiber Lasers . . . 49
3.3.5 Mamyshev Fiber Lasers . . . 49
3.3.6 Conclusions . . . 51
3.4 Modeling the Propagation of Ultrashort Pulses by the Split-Step Fourier Method . . . 52
3.4.1 Modeling of NALMs Incorporating 3x3-Couplers . . . 54
3.5 Nonlinear Chirped Pulse Amplification . . . 55
3.5.1 A Simplified Model for Nonlinear CPA . . . 56
3.5.2 Impact of the Spectral Shape on the Pulse Compressibility . . . 58
3.5.3 Impact of Spectral and Phase Perturbations on the Pulse Contrast 61

4 All-Fiber Lasers Passively Mode-Locked by a 3x3-Coupler-NALM 65
4.1 Thulium Doped Fiber Laser . . . 66
4.1.1 Dispersion Adjustment via cFBG . . . 70
4.1.2 Distributed Dispersion Compensation via cFBG and NDF . . . 74
4.2 Ytterbium Doped Fiber Laser . . . 78
4.2.1 Experimental Results . . . 79
4.3 Conclusion . . . 84

5 Monolithic Nonlinear Chirped Pulse Amplification Based on Thulium Doped Fibers 85
5.1 Experimental Setup . . . 86
5.2 High Pulse Energy Operation . . . 91
5.3 High Average Power Operation . . . 97
5.4 Summary . . . 102

6 Conclusion 104

Bibliography 107

Danksagung (Acknowledgements) 125

Curriculum Vitae 126

List of Abbreviations

ACT Autocorrelation Trace

AND All-Normal Dispersion

APM Additive Pulse Mode-Locking

ASE Amplified Spontaneous Emission

cFBG Chirped Fiber Bragg Grating

CPA Chirped Pulse Amplification

CW Continuous Wave

DC Double-Clad

Er Erbium

GDD Group Delay Dispersion

GVD Group Velocity Dispersion

FROG Frequency Resolved Optical Gating

FWHM Full Width at Half Maximum

Laser Light Amplification by Stimulated Emission of Radiation

MFD Mode Field Diameter

MFA Mode Field Adapter

NA Numerical Aperture

NALM Nonlinear Amplifying Loop Mirror

NDF Normally Dispersive Fiber

NLSE Nonlinear Schrödinger Equation

NOLM Nonlinear Optical Loop Mirror

OSA Optical Spectrum Analyser

PCF Photonic Crystal Fiber

PER Polarisation Extinction Ratio

PM Polarisation Maintaining

PSD Power Spectral Density

QD Quantum Defect

RF Radio Frequency

RPP Relative Peak Power

SC Single-Clad

SESAM Semiconductor Saturable Absorber Mirror

SHG Second Harmonic Generation

SPM Self-Phase Modulation

SRS Stimulated Raman Scattering

SSFM Split-Step Fourier Method

SSFS Soliton Self Frequency Shift

SVEA Slowly Varying Envelope Approximation

Tm Thulium

TOD Third Order Dispersion

TMI Transverse Mode Instabilities

WDM Wavelength Division Multiplexer

Yb Ytterbium

ZPL Zero Phonon Line

Abstract

Ultrashort pulse lasers continue to transform and open up industrial and scientific applications, comprising material processing, metrology, particle acceleration, laser-driven secondary radiation sources among others. In order to satisfy the demands of these ambitious applications, ever-increasing optical peak intensities at large repetition rates as well as stability and reliability are expected from the laser systems. Rare-earth doped glass fibers are widely used for the generation and amplification of the pulses as they offer an inexpensive, robust, and flexible platform with large gain bandwidths. However, as a result of the tight confinement of the pulses in the fiber core, large peak intensities are easily reached, which promotes nonlinear optical effects that are detrimental to the final pulse quality.

This work focuses on the generation as well as the amplification of highly energetic ultrashort pulses in the 2 µm wavelength regime. The first subject is the generation of the pulses in a passively mode-locked all-fiber oscillator that is capable of operation in an industrial environment including mechanical vibrations and fluctuating temperatures. Therefore, an oscillator architecture is proposed, which uses exclusively polarization maintaining components and omits free-space sections that could give rise to misadjustments due to environmental influences. Mode-locking is achieved by a nonlinear amplifying loop mirror that is coupled to the laser resonator via a fused 3x3-coupler. This implementation enables starting of the pulsed operation by simply increasing the pump power and allows for a flexible tuning of the intra-cavity pulse parameters. The concept is realised and studied for Thulium- as well

as Ytterbium-doped systems, allowing for the demonstration of pulse durations as short as 215 fs and 125 fs, respectively. The experimental results are supported by numerical simulations on the basis of an extended nonlinear Schrödinger equation. Moreover, insights obtained by the simulations are used to optimise the oscillators' output spectra towards an employment in a nonlinear chirped pulse amplification setup.

The second subject of this work is the realisation of a monolithic, nonlinear chirped pulse amplification setup based on Thulium-doped fibers, which allows for a study of the peak and average power scalability of the technology. In this setup, low-energy pulses are dispersively stretched to a pulse duration of 650 ps, amplified to a pulse energy of up to 100 µJ and then recompressed again close to the Fourier limit. The monolithic setup prevents the influence of water vapor absorption on the stretched pulse shape prior to the main amplifier and thus largely mitigates the adverse effects of a corresponding peak power reduction during nonlinear amplification. The resulting peak power is approximately 250 MW. A further scaling of the peak power is prevented by the onset of a nonlinear power transfer away from the main pulse. In this setup, the average power scaling is limited to 31 W due to the large thermal load of the 793 nm pumping scheme and insufficient heat removal from the fiber. In a subsequent step, an improved cooling scheme of the main amplifier based on thermally conductive silicone is used, which enables an average output power of 120 W that is limited by the available pump power. The measured amplifier temperature is below 70 °C, which indicates that further scaling of the output power is admissible with this cooling concept, especially when silicones with even larger thermal conductivities are applied.

Kurzzusammenfassung

Ultrakurzpulslaser transformieren und erschließen fortlaufend industrielle und wissenschaftliche Anwendungen in Bereichen wie der Materialbearbeitung, der Metrologie, der Teilchenbeschleunigung oder der Erzeugung von Sekundärstrahlungsquellen. Um diese anspruchsvollen Anwendungen ermöglichen zu können, werden stets wachsende Anforderungen an optische Spitzenleistungen bei hohen Repetitionsraten sowie Stabilität und Zuverlässigkeit der Lasersysteme gestellt. Glasfasern, die zum Zweck der Erzeugung und Verstärkung der Pulse mit seltenen Erden dotiert werden, finden dabei einen breiten Einsatz, da sie eine kostengünstige, robuste sowie flexible Plattform darstellen, die große Verstärkungsbandbreiten bietet. Aufgrund der starken Lokalisierung der Pulse im Faserkern werden jedoch unschwer hohe Spitzenintensitäten erreicht wodurch sich rasch nichtlineare optische Effekte bemerkbar machen, die sich nachteilig auf die finale Pulsqualität auswirken.

In der vorliegenden Arbeit wird die Erzeugung ultrakurzer Pulse im 2 µm Wellenlängenbereich sowie deren Verstärkung hin zu hohen Pulsenergien untersucht. Zur Erzeugung der Pulse werden rein faserbasierte, passiv modengekoppelte Oszillatoren verwendet, die in einer industriellen Umgebung, also unter Einfluss von mechanischen Vibrationen und sich ändernden Umgebungstemperaturen, verwendbar sind. Hierfür wird eine Oszillator-Architektur vorgeschlagen, in der ausschließlich polarisationserhaltende Komponenten Verwendung finden und Freistrahlbereiche, bei denen es unter Umgebungseinflüssen zu Fehljustagen kommen kann, vermieden werden. Die Modenkopplung wird durch eine nichtlineare, verstärkende Faserschlaufe erreicht, die

mittels eines 3x3-Kopplers mit dem Laserresonator verbunden ist. Diese Anordnung erlaubt den Start des gepulsten Betriebs durch schlichtes Erhöhen der Pumpleistung und erlaubt eine flexible Anpassung der Pulsparameter im Resonator. Das Konzept wird sowohl für Thulium- als auch Ytterbium dotierte Systeme realisiert und untersucht, wodurch sich Pulse mit Dauern von 215 fs beziehungsweise 125 fs erzeugen lassen. Die experimentellen Resultate werden durch numerische Berechnungen auf Basis einer erweiterten nichtlinearen Schrödingergleichung unterstützt. Darüberhinaus liefern die Berechnungen Einsichten, die genutzt werden um die Oszillatoren und die sich ergebenden Ausgangsspektren für den Einsatz in einem Aufbau zur nichtlinearen Verstärkung gechirpter Pulse zu optimieren.

Der zweite Gegenstand dieser Arbeit ist die Realisierung eines monolithischen Aufbaus zur nichtlinearen Verstärkung gechirpter Pulse basierend auf Thulium dotierten Fasern, welcher eine Untersuchung der Skalierbarkeit von mittlerer Leistung und Spitzenleistung der Technologie erlaubt. In diesem Aufbau werden Pulse niedriger Energie mittels Dispersion auf eine Pulsdauer von 650 ps gestreckt, auf eine Pulsenergie von 100 µJ verstärkt und anschließend wieder bis nah an das Fourierlimit komprimiert. Der monolithische Aufbau verhindert den Einfluss der Absorptionslinien von Wasser auf die Form des gestreckten Pulses bei etwaiger Propagation durch Luft. Auf diese Weise lassen sich die nachteiligen Effekte auf die erreichbare Spitzenleistung während der nichtlinearen Verstärkung deutlich reduzieren. Die resultierende Pulsspitzenleistung liegt bei circa 250 MW. Eine weitere Skalierung der Spitzenleistung wird durch das Einsetzen eines nichtlinearen Energietransfers weg vom Hauptpuls verhindert. Die Skalierung der mittleren Leistung ist mit diesem Aufbau auf 31 W begrenzt, da die thermische Last, die durch das Pumpen bei 793 nm entsteht, nur in unzureichendem Maße von der Faser abgeführt wird. In einem darauffolgenden Schritt wird deshalb eine verbesserte Kühlanbindung der Hauptverstärkerfaser mittels eines thermisch leitfähigen Silikons verwendet, wodurch sich eine durch verfügbare Pumpleistung limitierte mittlere Ausgangsleistungen von 120 W erreichen lässt. Die gemessene Verstärkertemperatur ist unterhalb von 70 °C, was darauf hinweist, dass eine weitere Skalierung der mittleren Leistung mit diesem Kühlungskonzept möglich ist, insbesondere wenn Silikone mit einer noch größeren thermischen Leitfähigkeit eingesetzt werden.

CHAPTER 1

Introduction

Passively mode-locked lasers provide one of the rare possibilities to experience exciting physics from a small footprint experimental setup and simultaneously represent a versatile tool. Their development and parameter scaling is still propelled by demanding applications in the scientific [MBP13; Col+18], medical [Hoy+14], and industrial [LDM97; GM08] sectors. While visibly departing the laboratory environment, the laser systems are expected to operate under more challenging surroundings. All-fiber versions of the mode-locked oscillator and subsequent amplifier stages allow us to tackle the growing demands due to their inherent reliability, reproducibility, and robustness against environmental perturbations. Assisted by technological advances such as large mode-area fibers and chirped pulse amplification (CPA) [SM85], the compact systems' output beams can be scaled up to power-plant-level peak powers that can be focused close to the diffraction-limit.

Generation of the pulses via passive mode-locking can be realised using different kinds of saturable absorbers. However, the fiber lasers' stability assets can only be harnessed using polarisation-maintaining (PM) fibers. For this reason, one of the most popular mode-locking techniques in laboratory fiber oscillators, i.e. nonlinear polarisation rotation (NPR), is ruled out. Common alternatives compatible with all-PM-fiber solutions comprise solid-state saturable absorbers based on absorptive

materials [Kel+96; Set+04], which are often prone to manufacturing fluctuations and degradation due to the operation near their damage threshold [VRR14]. Moreover, the technology is not straightforwardly transferable to different wavelength regimes. Alternatively, mode-locking can be achieved using saturable absorbers based on fiber loops [DW88; Fer+90]. Herein, pulse generation is achieved by an interferometric superposition of the electromagnetic fields, that favors larger peak powers in the cavity. In the past, however, this approach was hampered by self-starting issues [Hän+18; Dua+20]. In 2001, Cairns *et al.* proposed using a fiber loop coupled to the cavity by a 3x3-coupler instead of the commonly used 2x2-coupler [Cai+01]. Fallen into oblivion, the approach has been picked up again in 2019 by Kim *et al.*, who pointed out the advantage of an improved self-starting behaviour and demonstrated the reliable operation in an Er-fiber soliton oscillator [Kim+19]. These findings gave rise to a more in-depth investigation of these mode-lockers which enabled a transfer of the scheme to different wavelength and pulse formation regimes in the course of this work. A main focus in this development is the applicability of the oscillators as seed sources for nonlinear, all-fiber CPA systems which allow for the generation of large average powers and pulse energies compressible to the sub-ps pulse duration regime.

For decades, Ti:sapphire based CPA systems have been the go-to technology for applications requiring large peak powers, i.e. large pulse energies at ultrashort pulse durations. This trend is progressively shifting because of the limited thermal properties of the sapphire crystal which prohibits significantly further scaling of the pulse energy while maintaining high repetition rates. Thin disk, slab, and fiber laser geometries all proved favorable for handling the heat loads of high power operation enabling average output powers beyond 1 kW [Neg+15; Rus+10; WYL13a]. Herein, Yb-doped active media, emitting in the 1 µm-regime, are commonly preferred due to their simple energy level structure allowing for efficient in-band pumping and thus low heat loads. Interestingly though, the largest average power of a single-channel ultrashort pulse fiber laser was demonstrated using Tm-doped fibers emitting around 2 µm wavelength [Gai+18]. In these experiments, it was also found that Tm-doped fiber lasers are significantly more robust against the onset of transverse mode instabilities (TMI), which is currently the most severe limitation in terms of average power scaling of fiber lasers [Jau+12; JSL20]. Thus, despite being apparently

more challenging to master, due to minor efficiencies and thus larger heat loads, the maturity of the components' technology, and atmospheric adversities, Tm-fiber lasers hold promise of a significant average power *and* pulse energy scaling compared to their 1 µm counterpart. The obtainable pulse energies in a fiber CPA system are ultimately limited by the accumulation of a nonlinear phase during the amplification of the tightly confined pulses in the fiber, which subsequently diminishes the pulse compressibility. The impact of nonlinear effects, however, scales inversely with wavelength, giving Tm-doped fiber lasers the opportunity to outperform ultrashort Yb-systems once both technologies reach equal maturity. Apart from these considerations, many applications profit or become only possible due to different optical properties at 2 µm. For example, polymers or semiconductors, such as silicon, exhibit largely different absorption behaviour towards 2 µm wavelengths which enables novel applications in terms of direct laser material processing, e.g. by in-bulk material processing driven by nonlinear absorption [Min+12; Nej+05].

In this Thesis, the generation as well as the chirped pulse amplification of highly energetic ultrashort pulses in the 2 µm regime are treated with special regard towards an all-fiber integrability of the system. In Chapter 2 and 3 the theoretical basics of fiber technology, pulse generation, and (nonlinear) amplification are outlined which allows for the description and analysis of the subsequent experimental findings. The experimental results of Tm- and Yb-based fiber oscillators mode-locked by nonlinear amplifying loop mirrors (NALMs) coupled to the resonator via a 3x3-fiber coupler are presented in Chapter 4. Subsequently, the results are compared with theoretical expectations based on a model of reduced complexity as well as complete-cavity split-step Fourier method simulations, and discussed in terms of their applicability as a seed source for nonlinear CPA. In Chapter 5 the efforts of pulse energy and average power scaling in a monolithic, i.e. all-fiber, nonlinear Tm-CPA system are outlined. Chapter 6 provides a conclusion of the work.

CHAPTER 2

Concepts of Ultrashort Pulse Propagation in Optical Fibers

In this Chapter, general concepts concerning optical fibers as waveguides, Tm-doped fibers for light amplification as well as ultrashort pulse propagation therein are summarised, which is the basis for understanding the subsequent chapters. The waveguide and pulse propagation sections are mainly based on the books by Snyder/Love [SL83] and Agrawal [Agr07], respectively, where more extensive treatments of the subjects can be found.

2.1 The Optical Fiber as Dielectric Waveguide

Optical fibers are dielectric waveguides which usually possess a cylindrical shape. A common type is the step-index glass fiber, which has a doped core of high refractive index n_{core} surrounded by a typically undoped cladding of lower refractive index n_{clad}. In a simple picture, the light is guided inside the core of the fiber due to total internal reflection at the core-cladding interface. A more in depth comprehension of the light guidance requires the notion of fiber modes obtained from solving the

corresponding wave equation for the electric field $\tilde{\mathbf{E}}$ of angular frequency ω [SL83]

$$\left[\partial_x^2 + \partial_y^2 + \omega^2 n^2(x,y,\omega)/c_0^2 - \beta_{\mathrm{m}}^2(\omega)\right] \tilde{\mathbf{E}}_{\mathrm{m}}(\mathbf{r},\omega) = 0 \quad \text{with} \quad \beta_{\mathrm{m}}(\omega) := \omega n_{\mathrm{m,eff}}(\omega)/c_0. \tag{2.1.1}$$

Here, c_0 is the speed of light in vacuum, n is the refractive index, and β denotes the propagation constant. In order to arrive at the above equation from the source-free Maxwell equations, the weakly guiding approximation ($n_{\mathrm{core}} \approx n_{\mathrm{clad}}$) has been employed, which implies that the different electric field components of an individual fiber mode "m" do not mix, resulting in linearly polarised (LP), transverse modes. The fiber modes comprise characteristic transverse field distributions $F_{\mathrm{m}}(x,y)$ with corresponding propagation constants $\beta_{\mathrm{m}}(\omega)$, determined by an effective refractive index $n_{\mathrm{m,eff}}(\omega)$ that depends on the transverse progression of the refractive index $n(x,y,\omega)$. Accordingly, the wave equation (2.1.1) can be solved by a linearly polarised ansatz

$$\tilde{\mathbf{E}}_{\mathrm{m}}(\mathbf{r},\omega) = \frac{1}{2}\hat{\mathbf{x}}\left[F_{\mathrm{m}}(x,y)\tilde{A}(z,\omega)e^{i\beta_{\mathrm{m}}(\omega)z} + c.c.\right]. \tag{2.1.2}$$

The transverse field distributions $F_{\mathrm{m}}(x,y)$ of the fiber modes can be normalised to form an orthonormal basis, i.e. any guided transverse field distribution can be expanded in a series of $F_{\mathrm{m}}(x,y)$. However, for a given angular frequency ω only a finite number of different β_{m} exist for which the field is bound, i.e. it vanishes for $\sqrt{x^2+y^2} \to \infty$. Light, which is launched into the fiber, will excite the available fiber modes weighted by the overlap of the free-space and the bound fiber modes. The number of supported bound/guided modes is determined by the numerical aperture of the fiber [SL83]

$$\mathrm{NA} = \sqrt{n_{\mathrm{core}}^2 - n_{\mathrm{clad}}^2} = n_0 \sin\alpha, \tag{2.1.3}$$

where α is the acceptance angle of the light launched from a medium with refractive index n_0, the core radius r_{core}, and the vacuum wavelength $\lambda_0 = 2\pi c_0/\omega$ of the light. In this context the V number

$$V := \frac{2\pi r_{\mathrm{core}}}{\lambda_0}\mathrm{NA}. \tag{2.1.4}$$

is a helpful parameter. For $V < 2.405$ step-index fibers only support a single guided mode for **x**- and **y**-polarisation each [SL83]. Larger values allow for the existence of additional transverse modes. In the context of fiber lasers, single-mode operation is an important asset and usually a desired feature, as the fundamental mode enables an exceptional output beam quality corresponding to values of the beam propagation factors M^2 below 1.1, i.e. close to an ideal Gaussian beam.

Optical Fibers For High Power Operation In a fiber laser, the core of the active fiber is commonly doped by rare-earth ions as for example Pr^{3+}, Yb^{3+}, Nd^{3+}, Er^{3+}, Tm^{3+}, or Hm^{3+}. When excited at a pump wavelength λ_{Pump}, these ions can be used for stimulated light amplification at a signal wavelength λ_{Signal} (see Section 2.2). However, as both wavelengths need to be launched and guided in the fiber, the efficiency of the amplification process can be drastically limited by the brightness of the pump source. This problem is circumvented in so-called double-cladding fibers, where the pump light is guided in a second, typically concentric, guiding structure with a larger core radius and NA, i.e. a large acceptance angle α of the launched light. As a result, laser diodes with high power and low brightness coupled into the highly multi-mode pump core can be used to efficiently amplify a single-mode signal.

The resulting large signal powers along with large interaction lengths and a confinement to small mode-areas in the fiber core promote nonlinear optical effects, e.g. based on the Kerr-effect. While these nonlinear effects are an integral part of the generation of ultrashort pulses, they also represent a severe limitation in terms of (peak) power scalability of fiber based amplifiers. As the nonlinear effects scale with the intensity, an increased effective mode-area of the signal, which can be defined by [Agr07]

$$\mathrm{MA}_{\text{eff}} := \frac{\left[\iint |\mathbf{E}_{\text{m}}(\mathbf{r},t)|^2 \mathrm{d}x\mathrm{d}y\right]^2}{\iint |\mathbf{E}_{\text{m}}(\mathbf{r},t)|^4 \mathrm{d}x\mathrm{d}y}, \tag{2.1.5}$$

allows for an effective mitigation thereof. According to Equation (2.1.4), the core radius and thereby the mode-area of step-index fibers can be increased, as long as the NA is decreased by the same factor, without sacrificing the single mode property. However, this scaling approach of the mode-area is practically limited by an increasing sensitivity to bending [SC07] and refractive index variations in the

manufacturing process of very low NA fibers.

Alternatively, microstructuring techniques can be used to manipulate the waveguide properties and allow active, large mode-area fibers to effectively operate in single-mode conditions. In this regard, there are two main approaches, which differ in the mechanisms by which light is confined in the fiber. Photonic bandgap fibers [Pul+15] permit light trapping and guidance even in low refractive index cores. The trapping is enabled by a periodic index variation on the wavelength scale in the cladding which generates a region of forbidden light propagation [Rus03]. The second approach, which is also the principle of a Tm-doped fiber used in this work, is based on index-guiding similar to conventional step index fibers. Here, typically air holes are used to reduce the *effective* refractive index around the high index core region. Thereby a low effective NA can be obtained in a precise and controllable manner. The fibers are usually not strictly single-mode, i.e. $V > 2.405$. However, additional techniques for higher-order mode discrimination, which include a doped core geometry, allow for preferential gain of the fundamental mode [SO99; Mar09], preferential loss for higher-order modes by bending [KKG00], as well as selective excitation of the fundamental mode, which still allows for an effective single-mode operation.

2.2 Properties of Thulium-Doped Fibers as Active Medium

Thulium-doped fused silica possess a broad emission spectrum around 1900 nm that allows for the generation and amplification of pulses shorter than 100 fs [Gai+17]. Incorporating them as active media in fiber laser setups enables large single-pass amplifications due to large propagation lengths in the active medium with a small mode field area. However, compared to other rare-earth doped silica used for high-power laser operation in the infra-red, such as ytterbium, thulium stands out by the complexity of its energy level structure. As a consequence, unfavourable energy transfer processes can hinder efficient laser operation. On the other hand, cross-relaxation mechanisms even open up pumping schemes deemed unpromising at first sight. In the following section these mechanisms shall be illuminated and incorporated in a rate-equation based model capable of describing the light amplification in the

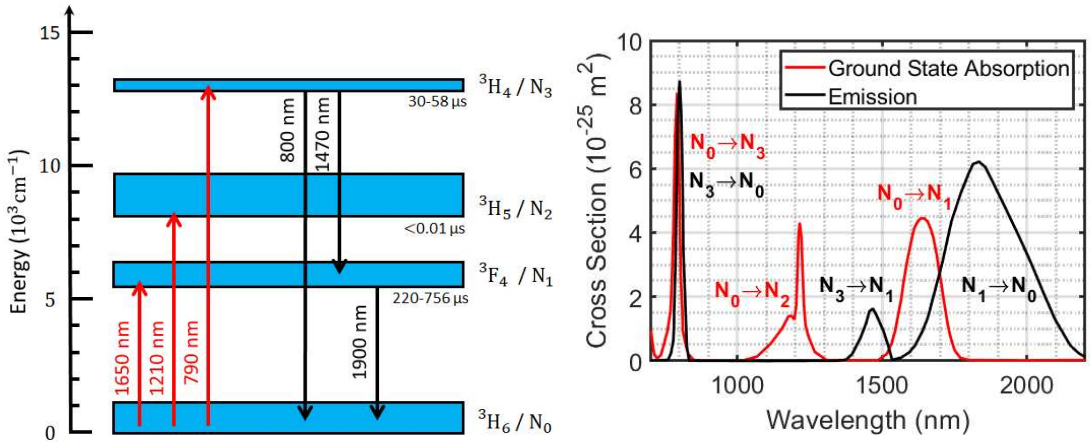

Figure 2.1: Spectroscopic details of Tm-doped fused silica. (a) Energy level scheme of Tm-doped fused silica together with possible pump transitions (red arrows) and emission from excited states (black arrows). Lifetimes according to [Caj+18]; larger lifetimes of N_1 are obtained for stronger aluminium co-doping. (b) Absorption and emission cross sections of Tm-doped fused silica for the four lowest levels, reproduced from [Pet+04]. Not depicted: excited state absorption, for example near 1100 nm or 1400 nm from N_1 and N_3 to higher lying levels.

2 µm wavelength regime by Tm-doped fibers.

2.2.1 Energy Level Structure and Transfer Processes

Figure 2.1 (a) shows the four lowest energy levels of thulium-doped fused silica, approximate values for ground-state absorption and excited-state emission wavelengths, along with lifetimes reported in the literature. As usual in solid state laser media, each of the depicted levels consists of a manifold of energy levels, which can be considered degenerate for the case of an isolated atom. The degeneracy is lifted by Stark splitting due to the influence of the host material's electric field acting on the Tm-ions. Moreover, lattice vibrations interacting with the electrons of the Tm-ions in the medium cause a broadening of the individual spectral lines compared to their natural width in an isolated atom and also enable vibration induced non-radiative transitions between the sub-levels [Sil62; Kri65]. In glasses, the local vibrations and electric fields experienced by the individual Tm-ions differ largely due to the amorphous host material. Macroscopically, the thereby induced broadening and overlapping of the individual energy levels enables a description in terms of effec-

tive energy level manifolds (or energy bands), whose interaction with light can be described by continuous, effective transition cross sections. The effective absorption and emission cross sections σ_a and σ_e for the case of Tm-doped silica measured by Peterka et al. are depicted in Fig. 2.1 (b) [Pet+04].

The particular interest in Tm-doped fibers in the context of ultrashort fiber lasers stems from the broad emission spectrum ($N_1 \rightarrow N_0$) in the 2 µm regime, whose centroid is spectrally shifted compared to the corresponding absorption spectrum ($N_0 \rightarrow N_1$). This shift is a direct consequence of the fast, phonon-assisted relaxation towards the lower band edges of both involved bands. As a result, absorption is preferentially observed at shorter wavelengths. In order to gain access of the broad emission spectrum, several pump transitions are conceivable. For example, the Tm-fiber can be pumped in-band ($N_0 \rightarrow N_1$) in the wavelength range 1500-1800 nm at the advantage of a small quantum defect ($\mathrm{QD} = 1 - \lambda_{\mathrm{Pump}}/\lambda_{\mathrm{Signal}}$) and thus potentially a larger slope efficiency. Moreover, pumping into the N_2-state is possible in the wavelength range 1100-1300 nm at the cost of a larger QD. Yet, the most common pump transition used for high power Tm-fiber lasers is $N_0 \rightarrow N_3$ near 790 nm which has a QD of $\approx 60\,\%$ for signal wavelengths around 2 µm. The main reason for this circumstance is the availability of high power, low brightness laser diodes in this wavelength regime. Additionally, a Tm-ion excited into the N_3-state can partially transfer its excitation energy to a neighbouring Tm-ion in the ground state, whereupon both ions are in the N_1-state, i.e. in the upper laser level [Hay+00; Jac04]. This cross-relaxation process can drastically reduce the QD and therefore the heat load in appropriately doped Tm-amplifiers.

2.2.2 Rate Equation Based Calculation of Laser Amplification

In order to model the amplification process in Tm-doped fibers based on coupled rate equations, such energy transfer processes (ETPs) between neighbouring Tm-ions need to be taken into account. The mentioned pumping schemes additionally allow for a plethora of inter-ionic processes which also involve higher lying energy levels than the ones shown in Fig. 2.1 (a) [JK99]. Generally, such processes are strongly dependent on the distance between the ions and therefore on the Tm-doping concentration. As long as the Tm-ions are distributed homogeneously in the glass matrix and for moderate doping concentrations, cascaded excitations to higher levels than N_3

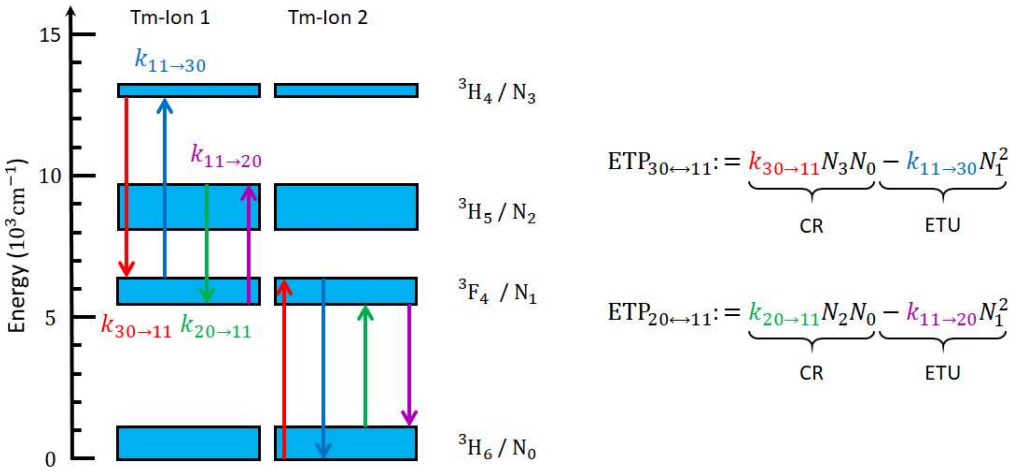

Figure 2.2: Depiction of the energy transfer, i.e. cross-relaxation (CR) and energy transfer upconversion (ETU), between neighbouring Tm-ions which are relevant for the amplification process.

have been found to have a low impact on the laser efficiency [Jac04]. However, the homogeneous distribution of the Tm-ions must be ensured as clustering of Tm-ion evokes upconversion processes, which are detrimental to an efficient laser operation due to lifetime quenching of the upper laser level N_1. Typically, this can be assured by co-doping $>10\,\%$ percent of aluminium to the fiber core [JM03]. If this requirement is met, the lowest four energy levels are sufficient to describe and model the laser operation of a Tm-fiber laser for all three of the above pumping schemes[1]. For these levels the relevant cross-relaxation (CR) processes and their inverse, i.e. energy transfer upconversion (ETU), are schematically depicted in Fig. 2.2. Including them, the coupled rate equations, which are used to describe the population dynamics of the Tm-doped fiber's energy levels along its longitudinal axis z, can be expressed by

[1] In the context of this work, no pumping to level $^3H_5$ is employed. Thus, the pumping scheme is excluded from the model and the further discussion.

[JK99; Eic05]:

$$\begin{aligned}
\frac{\partial N_0(t,z)}{\partial t} =& -[W_{01}(t,z)+W_{03}(t,z)]N_0(t,z) \qquad (2.2.1)\\
&+[W_{10}(t,z)+R_{10}]N_1(t,z)+R_{20}N_2(t,z)+[W_{30}(t,z)+R_{30}]N_3(t,z)\\
&-\mathrm{ETP}_{30\leftrightarrow 11}(t,z)-\mathrm{ETP}_{20\leftrightarrow 11}(t,z),\\
\frac{\partial N_1(t,z)}{\partial t} =& +W_{01}(t,z)N_0(t,z)-[R_{10}+W_{10}(t,z)]N_1(t,z)+R_{21}N_2(t,z) \qquad (2.2.2)\\
&+R_{31}N_3(t,z)+2\mathrm{ETP}_{30\leftrightarrow 11}(t,z)+2\mathrm{ETP}_{20\leftrightarrow 11}(t,z),\\
\frac{\partial N_2(t,z)}{\partial t} =& -[R_{21}+R_{20}]N_2(t,z)+R_{32}N_3(t,z)-\mathrm{ETP}_{20\leftrightarrow 11}(t,z), \qquad (2.2.3)\\
\frac{\partial N_3(t,z)}{\partial t} =& +W_{03}(t,z)N_0(t,z)-[W_{30}(t,z)+R_{32}+R_{31}+R_{30}]N_3(t,z) \qquad (2.2.4)\\
&-\mathrm{ETP}_{30\leftrightarrow 11}(t,z).
\end{aligned}$$

Here, the spontaneous (radiative and non-radiative) decay from level i to j is included by R_{ij} and $\mathrm{ETP}_{ij\leftrightarrow kl}$ denotes the energy transfer processes between the levels i,j and k,l as detailed in Fig. 2.2. Table 2.1 summarises the corresponding rates.

	R_{10}	R_{20}	R_{21}	R_{30}	R_{31}	R_{32}
(s^{-1})	3×10^{3}	181	1.4×10^{8}	717	59	8×10^{4}
	$k_{30\to11}$		$k_{11\to30}$	$k_{20\to11}$		$k_{11\to20}$
$(\mathrm{m}^3\mathrm{s}^{-1})$	1.3×10^{-21}		1.1×10^{-22}	3×10^{-24}		1.5×10^{-24}

Table 2.1: Decay rates and energy transfer rates for the rate equation model [Pet+92; PI95; JK99].

The pump or stimulated emission rates from N_i to N_j are described by W_{ij} and can be calculated by [Eic05]:

$$W_{ij}(t,z)=\sigma_{ij}(\lambda)P(\lambda,t,z)\frac{D(\lambda)\lambda}{F_{\mathrm{doped}}hc}, \qquad (2.2.5)$$

$$D(\lambda)=\begin{cases}1-\exp\left[-2F_{\mathrm{doped}}/F_{\mathrm{MF}}(\lambda)\right] & \text{for } \lambda=\lambda_{\mathrm{Signal}} \text{ or } \lambda=\lambda_{\mathrm{Pump,SC}}\\ F_{\mathrm{doped}}/F_{\mathrm{Pump}} & \text{for } \lambda=\lambda_{\mathrm{Pump,DC}}\end{cases} \qquad (2.2.6)$$

with $\sigma_{ij}(\lambda)$ being the transition cross-section, i.e. absorption ($i < j$) or emission ($i > j$) cross-section, at wavelength λ, which can be either the signal or the pump wavelength. For the case of a double-clad (DC) amplifier, the signal is propagating in the core of the fiber (cross sectional area F_{Doped}) with a Gaussian mode field area F_{MF} and the multimode pump in the cladding with cross sectional area F_{Pump}. Thus different spatial overlap factors $D(\lambda)$ with the Tm-doped core must be taken into account as displayed in Equation (2.2.6). The power spectral density (PSD) at the corresponding wavelength is denoted by $P(\lambda, t, z)$ and accounts for the sum of pump, signal, and ASE (amplified spontaneous emission) power propagating in both directions.

Evidently, the absorption and emission of pump, signal, and ASE light changes the corresponding PSDs along the fiber. The resulting power evolutions in positive (+) and negative (-) z-direction can be calculated according to

$$\frac{\partial P^{\pm}_{\mathrm{Pump}}(t,z)}{\partial z} = \pm\left[-(\sigma_{01}+\sigma_{03})N_0 + \sigma_{10}N_1 + \sigma_{30}N_3\right]D(\lambda_{\mathrm{Pump}})P^{\pm}_{\mathrm{Pump}}, \tag{2.2.7}$$

$$\frac{\partial P^{\pm}_{\mathrm{Signal}}(t,z)}{\partial z} = \pm\left[-\sigma_{01}N_0 + \sigma_{10}N_1\right]D(\lambda_{\mathrm{Signal}})P^{\pm}_{\mathrm{Signal}}, \tag{2.2.8}$$

$$\begin{aligned}\frac{\partial P^{\pm}_{\mathrm{ASE}}(\mathrm{d}\lambda_m,t,z)}{\partial z} &= \pm\left[-(\sigma_{01}+\sigma_{03})N_0 + \sigma_{10}N_1 + \sigma_{30}N_3\right]D(\lambda_m)P^{\pm}_{\mathrm{ASE}} \\ &\quad \pm\left[\sigma_{10}N_1 + \sigma_{30}N_3\right]D(\lambda_m)M_m\frac{2hc^2}{\lambda_m^3}\mathrm{d}\lambda_m,\end{aligned} \tag{2.2.9}$$

in which the generation of spontaneous emission in a wavelength interval $\lambda_m \pm \mathrm{d}\lambda_m/2$ is modeled by the last line [Eic05]. The factor M_m accounts for the number of guided modes within the fiber core at the respective wavelength. The set of coupled Equations (2.2.1) to (2.2.9) are used to numerically calculate the amplification of an input signal $P^{+}_{\mathrm{Signal}}(0,0)$ in a Matlab script. Thereby, the fiber is typically discretised in steps of 1 cm and the time in steps of 10 ns. In principle, the implemented script would also allow for modelling the amplification of a pulsed input, once the time discretisation is reduced accordingly. However, since in the course of this work, only large repetition rates $\geq 200\,\mathrm{kHz}$ (pulse spacing $\leq 5\,\mu\mathrm{s}$) and small pulse energies compared to the energy stored in the fiber appear, dynamic effects of inversion depletion by single pulses or depletion due to the fluorescence between the pulses are expected to have a small impact on the amplification process. Convergence of

the simulation is achieved once the steady state solution $\partial N_i/\partial t \approx 0$ is reached and the signal power at the fiber output is approximately constant over multiple amplification iterations.

2.2.3 Determination of the Heat Load and Temperature Along the Fiber

During laser amplification, a fraction of the pump power is converted to heat. The resulting temperature distributions can have detrimental effects on the amplification process as will be discussed more in-depth in Section (5.3). In general, the heat stems from non-radiative transitions between different manifolds, which is particularly the case for 790 nm pumping, as well as non-radiative relaxations within single manifolds. The model described in the previous passage can be used to determine the heat density $Q(z)$ per volume along the fiber. In simple terms, it corresponds to the absorbed pump power which is *not* converted to signal or ASE light[2]:

$$Q(z) = \frac{\Delta P_{\text{Pump}}(z) - \Delta P_{\text{Signal}}(z) - \Delta P_{\text{ASE}}(z)}{F_{\text{doped}} \Delta z}. \tag{2.2.10}$$

Once the steady-state heat density is known, the temperature distribution $T(\mathbf{r})$ along the fiber can be calculated according to the heat equation

$$\frac{1}{r}\frac{\partial}{\partial r}\left[rk(\mathbf{r})\frac{\partial T(\mathbf{r})}{\partial r}\right] + \frac{1}{r^2}\frac{\partial}{\partial \phi}\left[k(\mathbf{r})\frac{\partial T(\mathbf{r})}{\partial \phi}\right] + \frac{\partial}{\partial z}\left[k(\mathbf{r})\frac{\partial T(\mathbf{r})}{\partial z}\right] = \begin{cases} -Q(z) & \text{for } 0 \leq r \leq r_{\text{doped}} \\ 0 & \text{for } r_{\text{doped}} < r. \end{cases} \tag{2.2.11}$$

Herein, it is assumed that the heat is generated uniformly in the Tm-doped volume of the core and therein only exhibits a dependence along the z axis. For the case of cylindrically symmetric cooling, e.g. when the fiber is directly water cooled, the above equation can be simplified considerably towards a one-dimensional problem neglecting the ϕ- and z-dependence, which allows for an analytical treatment [BH01]. In general, however, the cooling process is not cylindrically symmetric and materials

[2] In this approach the power fraction of spontaneous radiative transitions, i.e. fluorescence, is neglected. However, in the dominant spontaneous transition rates R_{10}, R_{21}, and R_{32} in Table 2.1, the non-radiative fractions are orders of magnitude larger than the radiative fractions, which renders the generated fluorescence power negligible.

of different thermal conductivities k are used in the cooling process. Thus the determination of the temperature distribution along a fiber laser requires a numerical approximation of Equation (2.2.11) with adequately defined domains and boundary conditions.

2.3 Pulse Propagation in Optical Fibers

The wave equation that describes the propagation of light in a fiber can be derived directly from the source-free Maxwell equations and the constitutive relations $\mathbf{D} = \epsilon_0\mathbf{E}+\mathbf{P}$ and $\mathbf{B} = \mu_0(\mathbf{H}+\mathbf{M})$, where $\mathbf{M} \approx \mathbf{0}$, due to the negligible magnetic response of silica at optical frequencies [Agr07]:

$$\left(\nabla^2 - \frac{1}{c_0^2}\frac{\partial^2}{\partial t^2}\right)\mathbf{E}(\mathbf{r},t) = \mu_0\frac{\partial^2\mathbf{P}(\mathbf{r},t)}{\partial t^2}. \tag{2.3.1}$$

The plethora of physical effects which are observed in fiber optics are thus dictated by the way the induced polarisation $\mathbf{P}$ in the medium depends on the electric field $\mathbf{E}$ of the light. For low light intensities, the bound electrons follow a harmonic motion of the driving electric field, resulting in a linear relation between $\mathbf{E}$ and $\mathbf{P}$. However, due to the confinement of light in fibers large intensities are easily reached, such that the response of the electrons can no longer be considered purely harmonic. Consequently, the polarisation $\mathbf{P}$ induced by the light is no longer proportional to the electric field $\mathbf{E}$, but higher-order terms of the expansion need to be taken into account:

$$\mathbf{P}(\mathbf{r},t) = \underbrace{\epsilon_0\chi^{(1)}\cdot\mathbf{E}}_{\text{linear term }\mathbf{P}_\text{L}} + \underbrace{\epsilon_0[\chi^{(2)}:\mathbf{EE}+\chi^{(3)}\vdots\mathbf{EEE}+\ldots]}_{\text{nonlinear term }\mathbf{P}_\text{NL}}, \tag{2.3.2}$$

where $\chi^{(n)}$ is the media's electric susceptibility of order n. The linear term with susceptibility $\chi^{(1)}$ is the leading-order term. It is the source of all linear optical effects experienced by the optical pulse. For example, the fact that $\chi^{(1)}$ depends on the angular frequency ω leads to the effect of chromatic dispersion. In amorphous media (e.g. silica), the $\chi^{(2)}$-term vanishes due to the macroscopic centrosymmetry, prohibiting second-harmonic and sum-frequency generation in these media. Thus, the next-to-leading order term is the $\chi^{(3)}$-term, which among others causes an intensity

dependent refractive index, i.e. the Kerr effect.

For the propagation of an optical pulse with central frequency ω_0 and bandwidth $\Delta\omega \ll \omega_0$, the problem can be simplified by applying the slowly varying envelope approximation $\left|\frac{\partial^2 \mathbf{E}}{\partial z^2}\right| \ll \frac{\omega_0}{c_0}\left|\frac{\partial \mathbf{E}}{\partial z}\right|$ [Agr07]. Moreover, the coupling between different electric field components due to $\mathbf{P}_{\mathrm{NL}}$ is assumed to be negligible and therefore the linearly polarised ansatz can be applied again

$$\mathbf{E}(\mathbf{r},t) = \frac{1}{2}\hat{\mathbf{x}}\left[F(x,y)A(z,t)e^{-i[\omega_0 t - \beta(\omega_0)z]} + c.c.\right]. \tag{2.3.3}$$

The physical interpretation is that the electric field of the optical pulse exhibits a fast oscillation with central frequency ω_0 underneath a pulse envelope with a complex valued amplitude $A(z,t)$ and has a transverse field distribution $F(x,y)$ determined by the fiber mode. Herein, the temporal phase $\phi(z,t)$ of the amplitude $A = |A|e^{i\phi}$ is related to a deviation of the instantaneous frequency from the central frequency ω_0, i.e. $\omega(t) = \omega_0 + \delta\omega(t) = \omega_0 - \partial\phi/\partial t$. Accordingly, an up- or down-chirp of the pulse, which corresponds to an increasing or decreasing instantaneous frequency along the pulse, is characterised by $-\partial^2\phi/\partial t^2 > 0$ or $-\partial^2\phi/\partial t^2 < 0$, respectively.

Following this approach, a nonlinear pulse propagation equation, the extended nonlinear Schrödinger equation (NLSE), can be derived, which includes the most relevant effects of the pulse evolution [Agr07]:

$$\frac{\partial A(z,t)}{\partial z} = \underbrace{-\frac{\alpha}{2}A}_{\text{Loss/Gain}} \underbrace{-i\frac{\beta_2}{2}\frac{\partial^2 A}{\partial t^2}}_{\text{Dispersion}} \underbrace{+i\gamma|A|^2 A}_{\substack{\text{Self-Phase}\\ \text{Modulation}}}. \tag{2.3.4}$$

In this equation, a frame of reference moving with the pulse is employed using the substitution $t \to t - z/v_g$, where the group velocity $v_g = 1/\beta_1$ is the velocity of the pulse envelope.

Dispersive effects, e.g. due to a wavelength dependence of the fiber's refractive index, are accounted for by the group velocity dispersion (GVD) β_2. Where β_2 is the first coefficient in the Taylor expansion of the propagation constant $\beta(\omega)$

$$\beta(\omega) = n_{\mathrm{eff}}(\omega)\frac{\omega}{c} = \sum_{j\geq 0}\frac{(\omega-\omega_0)^j}{j!}\beta_j \quad \text{with} \quad \beta_j := \left.\frac{\mathrm{d}^j\beta}{\mathrm{d}\omega^j}\right|_{\omega=\omega_0} \tag{2.3.5}$$

which influences the pulse envelope via a relative delay between its frequency com-

ponents, i.e. a chirp induced pulse stretching. Similarly, the spectral phase $\phi(z,\omega)$ of the envelope's spectral amplitude $\tilde{A}(z,\omega) = |\tilde{A}|e^{i\phi}$ can be expanded in a Taylor series. The coefficients ϕ_2 and ϕ_3, which are referred to as group delay dispersion (GDD) and third order dispersion (TOD), are commonly used when dealing with separated changes of the phase, e.g. due to a pulse stretcher or compressor.

The treatment of the intensity dependent self-phase modulation (SPM) in Equation (2.3.4) includes the nonlinear coefficient $\gamma = n_2\omega_0/(c\mathrm{MA}_{\mathrm{eff}})$, where n_2 is the nonlinear refractive index coefficient caused by $\chi^{(3)}$

$$n(I) = n_0 + \frac{3\mathrm{Re}\left[\chi^{(3)}\right]}{4n_0^2\epsilon_0 c_0} I = n_0 + n_2 I \tag{2.3.6}$$

and $\mathrm{MA}_{\mathrm{eff}}$ is the effective mode-area of the fiber mode. The nonlinear phase $\phi_{\mathrm{NL}}(z,t)$ caused by SPM can be quantified, when solving Equation (2.3.4) while only regarding the SPM term:

$$\frac{\partial A(z,t)}{\partial z} = i\gamma|A(z,t)|^2 A(z,t) \tag{2.3.7}$$

$$A(z,t) = A(0,t)\exp\left[i\phi_{\mathrm{NL}}(z,t)\right] \quad \text{with} \quad \phi_{\mathrm{NL}}(z,t) = \int_0^z \gamma|A(z',t)|^2 \mathrm{d}z' \tag{2.3.8}$$

The peak nonlinear phase shift of a pulse is referred to as B-integral and can be used to estimate the impact of nonlinear effects during propagation/amplification along a length z:

$$B = \frac{2\pi}{\lambda}\int_0^z n_2 I(z')\mathrm{d}z' \approx \max\left[\int_0^z \gamma|A(z',t)|^2 \mathrm{d}z'\right]. \tag{2.3.9}$$

As the phase modulation induced by SPM explicitly depends on the pulse shape $|A(z,t)|^2$, its practical effects can vary largely. For example, as the instantaneous frequency of the pulse depends on the temporal change of the phase, large temporal phase changes caused by SPM can correspond to instantaneous frequencies which lie outside of the initial pulse's spectral bandwidth. In other words, SPM evoked by a partial wave at frequency ω allows for the change of the complex spectral amplitudes $\tilde{A}$ at different frequencies $\omega \pm \delta\omega$, which permits a spectral broadening that is unattainable by a sole dispersive phase change. However, the spectral broadening only results for un- or up-chirped pulses, whereas down-chirped pulses experience a

spectral narrowing [WBR00]. During propagation in a fiber, the pulse chirp changes continuously due to the combined effect of GVD and SPM. Depending on the initial pulse shape and phase, the resulting temporal and spectral evolution is generally complicated but can be obtained routinely by a numerical evaluation of Equation (2.3.4) as described in Section 3.4.

The extended NLSE can be amended to also include higher-order dispersive effects, e.g. third order dispersion via β_3, as well as higher-order nonlinear effects, e.g. self-steepening, which is caused by an intensity dependence of the group velocity, or stimulated Raman scattering (SRS), which results from a retarded medium response [Agr07]:

$$\begin{aligned}\frac{\partial A(z,t)}{\partial z} =& -\frac{\alpha}{2}A(z,t) + \sum_{j>1}\frac{i^{j+1}}{j!}\beta_j\frac{\partial^j}{\partial t^j}A(z,t) + \dots \\ &\dots + i\gamma\left(1+\frac{i}{\omega_0}\frac{\partial}{\partial t}\right)\left(A(z,t)\int_0^\infty R(t')|A(z,t-t')|^2\mathrm{d}t'\right).\end{aligned} \tag{2.3.10}$$

Here $R(t) = (1-f_\mathrm{R})\delta(t) + f_\mathrm{R}h_\mathrm{R}(t)$ describes the medium's instantaneous and retarded response modeled by the Raman response function h_R and weighted by f_R [3]. Raman scattering describes the inelastic scattering process in which energy is transferred between light and lattice vibrations, mediated by the delayed response of the medium's nuclei. In fused silica, this process preferentially leads to the generation of lattice vibrations, which decreases the photon energy and thus causes a red shift of the pulse spectrum. For large spectral bandwidths, this can allow for intra-pulse Raman scattering, i.e. a continuous energy transfer from the blue to the red end of the spectrum, which effectively shifts the spectrum's central frequency during propagation [MM86; Gor86]. However, SRS can also have a detrimental effect in the context of fiber lasers, as it allows signal power to be transferred out of the desired wavelength range. Particularly for the case of several amplifier stages, where (amplified) spontaneous emission generated in a previous amplifier stage can seed SRS in subsequent stages, which ultimately limits the extractable pulse energy.

[3] For fused silica, they can be approximated by $f_\mathrm{R} = 0.18$ and $h_\mathrm{R}(t) = \frac{\tau_1^2+\tau_2^2}{\tau_1\tau_2^2}\exp(-t/\tau_2)\sin(t/\tau_1)$ [Agr07], where $\tau_1 = 12.2\,\mathrm{fs}$ and $\tau_2 = 32\,\mathrm{fs}$.

CHAPTER 3

Concepts of Fiber-Based Generation and Amplification of Ultrashort Optical Pulses

The first part of this Chapter provides a review over passively mode-locked fiber lasers, with regard towards the occurring fundamental principles and different operating regimes. Herein, the concept of longitudinal resonator modes and their phase-locking for the generation of ultrashort pulses is recapitulated. Furthermore, saturable absorbers, the basic prerequisite for passively mode-locked lasers are introduced. Special consideration is given towards nonlinear amplifying loop mirrors (NALMs) based on 3x3-couplers, which are used for the construction of mode-locked fiber lasers in the subsequent Chapter. The analysis includes the introduction of a model that allows for an explanation of the various temporal and spectral responses observed from these mode-lockers. Subsequently, different pulse shaping regimes are reviewed, which are mostly determined by the occurring magnitude of group velocity dispersion, self-phase modulation as well as spectral filtering effects in the resonator. Ultimately, the different regimes are assessed with regard to their suitability as seed sources for high-energy pulse amplification.

The second part of this Chapter deals with the fiber based pulse amplification to high pulse energies in the micro to milli Joule regime. Thereby, the concept of chirped pulse amplification is treated in a simplified model, which unravels the

influence of the seed pulses spectral shape on the obtainable peak powers in the presence of SPM during amplification. Furthermore, the split-step Fourier method is used to identify the impact of initial perturbations, e.g. due to spectrally narrow water absorption lines, on the obtainable pulse quality and contrast.

3.1 Locking of Longitudinal Resonator Modes

In general, a laser resonator features a set of infinite longitudinal resonator modes, i.e. electric field distributions that reproduce themselves after consecutive round trips. These modes are characterised by a phase-change of a multiple of 2π per resonator round trip [Sve10]:

$$\omega_n \cdot T_{\mathrm{rt}} = n \cdot 2\pi \quad n \in \mathbb{N}. \tag{3.1.1}$$

Here, the round trip time T_{rt} is the time an electromagnetic field of angular frequency ω_n takes for one resonator cycle. Electromagnetic fields with frequencies different from ω_n eventually decay in the resonator due to destructive interference. In first approximation, the longitudinal modes are equidistant in frequency space. In the presence of a gain medium, the modes compete for the available gain, so only the modes at the maximum net gain of the resonator emerge. If only a single mode of the resonator is above the lasing threshold, the laser is in a continuous wave (CW) state with a temporally constant output power. Whenever different modes show up in parallel, the output power is temporally modulated. The different modes generally have no fixed phase relation to each other. However, if special measures are installed to fix the phase relation between the different longitudinal modes, the resonator can periodically emit short pulses of light. The total electric field in the resonator is obtained by summing up the electric fields of all the occurring modes [Sve10]:

$$E(t) = \sum_{n=-N}^{n=N} E_n e^{-i(\omega_n t - \phi_n)} \tag{3.1.2}$$

with E_n, ϕ_n, and ω_n being the respective electric field amplitude, phase, and frequency of each of the $2N+1$ excited modes. Mode-locking is achieved when multiple longitudinal modes are synchronised in a way that phase differences between consec-

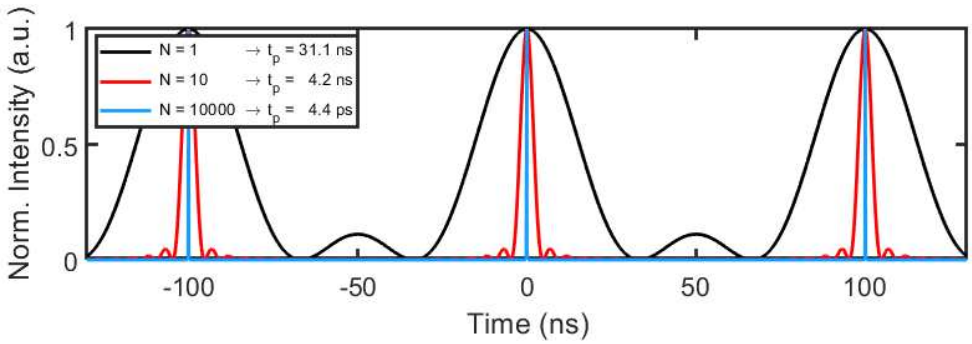

Figure 3.1: Pulse trains and corresponding pulse durations resulting from different numbers of locked longitudinal modes $(2N+1)$ for a repetition rate of $f = \Delta\omega/(2\pi) = 10\,\mathrm{MHz}$ according to Equation (3.1.3).

utive modes are fixed: $\phi_n - \phi_{n-1} = \Phi$. For constant Φ, this implies that the phases can be expressed as $\phi_n = n\Phi + \phi_0$. The frequency of the longitudinal modes is simply given by $\omega_n = \omega_0 + n\Delta\omega$, with ω_0 being the frequency of the mode $n = 0$ in the above summation. If it is additionally assumed that the involved modes have the same amplitude E_0, an analytical result can be obtained [Sve10]:

$$|E(t)|^2 = E_0^2 \frac{\sin^2\left[(2N+1)(\Delta\omega t/2 + \Phi/2)\right]}{\sin^2\left(\Delta\omega t/2 + \Phi/2\right)}. \tag{3.1.3}$$

In Fig. 3.1 the pulse trains for different numbers of locked longitudinal modes is plotted. It can be seen, that an increasing number of modes, i.e. a broader pulse spectrum, leads to a shortening of the pulses in the time domain. For example, in order to generate femtosecond pulses (pulse duration $< 1\,\mathrm{ps}$) in the near-infrared wavelength regime a spectral width of several nanometers is required. If a resonator length of several meters is assumed, the spacing between the resonator modes is in the order of 10^{-4} nanometers, thus several 10.000 modes need to be locked in phase for a femtosecond pulse to propagate in the resonator. The question arises: how is this phase-locking achieved in practice?

3.2 Saturable Absorbers

Mode-locking of lasers can be intuitively easier understood in the time domain. A mode-locked laser device incorporates some sort of intra-cavity amplitude modulation that favours pulsed over CW operation. Without further measures, the gain medium will provide larger gain for a narrow-band laser signal, due to the shape of the gain profile and mode competition, resulting in CW operation [Ipp94]. In order to allow for mode-locked operation, the required amplitude modulation has to induce a larger loss for low intensity light. During the starting process of such mode-locked lasers, long pulses which are randomly generated by mode beating in the cavity, can subsequently be reshaped into short stable pulses, while the low intensity background is suppressed. In practice, this can be done actively by an external radio frequency signal via acousto-optic or electro-optic modulators [Hug68], that apply a fixed loss modulation which is synchronised to the cavity round trip time. An important effect of the fixed loss is that pulse duration reduction decreases for shorter pulses due to counteracting effects of gain-narrowing and dispersion. The resulting minimal pulse durations are typically in the picosecond range. Even shorter pulses can be generated by using saturable absorbers in a passively mode-locked laser. Here, the pulse duration reduction relies on self-amplitude modulation, meaning that the shape and intensity of the pulse itself influences the magnitude of the pulse duration reduction.

Generally, a saturable absorber reacts with a change in absorption to a varied incoming light intensity. More specifically, it inflicts a large loss on weak signals while being more transparent for intense signals. When a long pulse impinges on such an absorber multiple times in the resonator, its wings are successively suppressed relative to the more intense peak part, leading to a pulse shortening.

In practice, saturable absorbers can be realised by real absorptive materials, where the saturation of the absorption stems from the bleaching of possible transitions from its ground state to an excited state. The most prominent and extensively examined representative of this group being semiconductor saturable absorber mirrors (SESAMs) [Kel+96]. On the other hand, there are also different types of so-called artificial saturable absorbers that mimic saturable absorption by transforming SPM induced effects into a self-amplitude modulation. These absorbers will be examined

in the next passage.

3.2.1 The Nonlinear Amplifying Loop Mirror as Artificial Saturable Absorber

The general idea behind artificial saturable absorbers is to use a Kerr-effect induced influence on the signal to favor high intensity operation of the resonator. This idea has several advantages over solid-state saturable absorbers. Firstly, the recovery time of such schemes can be in the order of only a few femtoseconds and thereby much shorter than solid-state saturable absorbers. This enables parameter regimes where both the leading and trailing parts of the pulse need to be substantially shaped in order to enable a stable mode-locked operation. Furthermore, artificial saturable absorbers can be less prone to degradation than solid-state saturable absorbers, which makes them more suitable for long-term operation [VRR14]. On the other hand, it has proven difficult to attain a reliable self-starting behaviour of the mode-locked operation using artificial absorbers only, which is why they are often avoided in turn-key solutions.

One commonly used implementation of artificial saturable absorbers is additive pulse mode-locking (APM) [IHL89]. It is based on the interferometric superposition of two pulses that have originally been generated by splitting one pulse. Prior to superposition, the two pulses receive a phase bias with respect to one another. During the propagation one pulse experiences a larger phase shift due to SPM. As SPM is an intensity dependent process, the pulse peak encounters a stronger phase change, such that constructive interference for only the peak part of the pulse can be achieved, while the less intense wings of the pulse interfere destructively. This way a reduced pulse width inside the resonator can be realised without using an intrinsic saturable absorber.

In the case of fiber lasers, there exists a simple way of implementing the aforementioned scheme which relies on the use of a fiber loop mirror coupled to the resonator by a directional fiber coupler. The coupler splits the pulse into two pulses which counter-propagate in the loop and interfere with each other back at the coupler. The required phase bias of the pulses either stems directly from the relative phase change due to the coupler or can be influenced using a non-reciprocal element (e.g. magneto-optical device). For the two pulses to acquire different amounts of SPM

during the propagation some form of asymmetry needs to be introduced in the loop. This can either be done by varying the coupling ratio to the different ports of the coupler or by introducing gain and/or loss asymmetrically inside the loop. If there is no gain fiber placed inside the loop, the configuration is called nonlinear optical loop mirror (NOLM) [DW88]. The case of an asymmetrically placed gain fiber inside the loop is called nonlinear amplifying loop mirror (NALM) [Fer+90]. The latter configuration has the advantage of having an additional degree of freedom in the form of a tunable nonlinear phase difference by variation of the pump power. Generally, the fiber loop implementation has the additional intrinsic advantage of a cancellation of most environmental influences and no need for interferometric alignment due to the propagation of both pulses in the same fibers. This environmental stability can be further enhanced by using polarisation maintaining (PM) fibers.

In the following paragraphs, the operating principles of fiber loops employing 2x2- and 3x3-couplers will be discussed. The power transfer functions are obtained assuming monochromatic, electromagnetic input fields, i.e. CW light, in order to analytically identify the loops' switching characteristics. Qualitatively, these characteristics also hold for a pulsed input as when the loops are used for mode-locking. In a subsequent paragraph, the situation of a Gaussian pulse input is discussed for a 3x3-coupler NALM.

Operating Principle of a NOLM based on a 2x2-Coupler A NOLM can be constructed by connecting the two output ports of an asymmetrical 2x2 fiber coupler [cf. Fig 3.2 (a)]. The fiber coupler has a power splitting ratio of $R : (1-R)$. When an electromagnetic field E_{in} enters on Port 1 of the coupler, it is split whereby a portion of it is transmitted to port 3 and another portion is coupled to port 4, receiving a phase shift of $\pi/2$ with respect to the field on port 3 [DW88]:

$$E_{\mathrm{P3}} = \sqrt{R}E_{\mathrm{in}} \tag{3.2.1}$$

$$E_{\mathrm{P4}} = e^{-i\frac{\pi}{2}}\sqrt{1-R}E_{\mathrm{in}}. \tag{3.2.2}$$

The two fields counter-propagate through the fiber loop and acquire different SPM induced nonlinear phase shifts $\phi_{\mathrm{NL},1}$ and $\phi_{\mathrm{NL},2}$, respectively, due to their different intensities. Back at the coupler both fields are once more split up and interfere with each other. Again, only the fields which are coupled from one fiber to the other, i.e.

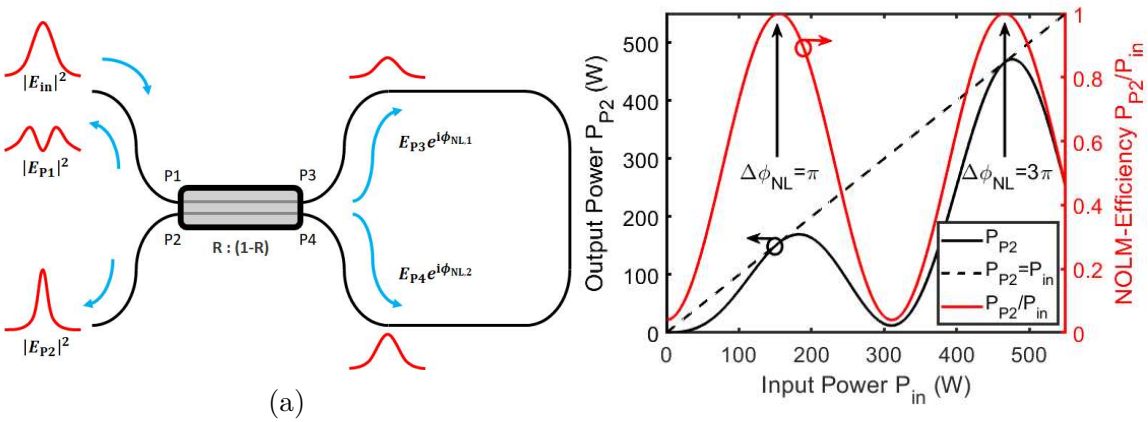

(a) (b)

Figure 3.2: (a) Schematic representation of a NOLM implementation using a 2x2-fiber coupler. (b) Transmission characteristics of a NOLM according to Equation (3.2.6) for a fiber length $L = 3\,\mathrm{m}$, splitting ratio $0.4 : 0.6$, wavelength $\lambda = 1950\,\mathrm{nm}$, nonlinear refractive index $n_2 = 2.5 \times 10^{-20}\,\mathrm{m}^2/\mathrm{W}$ and an effective area of $A = 30\,\mu\mathrm{m}^2$.

from port 3 to port 2 and from port 4 to port 1, receive a phase shift of $\pi/2$. The fields returning from the coupler are consequently given by:

$$E_{\mathrm{P1}} = \left[e^{i\phi_{\mathrm{NL},1}} + e^{i\phi_{\mathrm{NL},2}}\right] e^{-i\frac{\pi}{2}} \sqrt{R(R-1)} E_{\mathrm{in}} \tag{3.2.3}$$

$$E_{\mathrm{P2}} = \left[Re^{i\phi_{\mathrm{NL},1}} + e^{-i\pi}(1-R)e^{i\phi_{\mathrm{NL},2}}\right] E_{\mathrm{in}}. \tag{3.2.4}$$

From the above equations it can be seen that for a vanishing nonlinear phase difference, i.e. $\phi_{\mathrm{NL},1} = \phi_{\mathrm{NL},2}$, constructive interference for port 1 is achieved. In this case the loop can be regarded as a mirror that reflects the electromagnetic field back to the input port. Thus, only a small fraction of the electromagnetic power is transferred to port 2, depending on the value of R. However, if a nonlinear phase difference $\Delta\phi_{\mathrm{NL}} = \phi_{\mathrm{NL},2} - \phi_{\mathrm{NL},1} = \pi$ (or an odd multiple of π) is achieved between the fields, the opposite is the case. Then *all* of the energy is transferred to port 2. Note that for this setup a nonlinear phase difference can only be achieved for an uneven splitting ratio $R \neq 0.5$, since otherwise both fields would experience identical nonlinear phase shifts.

Utilizing that the nonlinear phase shift can be expressed as [DW88]

$$\phi_{\mathrm{NL}} = \frac{2\pi n_2 L |E|^2}{\lambda}, \tag{3.2.5}$$

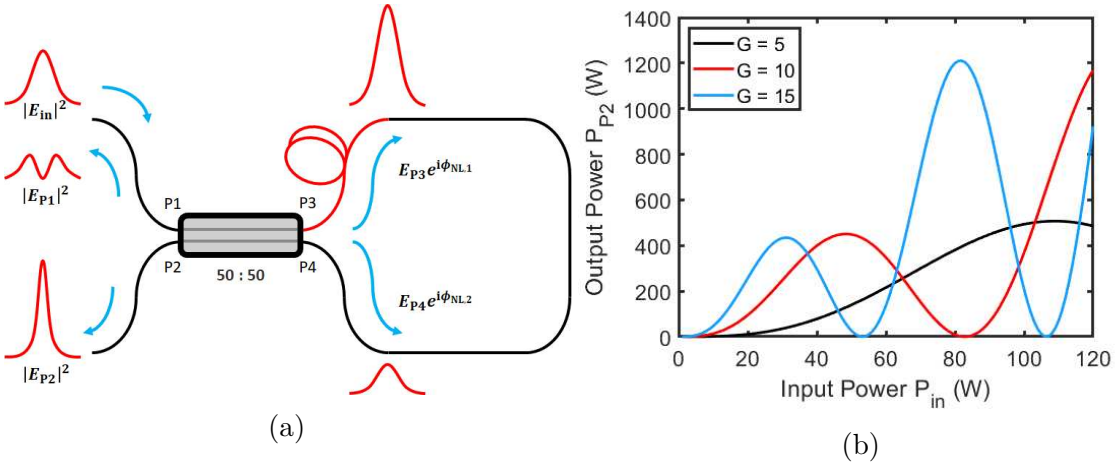

Figure 3.3: (a) Schematic representation of a NALM implementation using a 2x2-fiber coupler. (b) Transmission characteristics of a NALM according to Equation (3.2.8) for fiber length $L = 0.5\,\mathrm{m}$, gain $G = 5$, 10, and 15, splitting ratio $R = 0.5$, wavelength $\lambda = 1950\,\mathrm{nm}$, nonlinear refractive index $n_2 = 2.5 \times 10^{-20}\,\mathrm{m}^2/\mathrm{W}$ and an effective area of $A = 30\,\mu\mathrm{m}^2$.

the following expression for the output power on port 2 P_{P2} can be found [DW88]:

$$P_{\mathrm{P2}} = P_{\mathrm{in}} \left(1 - 2R(1-R)\left\{1 + \cos\left[(1-2R)2\pi n_2 L|E_{\mathrm{in}}|^2/\lambda\right]\right\}\right). \tag{3.2.6}$$

Here L is the length of the fiber loop, n_2 is the nonlinear refractive index of the fiber, and λ is the wavelength of the light. The characteristic transmission for CW light is plotted in Fig. 3.2 (b) for a loop length of $L = 3\,\mathrm{m}$. On the interval $\Delta\phi_{\mathrm{NL}} \in [0, \pi]$ the transmission curve resembles that of a saturable absorber, i.e. for low input powers the relative transmission to port 2 (or NOLM-efficiency) is low and increases for an increasing input power. When launching a pulse into the NOLM whose peak power generates a nonlinear phase difference $\Delta\phi_{\mathrm{NL}}$ of π, the peak of the pulse is efficiently transmitted to port 2. Simultaneously, the less intense pulse wings will generate a nonlinear phase difference smaller than π and are thus transmitted less efficiently to port 2 but rather reflected to port 1 [cf. Fig. 3.2 (a)], causing a reduced pulse width on port 2. Further increasing the input peak power will then again reduce the transmission of the NOLM, as the nonlinear phase difference is greater than π. When using the NOLM as a saturable absorber in a cavity, it is then overdriven, as larger peak powers now experience an increasing loss. This in turn leads to a temporal broadening of the pulse which can destabilise the mode-locking.

Operating Principle of a NALM based on a 2x2-Coupler One drawback of the NOLM-scheme is the fact that high modulation depths require splitting ratios close to $R = 0.5$ resulting in low differential phase shifts between the two loop directions and consequently long loop lengths in order to reach the desired phase difference. In 1990 Fermann *et al.* suggested an extension to the NOLM by adding a gain fiber asymmetrically inside the loop that can solve this problem [Fer+90]. Due to the asymmetrical placement of the fiber, the split electromagnetic fields experience different SPM during the propagation in the loop even when using a $50:50$-coupler. Moreover, the switching behaviour can be tuned variably by changing the pump power and thus the gain in the amplifying fiber.

Assuming that the gain fiber is a lumped element placed directly at port 3 of the coupler, such that the clockwise propagating field is amplified as soon as it enters the loop and the counter-clockwise propagating field is getting amplified just before leaving the loop, the output power at port 2 is given by [Fer+90]

$$P_{\mathrm{P2}} = P_{\mathrm{in}} G \left(1 - 2R(1-R)\left\{1 + \cos\left[(1 - R - GR)2\pi n_2 L |E_{\mathrm{in}}|^2/\lambda\right]\right\}\right), \tag{3.2.7}$$

where G is the gain factor due to the gain fiber. Particularly for a $50:50$-coupler one obtains

$$P_{\mathrm{P2}} = 0.5 P_{\mathrm{in}} G\left\{1 - \cos\left[(G-1)\pi n_2 L |E_{\mathrm{in}}|^2/\lambda\right]\right\}. \tag{3.2.8}$$

The output power at port 2 for CW light is plotted in Fig. 3.3 (b) for different gain values. For mode-locked fiber lasers, the regime in the order of 100 W is of particular relevance, since the peak powers inside the resonator commonly lie in this regime. It can be seen that this regime of input powers can be covered already for a fiber length of 0.5 m with comparably low gain factors of order 10.

Operating Principle of a NALM based on a 3x3-Coupler For a low intensity input the transmissions to port 2 of a NALM based on a 2x2-coupler is close to zero [cf. Fig. 3.4 (b)]. Moreover, the intensity dependence of the transmission is also close to zero for low intensities i.e. there is no intrinsic mechanism that can reliably initiate pulsed operation from a noise input. An incoming long pulse of low intensity will be suppressed by the NALM/NOLM and only experience a minor pulse

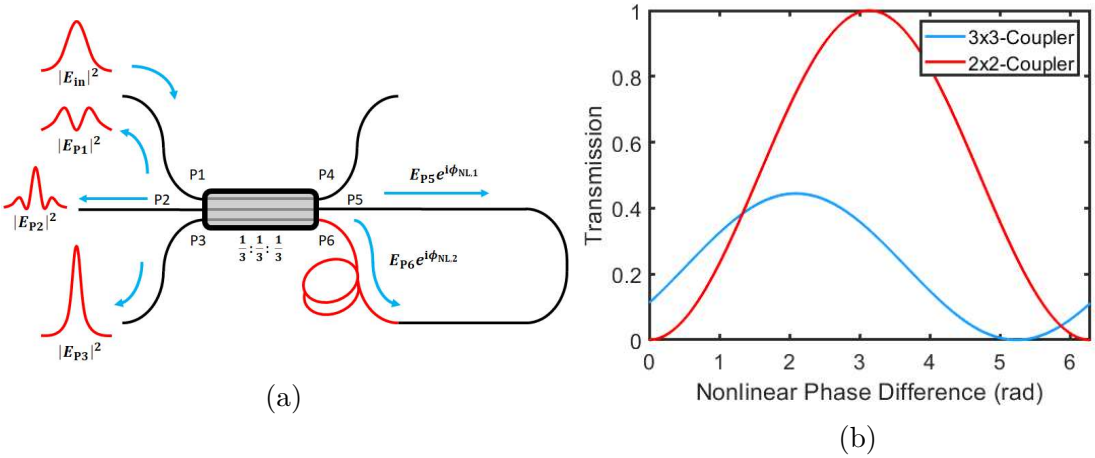

Figure 3.4: (a) Schematic representation of a NALM implementation using a 3x3-fiber coupler. (b) Comparison of transmission characteristics for the 2x2- and the 3x3-coupler NALM for varying nonlinear phase difference between counter-propagating CW-fields. The depicted curve for the 3x3-coupler is valid for the output port 3 if the NALM is arranged as in (a).

shortening. This strongly inhibits the starting of the mode-locked operation from noise in a fiber laser. In practice, this has led to approaches using active methods [NA06; Bau+09] and methods that comprise a non-reciprocal phase shifter inside the loop to initiate mode-locked operation [Hän+13; Jia+16].

A different approach, which does not require any further phase biasing, is based on a symmetric 3x3-coupler instead of a 2x2-coupler [cf. Fig. 3.4 (a)]. The main difference lies in the phase change experienced by the coupled electromagnetic fields, which is $\frac{2\pi}{3}$ for an ideal, even 3x3-coupler [Pri82; Pie89]. Following the same approach as above the transmission of the NALM to port 1, 2, and 3 for the configuration depicted in Fig. 3.4 (a) can be calculated by:

$$P_{\mathrm{P1}} = \frac{2}{9} P_{\mathrm{in}} G \left\{ 1 + \cos\left[\frac{(G-1) 2\pi n_2 L |E_{\mathrm{in}}|^2}{3\lambda} \right] \right\}, \tag{3.2.9}$$

$$P_{\mathrm{P2}} = \frac{2}{9} P_{\mathrm{in}} G \left\{ 1 + \cos\left[\frac{(G-1) 2\pi n_2 L |E_{\mathrm{in}}|^2}{3\lambda} + \frac{2}{3}\pi \right] \right\}, \tag{3.2.10}$$

$$P_{\mathrm{P3}} = \frac{2}{9} P_{\mathrm{in}} G \left\{ 1 + \cos\left[\frac{(G-1) 2\pi n_2 L |E_{\mathrm{in}}|^2}{3\lambda} - \frac{2}{3}\pi \right] \right\}. \tag{3.2.11}$$

The last equation reveals that the power transmitted to port 3 of the coupler is non-

zero already in the absence of gain in the NALM [$P_{\mathrm{P3}}(G = 1) \approx 0.11 \cdot P_{\mathrm{in}}$]. Therefore, incident long pulses will not be suppressed as strongly as by the 2x2-coupler NALM schemes which facilitates the self-starting of the mode-locked operation considerably. Moreover, the slope of the output power on port 3 is non-zero already for low intensities [see also Fig. 3.4 (b)] which allows for better pulse build-up from noise. On the other hand, the overall maximum transmission of the NALM is significantly reduced compared to the 2x2-coupler NALM. Another advantage of the 3x3-coupler NALM is the reduced nonlinear phase difference of $\frac{2\pi}{3}$ that is required for maximum transmission to port 3. This allows for shorter fiber lengths and/or lower gain inside the NALM which permits the construction of fiber oscillators of larger repetition rate. Additionally, a pulse's maximum tolerable nonlinear phase shift experienced per oscillator round trip is limited (see Section 3.3). In this context, a lower nonlinear phase shift inside the NALM is highly favourable.

Model for the Effect of 3x3-Coupler-NALMs on Gaussian Pulses The equations obtained so far are primarily applicable for CW light. When considering a pulsed input to the NALM things generally get more complex, as the parameter space grows. Fiber dispersion, nonlinear phase shift, pulse shape, initial pulse chirp, and interdependencies thereof can influence the resulting transmission behaviour. The emerging time and frequency response of the saturable absorber can thus only be determined by a rigorous numerical treatment, where the partial pulses are propagated through the fibers of the NALM and where the NALM is part of the complete cavity (see Section 3.4).

For now, a simpler model is applied which allows for the identification of the characteristics. The results of this analysis have been published previously in [Gra+22]. In the model, the situation in Fig. 3.4 (a) shall me mimicked, where port 1 is the input and port 3 is the output of the saturable absorber. Therefore, a Gaussian pulse $A_0(t)$ with 200 fs FWHM pulse duration, which enters the NALM on port 1, is chosen as starting point. The pulse is split into three partial pulses of equal amplitude. The first pulse exits the NALM on port 4, whereas the two coupled partial pulses on port 5 (pulse 2) and port 6 (pulse 3) both experience a phase shift of $\frac{2\pi}{3}$ due to the coupler, i.e. there is no resulting phase difference between both pulses at this point. Afterwards, pulse 3 experiences a nonlinear phase shift proportional to

the normalised pulse envelope squared

$$A_3(t) = \frac{A_0(t)}{\sqrt{3}} \exp\left(i\kappa \frac{|A_0(t)|^2}{\max\left[|A_0(t)|^2\right]}\right), \tag{3.2.12}$$

in order to mimic the effect of SPM, whereas pulse 2 is left unchanged $A_2(t) = \frac{A_0(t)}{\sqrt{3}}$. Thus, the parameter κ represents a direct measure for the nonlinear phase difference $\Delta\phi_{\mathrm{NL}}$ between the two pulses and is varied to study the NALM characteristics. Both pulses are now distributed back to the ports 1, 2, and 3. Thereby only the coupled fields receive a phase shift of $\frac{2\pi}{3}$. The resulting time signals are obtained by a coherent summation of the pulses 2 and 3:

$$|A_{\mathrm{Port1}}(t)|^2 = |A_2(t)e^{-i\cdot 2\pi/3} + A_3(t)e^{-i\cdot 2\pi/3}|^2/3, \tag{3.2.13}$$

$$|A_{\mathrm{Port2}}(t)|^2 = |A_2(t)e^{-i\cdot 2\pi/3} + A_3(t)|^2/3, \tag{3.2.14}$$

$$|A_{\mathrm{Port3}}(t)|^2 = |A_2(t) + A_3(t)e^{-i\cdot 2\pi/3}|^2/3. \tag{3.2.15}$$

Figure 3.5 shows results obtained by the model. One notable result is that the maximum relative transmission to port 3 (39 % with respect to the input on port 1) is not achieved at a nonlinear phase difference of $\Delta\phi_{\mathrm{NL}} = 2\pi/3\,\mathrm{rad} \approx 2.09\,\mathrm{rad}$ (where constructive interference for the pulse peak is obtained), but at 2.53 rad [see Fig. 3.5 (a)]. This implies that at maximum efficiency of the NALM, the output peak intensity has already decreased again, which leads to a slight flattening of the pulse peak compared to the original pulse [see Fig. 3.5 (c)]. Nevertheless, the pulse duration is reduced by 6 % due to the NALM, as the wings, which experience less nonlinear phase shift, do not interfere constructively to port 3. Overall, port 3 provides a pulse width reduction for $\Delta\phi_{\mathrm{NL}}$ between 0 and 2.78 rad [see Fig. 3.5 (b)]. The modulation depth is $\Delta q = 1 - \min\left(P_{\mathrm{Port3}}\right)/\max\left(P_{\mathrm{Port3}}\right) \approx 71\,\%$. Even though the ports 1 and 2 provide larger pulse duration reductions and modulation depths, they are not suitable as saturable absorber exits since they also exhibit a pulse duration increase and negative transmission slope for lower $\Delta\phi_{\mathrm{NL}}$ which will inhibit the pulse build up.

The behaviour discussed so far remains unchanged when adding a linear initial chirp to the pulse, as this does not alter the Gaussian pulse shape. However, the spectra of the coupled pulses significantly change when the input pulse is initially

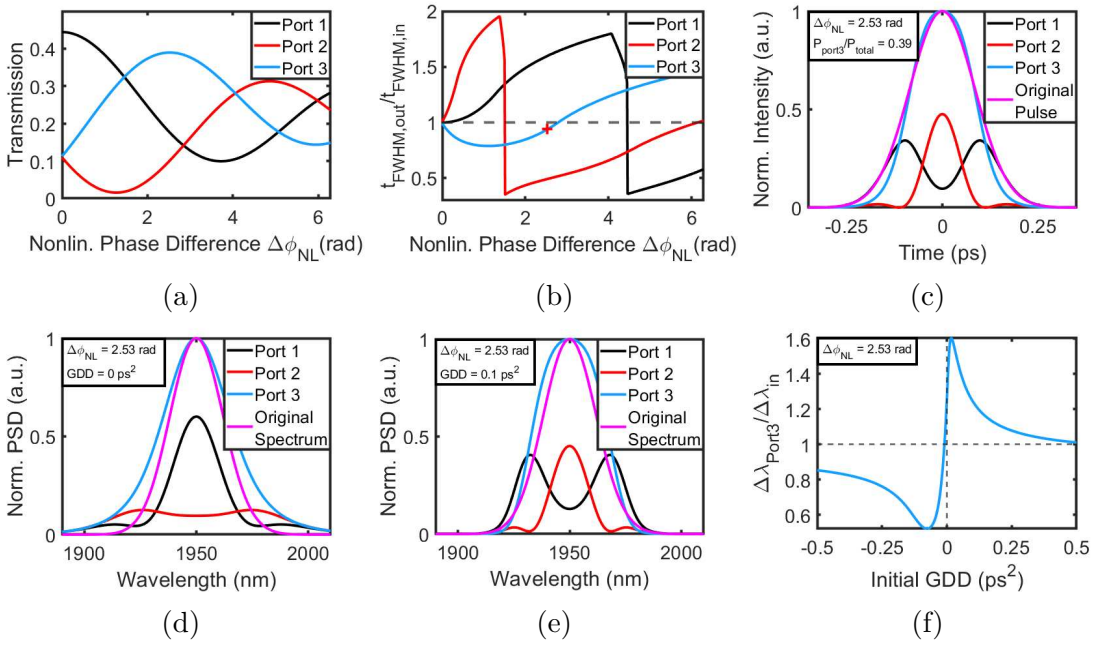

Figure 3.5: Analysis of the pulse transmission characteristics of the 3x3-coupler in the model. (a) Relative transmission to port 1, 2, and 3 as a function of the applied nonlinear phase difference $\Delta\phi_{\mathrm{NL}}$ between the split pulses. (b) Pulse width change of the pulses at port 1, 2, and 3 as a function of $\Delta\phi_{\mathrm{NL}}$. The red marker indicates the position of maximum relative transmission at port 3. (c) Time profiles of the original pulse and the recombined pulses at port 1, 2, and 3 for the case of maximum transmission to port 3, i.e. $\Delta\phi_{\mathrm{NL}} = 2.53\,\mathrm{rad}$. The original pulse amplitude is scaled down to the amplitude at port 3 for better comparison. (d) Corresponding output spectra for an initially unchirped pulse: GDD $= 0\,\mathrm{ps}^2$. (e) Corresponding output spectra of an initially up-chirped pulse GDD $= 0.1\,\mathrm{ps}^2$, chirped FWHM pulse duration 1.4 ps. The original spectrum is scaled down to the spectrum at port 3 for better comparison. (f) Relative change of the FWHM bandwidth of the spectra at port 3 at maximum transmission in dependence of the initial GDD.

chirped. The unchirped pulse generates the spectra seen in Fig. 3.5 (d), with long tails at port 3, a dipped spectrum at port 2, and a narrow spectrum with shoulders at port 1. Adding a positive GDD of $0.1\,\mathrm{ps}^2$ (chirped pulse duration 1.4 ps), the spectra change to a strongly dipped spectrum now observed at port 1 and a narrow spectrum with shoulders at port 2 [see Fig. 3.5 (e)]. Overall, these spectra strongly resemble the temporal characteristics of the corresponding pulses [compare to Fig. 3.5 (c)]. This time-domain to frequency-domain correspondence is caused by the strong linear chirp of the pulse which approximately linearly maps every point in time of the pulse to a corresponding instantaneous frequency. For moderately positive values of the

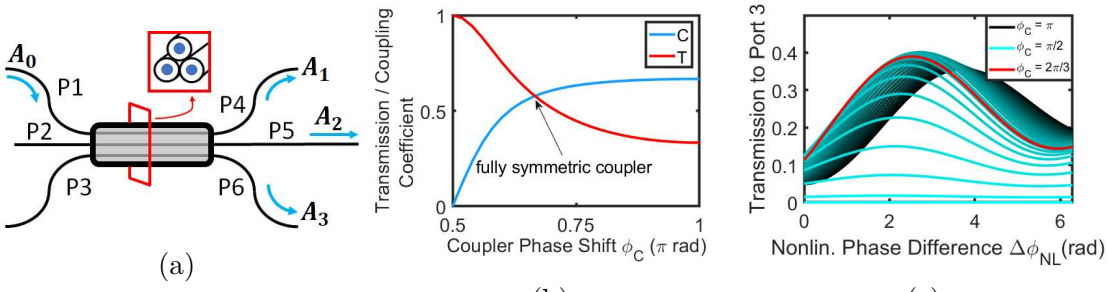

(a) (b) (c)

Figure 3.6: Analysis of the pulse transmission of the 3x3-coupler for varying coupler parameters in the model. (a) Scheme of the considered 3x3-coupler. (b) Relationship between the coupler phase shift ϕ_C and the transmission / coupling coefficients T and C of the coupler. (c) Transmission to port 3 as a function of the applied nonlinear phase difference $\Delta\phi_{NL}$ between the split pulses. Different lines correspond to different coupler phase shifts ϕ_C, ranging from $\pi/2$ (brightest) to π (darkest) in steps of 0.02π.

initial GDD this results in a broadening of the spectrum at port 3 compared to the initial spectrum [see Fig.3.5 (f)], with a maximum broadening of 60 % at 0.017 ps^2 (chirped pulse duration 310 fs). On the other hand, negative values of the initial GDD below -0.01 ps^2 will lead to a reduction of the spectral width.

Finally, the influence of the coupler's parameters on the transmission to port 3 is studied. In general, the 3x3-coupler does not need to be fully symmetric in terms of the transmitted and coupled fields. However, the analysis is restricted to a *geometrically* symmetric cross section of the coupler, i.e. the three fibers inside the coupler are arranged as in Fig. 3.6 (a). For this symmetric arrangement, the coupling coefficient C, for example, from port 1 to port 5 is equal to the one from port 1 to port 6 [FCI96]. An input pulse A_0 on port 1 is thus divided to ports 4, 5, and 6 according to

$$A_1(t) = T \cdot A_0(t), \tag{3.2.16}$$

$$A_2(t) = C \cdot e^{-i\cdot\phi_C} A_0(t), \tag{3.2.17}$$

$$A_3(t) = C \cdot e^{-i\cdot\phi_C} A_0(t). \tag{3.2.18}$$

If furthermore energy conservation is assumed, the transmission/coupling coefficients

(T and C) and the coupler phase shift ϕ_C are connected by [FCI96]

$$T^2 + 2C^2 \stackrel{!}{=} 1 \qquad \text{and} \qquad \cos(\phi_\mathrm{C}) \stackrel{!}{=} -\frac{C}{2T}. \tag{3.2.19}$$

Figure 3.6 (b) shows T and C in dependence of ϕ_C. For the case of a fully symmetric coupler $C = T = 1/\sqrt{3}$ and $\phi_\mathrm{C} = 2\pi/3$ are restored. The phase shift ϕ_C is bounded by $\pi/2$ and π, for weak ($C \to 0$) and maximum ($C = 2T = 2/3$) coupling between the fibers, respectively. In contrast to the 2x2-coupler, 100%-coupling is not possible with this type of coupler and a minimum of $1/3^2 \approx 11\%$ of the launched power stays in the input fiber even for maximum coupling.

Intuitively, one could assume that a lower transmission coefficient T might increase the efficiency of the 3x3-coupler-NALM, as less power is lost to port 4. However, on the return path also less power is transmitted from port 6 to port 3. Figure 3.6 (c) shows the transmission curves of the 3x3-coupler-NALM to port 3 for varying coupler parameters in the model. For maximum coupling (black curve, $\phi_\mathrm{C} = \pi$) the NALM has a vanishing transmission slope to port 3 at $\Delta\phi_\mathrm{NL} = 0\,\mathrm{rad}$ and a maximum transmission of 36% at $\Delta\phi_\mathrm{NL} \approx 3.7\,\mathrm{rad}$, which refutes the previous conjecture. A weaker coupling (brighter curves) results in larger transmission and increasing slope for $\Delta\phi_\mathrm{NL} = 0\,\mathrm{rad}$ and a shift of the transmission maximum towards lower $\Delta\phi_\mathrm{NL}$. The maximum transmission of 40% is obtained for $\phi_\mathrm{C} = 2.26\,\mathrm{rad}$ at $\Delta\phi_\mathrm{NL} \approx 2.71\,\mathrm{rad}$. Further decreasing the phase bias, then again results in a shift of the transmission maximum's position towards even lower $\Delta\phi_\mathrm{NL}$ and a lower maximum transmission. For $C = 0$ the transmission to port 3 vanishes independently of the nonlinear phase shift, as the power is completely transmitted to port 4.

In summary, a shift of the coupling parameters away from the symmetric parameters ($C = T$) is not expected to increase the performance of the 3x3-coupler-NALM noteworthily. Overall, the maximum transmission can be increased from 39 to 40 %, however at the cost of an increased nonlinear phase difference of 2.71 rad instead of 2.53 rad within the NALM.

3.3 Survey of Pulse Formation Regimes

In this section the most prominent pulse formation regimes for the generation of sub-ps pulses in fiber oscillators shall be reviewed. In the context of this work, seed sources for all-fiber nonlinear CPA-systems are of particular interest. In the end, the regimes are assessed in terms of their suitability for this purpose.

Apart from the saturable absorber described in the previous section, there are numerous other components and effects inside a mode-locked fiber laser that affect the pulse shaping. The most relevant of these effects can be described using the extended nonlinear Schrödinger equation (NLSE) that includes gain and loss [see Equation (2.3.4)]

$$\frac{\partial A(z,t)}{\partial z} = \underbrace{-\frac{\alpha}{2}A(z,t)}_{\text{gain/loss}} \underbrace{-i\frac{\beta_2}{2}\frac{\partial^2}{\partial t^2}A(z,t)}_{\text{GVD}} \underbrace{+i\gamma|A(z,t)|^2A(z,t)}_{\text{SPM}}, \tag{3.3.1}$$

where $A(z,t)$ represents the slowly-varying envelope function of a pulse evolving in a dispersive, third-order nonlinear medium ($\chi^{(2)} = 0$, $\chi^{(3)} \neq 0$). The variables z and t are the propagation distance and the time in a moving frame of reference of the pulse, respectively. The gain and loss of the pulse are modelled by α, the dispersive effects due to GVD are included in β_2. The last term on the right-hand side of the equation represents the influence of SPM. It includes the nonlinear coefficient $\gamma = n_2\omega_0/(cA_{\text{eff}})$, where n_2 again is the nonlinear refractive index and A_{eff} is the effective area of the transverse fiber mode. In general, the above equation can be amended to also include self-steepening, Raman shift and/or higher-order dispersive effects [as in Equation (2.3.10)]. However, for pulse durations $> 100\,\text{fs}$ and small peak powers, as they are often obtained in fiber oscillators, they can be largely omitted.

3.3.1 Soliton Fiber Lasers

In the absence of gain and loss ($\alpha = 0$) and for anomalous dispersion ($\beta_2 < 0$) Equation (3.3.1) possesses a fundamental soliton solution that has a sech-shaped envelope [Boy20]

$$A(z,t) = A_0\text{sech}\left(\frac{t}{t_0}\right)e^{i\frac{1}{2}\gamma|A_0|^2z}, \tag{3.3.2}$$

with A_0 and t_0 being the amplitude and the pulse duration, respectively. As can be seen from Equation (3.3.2) the pulse shape of the soliton does not change during propagation, which is achieved by a continuous balance between the SPM-induced and the GVD-induced frequency modulations during propagation. A key property of this solution is the soliton area theorem, which states that

$$A_0 t_0 = \sqrt{\frac{|\beta_2|}{\gamma}}. \tag{3.3.3}$$

For a given pulse duration t_0, the peak power $P_\mathrm{P} = |A_0|^2$ and thereby also the pulse energy are fixed by the fiber parameters β_2 and γ, accordingly.

In practice, a mode-locked fiber oscillator consists of a variety of discrete components, rendering periodically varying sections of dissipation and amplification as well as dispersion and SPM inevitable. As a result, pulse duration and peak power are varying quantities in the course of one round trip. Yet, the mode-locked laser can still support stable *average solitons*, if the overall balance between SPM and anomalous dispersion is maintained and provided that the period, over which these perturbations occur (i.e. the resonator length z_R), is short compared to the so-called soliton period z_0 [BD91; Kel+91]

$$z_\mathrm{R} \ll z_0 = \frac{\pi t_0^2}{2|\beta_2|}. \tag{3.3.4}$$

The condition $z_\mathrm{R} \ll z_0$ ensures, that pulse shaping effects due to varying GVD and SPM occur on a length scale, which is much larger than the resonator length [TBF12]. Under this condition the soliton area theorem remains valid for the average soliton with regard to its cavity averaged amplitude $\langle A_0 \rangle$ and pulse duration $\langle t_0 \rangle$, despite large changes in pulse energy that may occur over one round trip.

Unfortunately, small pulse durations in the sub-picosecond regime cause the soliton period to become comparable to or even smaller than the resonator length, thus the above condition can hardly be met [Tam+93]. Still, despite the deviations from the average soliton regime, soliton lasers have been found to permit stable operation. However, the periodic perturbations now have a stronger influence on the pulse as z_0 approaches z_R leading to a series of peaks generated in the spectrum of the soliton [see Fig. 3.7 (a)]. These peaks were first explained by S.M.J. Kelly and

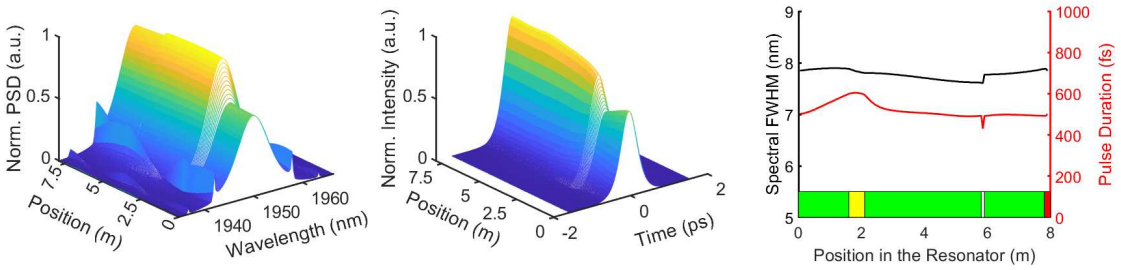

(a) (b) (c)

Figure 3.7: Simulation of exemplary propagation dynamics of a mode-locked soliton fiber laser based on the split-step Fourier method (see. Chapter 3.4). (a) Spectral evolution of the pulse envelope inside the simulated resonator. (b) Temporal evolution of the pulse envelope inside the resonator. (c) Evolution of spectral width and pulse duration inside the resonator. The green, yellow, white, and red sections are anomalous dispersive fiber $\beta_2 = -0.06\,\mathrm{ps}^2$, gain fiber, saturable absorber, and outcoupler, respectively. Despite substantial changes in pulse energy due to gain and outcoupling, the spectral width and the pulse duration only show a small variation.

are thus often called Kelly sidebands [Kel92].

Kelly Sideband Generation In order to comply with the area theorem in spite of the perturbations, the soliton will discard parts of its energy. The discarded waves are not able to sustain the same temporal stability as the soliton, since they experience negligible SPM and thus broaden due to the sole effect of chromatic dispersion. However, for certain frequency components the difference between the phases of the dispersive waves ϕ_{DW} and the soliton ϕ_{S} reaches an integer multiple of 2π per cavity round trip

$$\phi_{\mathrm{S}}(z_{\mathrm{R}}) - \phi_{\mathrm{DW}}(z_{\mathrm{R}}) \stackrel{!}{=} 2\pi m \qquad m \in \mathbb{N}, \tag{3.3.5}$$

resulting in resonantly enhanced peaks in the laser spectrum [Pan+92].

In a leading order assessment, the phase-matching Equation (3.3.5) can be used to determine the spectral positions of the sidebands [Nel+97]. The phase of the dispersive wave is mainly influenced by GVD and thus scales quadratically with $\Delta\omega := \omega - \omega_0$

$$\phi_{\mathrm{DW}}(z_{\mathrm{R}}) = -\frac{1}{2}\Delta\omega^2 \langle|\beta_2|\rangle z_{\mathrm{R}}, \tag{3.3.6}$$

where $\langle|\beta_2|\rangle$ is the cavity averaged GVD of the fibers. The phase acquired by the soliton on the other hand does in first approximation not depend on the frequency $\Delta\omega$

$$\phi_{\mathrm{S}}(z_{\mathrm{R}}) \overset{(3.3.2)}{=} \frac{1}{2}\langle\gamma\rangle\langle|A_0|\rangle^2 z_{\mathrm{R}} \overset{(3.3.3)}{=} \frac{1}{2}\frac{\langle|\beta_2|\rangle z_{\mathrm{R}}}{\langle t_0\rangle^2}. \tag{3.3.7}$$

The phase-matched frequencies, at which the enhanced dispersive waves show up in the spectra, can then promptly be obtained using Equation (3.3.5)

$$\Delta\omega_m = \pm\frac{1}{\langle t_0\rangle}\sqrt{\frac{4\pi m\langle t_0\rangle^2}{\langle|\beta_2|\rangle z_{\mathrm{R}}} - 1} = \pm\frac{1}{\langle t_0\rangle}\sqrt{\frac{8mz_0}{z_{\mathrm{R}}} - 1}. \tag{3.3.8}$$

In general, the sideband intensity is proportional to the intensity of the soliton at the particular frequency, causing a decreased intensity for the peaks further away from the center frequency. For $z_{\mathrm{R}} \ll z_0$ the first sidebands appear far outside of the relevant spectral range and are thus strongly suppressed.

Though, according to Equation (3.3.8) the sideband position is in first approximation symmetric with respect to the center frequency, the sideband intensity typically is not. This can be attributed to numerous factors as for example the gain profile, other filtering components inside the cavity, and higher-order dispersion [DD94].

In principle, the area theorem (3.3.3) does not forbid arbitrarily small pulse durations with correspondingly high peak powers, yet pulse durations smaller than 100 fs are hardly observed in mode-locked soliton fiber lasers. Ultimately, this can be understood by the existence of the sidebands which imposes a limitation in terms of the achievable pulse energy and duration in a soliton laser. For example, assuming that the soliton phase shift per resonator round trip $\phi_{\mathrm{S}}(z_{\mathrm{R}})$ was equal to 2π: Eqs. (3.3.5) and (3.3.6) imply that phase matching with the dispersive wave would then already be obtained for the center frequency $\Delta\omega_1 = 0$. Thereby, the first order sidebands would both be shifted to the center of the spectrum, leading to a strong coupling to the dispersive waves which would quickly destabilise the pulse. The accumulated nonlinear phase of the soliton is thus limited to values smaller than 2π per round trip, which in turn limits the achievable pulse peak power according to Equation (3.3.7) and thus also the pulse energy. Moreover, Equation (3.3.8) reveals that for $\Delta\omega_1 = 0$ the soliton period $z_0 = z_{\mathrm{R}}/8$ would be minimal, which also poses a

lower limit to the achievable pulse duration as $z_0 \propto \langle t_0 \rangle^2$.

Another limiting factor typically setting in before the soliton phase shift of 2π is reached, is the soliton quantisation effect, which causes a splitting of the soliton into multiple solitons inside the oscillator due to excessive nonlinear phase shift [Tan+05].

Finally, it can be stated that an inherent problem in achieving ever shorter solitons is situated in the need for stronger SPM to generate additional frequency components, whereas the nonlinear phase shift due to SPM also causes instability issues. In order to overcome this limitation, different pulse shaping regimes, where GVD and SPM do not compensate each other perpetually, have been explored. One approach is the dispersion-managed soliton oscillator which will be examined in the next section. Furthermore, one could abandon the solitonic pulse shaping completely by further reducing/avoiding anomalous dispersion inside the cavity. In the presence of normal dispersion and SPM, the pulses will broaden spectrally as well as temporally, leading to strongly chirped pulses in the cavity. The pulse shaping in these lasers will be examined in the subsequent sections.

3.3.2 Dispersion Managed Soliton Fiber Lasers

In 1993, a mode-locked Er-fiber laser has been demonstrated in which a normal dispersion fiber is employed inside the cavity, allowing pulse durations below 100 fs [Tam+93]. The general idea is that the cavity consists of fibers of different signs of dispersion, which cause the pulse to periodically stretch and compress (see Fig. 3.8) due to the corresponding sign change of the chirp. Such a temporally "breathing" pulse may vary in pulse duration by over an order of magnitude, effectively reducing the average value of its peak power [Hau+95]. The accumulated nonlinear phase can thus be significantly lowered, shifting the thresholds for the onset of instabilities and multi-pulsing towards larger pulse energies. Using appropriate fiber lengths, the cavity averaged dispersion can be kept close to zero which shifts the position of the sidebands away from the center frequency. As the energy coupling to the dispersive waves is proportional to the soliton's energy at the respective frequency, the sidebands are strongly suppressed, resulting in cleaner output spectra. In this regime, the pulse can no longer be approximated as a conventional average soliton, which also manifests in the spectral and temporal shape changing towards a Gaussian. In fact, the spectral shape also evolves strongly [see Fig.3.8 (a)], which is due to the

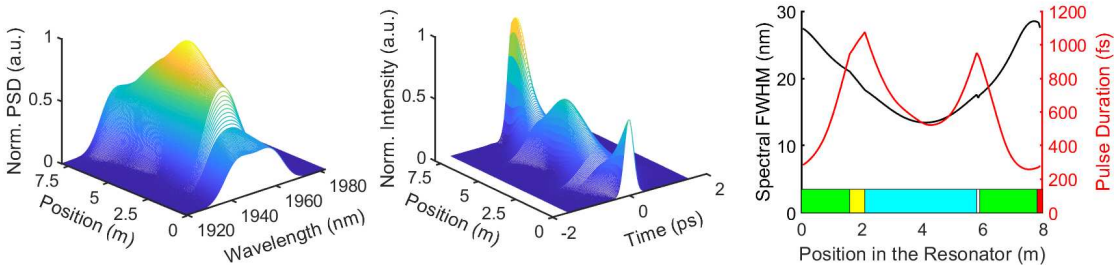

(a) (b) (c)

Figure 3.8: Simulation of exemplary propagation dynamics of a mode-locked dispersion managed soliton fiber laser based on the split-step Fourier method (see. Chapter 3.4). (a) Spectral evolution of the pulse envelope inside the simulated resonator. (b) Temporal evolution of the pulse envelope inside the resonator. (c) Evolution of spectral width and pulse duration inside the resonator. The green, yellow, blue, white, and red sections are anomalous dispersive fiber $\beta_2 = -0.06\,\mathrm{ps}^2$, gain fiber, normal dispersive fiber $\beta_2 = 0.06\,\mathrm{ps}^2$, saturable absorber, and outcoupler, respectively. In the first half of the resonator (0-4 m) the pulse is down-chirped, which leads to a reduction of spectral width in the interplay with SPM. When the chirp flips its sign in the middle of the resonator, the spectral width increases again, resulting in the characteristic breathing of the pulse.

fact that the chirp of the pulse changes signs during one round trip. The interplay between SPM and the chirp, however, determines whether the spectrum will broaden (up-chirp, caused by normal dispersion) or become narrower (down-chirp, caused by anomalous dispersion) during propagation [Agr07]. Thus, the pulse breathes not only temporally but also spectrally. In consequence, the outcoupling position influences the obtainable spectral bandwidth. Generally, the bandwidth is larger compared to the average soliton laser due to the spectral broadening induced by SPM of the up-chirped pulse, which typically allows for smaller compressed pulse durations.

3.3.3 Self-Similar Fiber Lasers

Even though gain and loss are unavoidable in mode-locked soliton lasers, their existence can be regarded as perturbation to the solitonic propagation. Yet, apart from the conventional soliton and the DMS there exist different types of attractors of the nonlinear propagation equation, which have been discovered in the pursuit of larger pulse energies and smaller pulse durations.

One such type is the self-similar fiber laser (see Fig. 3.9). In the presence

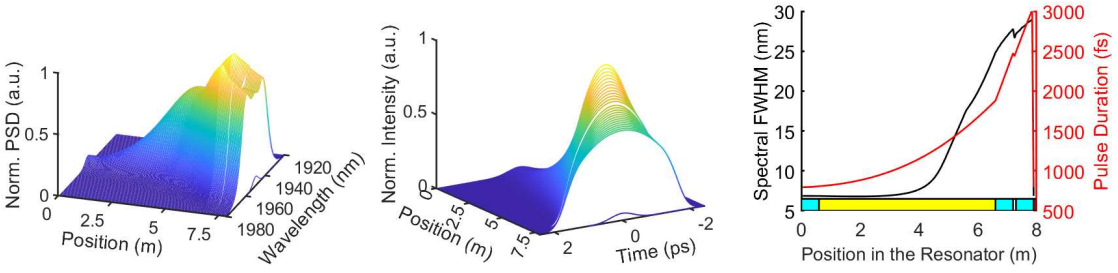

(a) (b) (c)

Figure 3.9: Simulation of exemplary propagation dynamics of a mode-locked self-similar fiber laser based on the split-step Fourier method (see Chapter 3.4). (a) Spectral evolution of the pulse envelope inside the simulated resonator. (b) Temporal evolution of the pulse envelope inside the resonator. (c) Evolution of spectral width and pulse duration inside the resonator. The blue, yellow, white, and red sections are normally dispersive fiber $\beta_2 = 0.06\,\mathrm{ps}^2$, gain fiber, saturable absorber, and Gaussian spectral filter, respectively.

of normal dispersion ($\beta_2 > 0$) and constant gain ($\alpha > 0$), there exists an exact asymptotic solution to the modified NLSE (3.3.1) that has a parabolic pulse shape and scales self-similarly during amplification [Fer+00]. The asymptotic solution is given by [Kru+02]

$$A(z,t) = \begin{cases} A_0 e^{\frac{\alpha z}{3}} \sqrt{1 - \frac{t^2}{t_\mathrm{p}^2(z)}}\, e^{i\phi(z,t)} & \text{for } |t| < t_\mathrm{p} \\ 0 & \text{for } |t| \geq t_\mathrm{p} \end{cases} \quad \text{with} \tag{3.3.9}$$

$$A_0 = \frac{1}{2}\left(\frac{\alpha U_\mathrm{in}(z=0)}{\sqrt{\gamma\beta_2/2}}\right)^{\frac{1}{3}}, \quad t_\mathrm{p}(z) = \frac{6\sqrt{\gamma\beta_2/2}}{\alpha} A_0 e^{\frac{\alpha z}{3}}, \quad \phi(z,t) = \phi_0 + \frac{3\gamma A_0^2}{2\alpha} e^{\frac{2\alpha z}{3}} - \frac{\alpha t^2}{6\beta_2}. \tag{3.3.10}$$

Here, U_in is the input pulse energy and ϕ_0 is an arbitrary constant phase. As the asymptotic solution acquires a linear chirp ($\partial\phi/\partial t \propto -t$) during propagation, the corresponding spectrum must be of parabolic shape as well

$$|\tilde{A}(z,\bar{\omega})|^2 = \begin{cases} \frac{3\beta_2 A_0^2}{\alpha} e^{\frac{2\alpha z}{3}} \left[1 - \frac{\bar{\omega}^2}{\omega_\mathrm{p}^2(z)}\right] & \text{for } |\bar{\omega}| < \omega_\mathrm{p} \\ 0 & \text{for } |\bar{\omega}| \geq \omega_\mathrm{p} \end{cases} \quad \text{with} \tag{3.3.11}$$

$$\omega_\mathrm{p}(z) = \sqrt{\frac{2\gamma}{\beta_2}} A_0 e^{\frac{\alpha z}{3}}, \quad \bar{\omega} = \omega - \omega_0. \tag{3.3.12}$$

It can be seen, that both the FWHM pulse duration $\sqrt{2}t_\mathrm{p}$ and the FWHM spec-

tral bandwidth $\sqrt{2}\omega_\mathrm{p}$ increase exponentially during propagation. In reality, the exponential growth of the bandwidth is, however, limited by the available gain bandwidth of the active fiber and by the available pump power. A key advantage of the parabolic pulses is that they can propagate in the normal dispersion regime without wave-breaking [TSJ85; And+93] despite large pulse energies. Moreover, the linear chirp can be easily compressed after amplification. Concerning the construction of a mode-locked oscillator, self-consistency is required over the course of one round trip. Therefore, the strongly chirped pulses can be temporally narrowed by an anomalous dispersive component and/or by a spectral filter. When the short pulses reenter the active fiber, they will again reshape towards the parabolic solution determined by the active fiber's parameters. The increased chirp compared to the DMS and resistance to optical wave-breaking allow for a larger pulse energy in the cavity.

3.3.4 Dissipative-Soliton Fiber Lasers

Apart from the self-similar regime, there is the dissipative soliton (DS) regime [Cho+06; RCW07], which exists in all (or mostly) normally dispersive cavities (see Fig. 3.10). Herein, the pulse shaping relies on a balance between SPM, GVD, gain, and spectral filtering, which is essentially a dissipative process. During propagation the pulse broadens spectrally as well as temporally [see Fig. 3.10 (c)] due to the simultaneous action of SPM and the up-chirp caused by the normal dispersion of the fiber. The spectral filter then resets the pulse to its initial state by truncating the spectrum as well as the pulse wings due to the large chirp [see Fig. 3.10 (a), (b)]. Generally, the interplay between SPM and normal dispersion can lead to M-shaped spectra with steep edges, however the exact output spectra also strongly depend on the spectral width and shape of the filter [CRW07], the resonator dispersion, and the total nonlinear phase-shift. The resulting pulse energies can be in the range of tens of nJ with sub-50 fs compressible pulse durations [Chi+12].

3.3.5 Mamyshev Fiber Lasers

A Mamyshev fiber laser[1] consists of two amplifying sections which are separated by two spectrally offset, narrow band-pass filters. The offset ensures that emerging

[1] Named after the Mamyshev pulse regenerator used in telecommunication [Mam98].

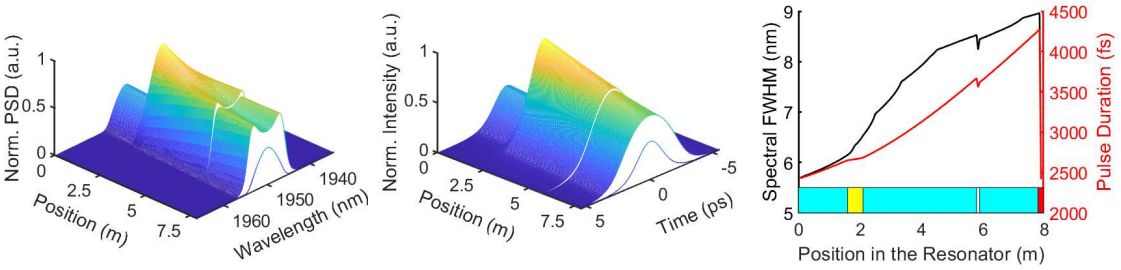

(a) (b) (c)

Figure 3.10: Simulation of exemplary propagation dynamics of a mode-locked all-normal dispersion (AND) fiber laser based on the split-step Fourier method (see Chapter 3.4). (a) Spectral evolution of the pulse envelope inside the simulated resonator. (b) Temporal evolution of the pulse envelope inside the resonator. (c) Evolution of spectral width and pulse duration inside the resonator. The blue, yellow, white, and red sections are normal dispersive fiber $\beta_2 = 0.06\,\mathrm{ps}^2$, gain fiber, saturable absorber, and Gaussian spectral filter, respectively. The interplay between normal dispersion and SPM leads to a spectral as well as temporal broadening, which is reset by the spectral filter at the end of the cavity.

narrow-band CW-light will be suppressed and only high intensity pulsed light, which generates enough spectral broadening via SPM to span the spectral separation between the filters, is able to propagate in the cavity (see Fig. 3.11). As this mechanism by itself favors pulsed over CW-light, in principle no further saturable absorber should be required. Practically, however, the suppression of low intensity fluctuations hinders the self-start from noise [Sid+18]. Therefore, different techniques have been explored that can initiate mode-locking, such as pulse injection from an external source [Liu+17; Rep+19], generation of gain-switched seed pulses via pump modulation [SBG17] or self-injection by a separate cavity that incorporates an additional saturable absorber [Sid+18; Bou+20].

Once started, Mamyshev oscillators can reach unprecedented performance levels including µJ-pulses which can be directly compressed to sub-50 fs by a grating pair [Liu+19]. This performance leap is enabled by largely relaxed constraints concerning the intracavity nonlinear phase shift. In contrast to the aforementioned schemes (DS and self-similar fiber laser), which are limited to nonlinear phase shifts in the range of 10π [Fu+18], for the Mamyshev oscillators nonlinear phase shifts as large as 60π have been reported [Liu+17].

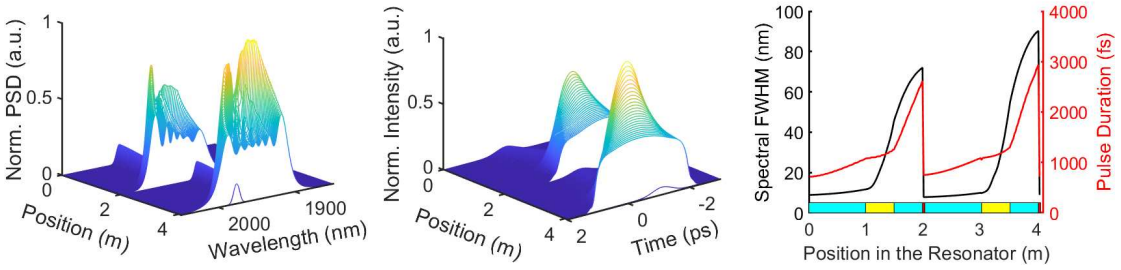

(a) (b) (c)

Figure 3.11: Simulation of exemplary propagation dynamics of a mode-locked Mamyshev fiber laser based on the split-step Fourier method (see Chapter 3.4). (a) Spectral evolution of the pulse envelope inside the simulated resonator. (b) Temporal evolution of the pulse envelope inside the resonator. (c) Evolution of spectral width and pulse duration inside the resonator. The blue, yellow, and red sections are normal dispersive fiber $\beta_2 = 0.06\,\mathrm{ps}^2$, gain fiber, and Gaussian spectral filter, respectively. The central wavelengths of the two spectral filters (bandwidth 8 nm each) are separated by 25 nm, which ensures that only spectrally broadened pulses can propagate in the cavity.

3.3.6 Conclusions

All of the aforementioned pulse formation mechanisms provide their own particular advantages and disadvantages. In the context of this work, seed sources for nonlinear fiber CPA systems, which eventually generate femtosecond pulses in the 100 µJ regime at a 100 W average power level, are of particular interest. A high pulse energy output from the oscillator only plays a secondary role in this regard and can be even detrimental, as significant SPM can be generated prior to stretching in an all-fiber setup. Instead, the basic requirement for this deployment is a robust, self-starting femtosecond oscillator that allows for reproducible, smooth spectral shapes which generate compressible nonlinear phases during propagation of the subsequently stretched and amplified pulses (see Section 3.5).

With this in mind, the close-to-ideal spectral shape would be a parabola. For the strongly stretched pulse, the spectral shape is mapped to the time domain. A pulse with a parabolic temporal profile subsequently generates a parabolic nonlinear phase which can be compressed with only minor deterioration in pulse quality despite B-integral levels of >10 rad during the amplification process. Contrarily, any steep features or modulations in the spectrum will generate nonlinear phases that are virtually incompressible using a grating type compressor, as the Taylor expansion

of the spectral phase includes significant shares of higher-order terms. Besides, periodic spectral modulations or phase modulations of the seed are an effective way of coupling energy from the main pulse to side pulses in a nonlinear CPA-system, which degrades the pulse contrast (see Section 3.5). Therefore, the soliton, the DS, and the Mamyshev fiber laser appear unsuitable due to the Kelly-sidebands or the spectral features caused by SPM, respectively. Intuitively the self-similar laser is a good candidate, however, truly parabolic spectral shapes are rarely reported for this type of laser [CWW15]. The spectra of the DMS on the other hand are also not parabolic, but rather Gaussian, as mentioned before. Including an appropriate pulse stretcher the clipping effect due to the limited stretcher bandwidth can produce flat-top or nearly parabolic spectra, that generate nonlinear phases which are well manageable as well.

3.4 Modeling the Propagation of Ultrashort Pulses by the Split-Step Fourier Method

In order to assess the possible working regimes and the obtainable pulse parameters of mode-locked fiber lasers, a thorough theoretical understanding of the intracavity pulse dynamics becomes mandatory. In the early years of mode-locked lasers, the Haus master equation [Hau75a; Hau75b; Hau00] has become successful in predicting classical soliton solutions and partially also for dispersion managed solitons. For the other pulse shaping regimes presented in the last section, the assumption, that the pulse experiences only small modifications per round trip, becomes increasingly inaccurate. Besides, the positioning of the cavity elements clearly has a great influence on the pulse shaping especially in the case of fiber lasers, which dooms all cavity-averaged models. This implies that an overall optimisation of a mode-locked fiber laser based on strict guide-lines is hardly attainable and at most local optima with regard to the desired properties can be readily obtained. In this pursuit, numerical models allow for a fast exploration of parameter spaces and subsequent optimisation without the need for time and cost consuming trial and error ventures.

The pulse dynamics in a mode-locked fiber laser are governed by Equation (3.3.1), i.e. a nonlinear partial differential equation. Solving this equation is widely done by the split-step Fourier method (SSFM) which was also implemented in the course of

this work in a Matlab script. The method is based on the alternating application of fiber nonlinearity in the time domain and fiber dispersion in the frequency domain.

Rewriting the pulse propagation equation in terms of the dispersion differential operator $\hat{D}$ and the nonlinear operator $\hat{N}$ yields [Agr07]

$$\frac{\partial A(z,t)}{\partial z} = \Bigg[\underbrace{-\frac{\alpha(z)}{2} - \frac{i\beta_2(z)}{2}\frac{\partial^2}{\partial t^2}}_{=:\hat{D}} + \underbrace{i\gamma(z)|A(z,t)|^2}_{=:\hat{N}}\Bigg] A(z,t) = (\hat{D}+\hat{N})A(z,t). \tag{3.4.1}$$

The idea behind the split-step method is to decouple the effects of dispersion and of nonlinearity and let each of them act on the pulse independently in a domain that avoids error-prone numerical derivatives. In practice, the propagation of the pulse envelope $A(z,t)$ over a small distance Δz is calculated in two steps: First, it is assumed that only the nonlinear effects act on the pulse, i.e. $\hat{D} = 0$:

$$A'(z+\Delta z, t) = \exp\Big[i\gamma(z)|A(z,t)|^2\Delta z\Big]A(z,t). \tag{3.4.2}$$

In the second step only dispersion, gain, and loss act on the pulse, i.e. $\hat{N} = 0$. This step has an analytical solution only in the frequency domain, thus the envelope is Fourier transformed with respect to time first $[A'(t) \to \tilde{A}'(\bar{\omega})$, where $\bar{\omega} := \omega - \omega_0]$. The dispersive step is then calculated by:

$$\tilde{A}(z+\Delta z, \bar{\omega}) = \exp\left\{\left[-\frac{\alpha(z)}{2} + i\frac{\beta_2(z)}{2}\bar{\omega}^2\right]\Delta z\right\}\tilde{A}'(z+\Delta z, \bar{\omega}). \tag{3.4.3}$$

Transforming back into time domain one obtains the pulse $A(z+\Delta z, t)$ propagated by distance Δz, i.e. altogether the propagation step is calculated by:

$$A(z+\Delta z, t) = \mathcal{F}^{-1}\Big\{\exp(\tilde{\hat{D}}\Delta z)\mathcal{F}\left[\exp(\hat{N}\Delta z)A(z,t)\right]\Big\}. \tag{3.4.4}$$

Here, $\mathcal{F}(\cdot)$ and $\mathcal{F}^{-1}(\cdot)$ denote the Fourier transform and its inverse, respectively. Incorporating the gain/loss α in the frequency step additionally allows for a frequency dependence therein, which can be used to model bandwidth limiting effects of different shapes, such as gain media with finite bandwidth and fiber Bragg gratings. The simulation of the complete oscillator is initiated by a random "pulse envelope" which is

repeatedly propagated through all fiber components of the resonator until a converged pulse solution is obtained.

3.4.1 Modeling of NALMs Incorporating 3x3-Couplers

In the context of this work, mode-locked fiber lasers containing a NALM as mode-locking element are of particular interest. The above described numerical procedure can be easily implemented to accurately model the effect of the NALM on the pulses. In contrast to the simulation of other saturable absorbers, whose transmission functions are often modelled in terms of intangible parameters, the impact of the NALM can be calculated a priori using only the fiber and coupler parameters. For example, the procedure for the pulse propagation through a 3x3-coupler-NALM as shown in Fig. 3.4 (a) can be done as follows: First, the incident field $A_{\mathrm{in}}(t)$ on port 1 is split into three fields

$$A_{\mathrm{P4}} = \frac{1}{\sqrt{3}} A_{\mathrm{in}},\ A_{\mathrm{P5}} = \frac{e^{-i\frac{2\pi}{3}}}{\sqrt{3}} A_{\mathrm{in}},\ \text{and}\ A_{\mathrm{P6}} = \frac{e^{-i\frac{2\pi}{3}}}{\sqrt{3}} A_{\mathrm{in}}. \tag{3.4.5}$$

The field A_{P4} exits the oscillator on the unconnected port 4. Note that there is no relative phase difference between A_{P5} and A_{P6} for the discussed arrangement in which an ideal, even coupler is assumed[2]. A_{P5} and A_{P6} are propagated through the NALM in opposite directions [$A_{\mathrm{P5}} \rightarrow A_{\mathrm{cw}}$, (clockwise), $A_{\mathrm{P6}} \rightarrow A_{\mathrm{ccw}}$ (counter-clockwise)], whereby the different orders of the fibers are taken into account. The asymmetrical positioning of the gain fiber causes a nonlinear phase difference between the propagated fields. Back at the coupler, each of the two fields are again split into three fields going to port 1, 2, and 3, respectively. Again, only the coupled fields receive a phase change of $2\pi/3$. The fields are then summed up coherently, resulting

[2] In general, for the case of a real, lossy (and uneven) coupler, the values of the coupling ratios and coupling phases can only be specified within certain loss-dependent boundaries [Pie89; FCI96].

in the output fields of the NALM

$$A_{\mathrm{P1}} = \frac{e^{-i\frac{2\pi}{3}}}{\sqrt{3}} A_{\mathrm{ccw}} + \frac{e^{-i\frac{2\pi}{3}}}{\sqrt{3}} A_{\mathrm{cw}}, \tag{3.4.6}$$

$$A_{\mathrm{P2}} = \frac{1}{\sqrt{3}} A_{\mathrm{ccw}} + \frac{e^{-i\frac{2\pi}{3}}}{\sqrt{3}} A_{\mathrm{cw}}, \tag{3.4.7}$$

$$A_{\mathrm{P3}} = \frac{e^{-i\frac{2\pi}{3}}}{\sqrt{3}} A_{\mathrm{ccw}} + \frac{1}{\sqrt{3}} A_{\mathrm{cw}}. \tag{3.4.8}$$

In this example the signal port is port 3, i.e. the output pulse duration on port 3 shall be reduced compared to the input pulse on port 1. As the phase advancement due to SPM is of opposite sign compared to the applied phase bias due to the coupler (compare eqs. 3.4.2 and 3.4.8), the counter-clockwise propagating field A_{ccw} needs to acquire a larger nonlinear phase shift than the clockwise propagating field A_{cw} in order to achieve constructive interference for the pulse peak on port 3. The nonlinear phase shift difference $\Delta\phi_{\mathrm{NL}}$ between the two counter-propagating waves can be quantified via the difference in their B-integrals $\Delta\phi_{\mathrm{NL}} := B_{\mathrm{ccw}} - B_{\mathrm{cw}}$ which are step-wisely calculated by

$$B_{\mathrm{cw/ccw}}(z + \Delta z) = B_{\mathrm{cw/ccw}}(z) + \gamma_{\mathrm{cw/ccw}} \max\left[|A_{\mathrm{cw/ccw}}(z + \Delta z, t)|^2\right] \Delta z. \tag{3.4.9}$$

3.5 Nonlinear Chirped Pulse Amplification

The aforementioned scheme of self-similar pulse propagation (see Section 3.3.3) is not only a viable route for the generation but also for the amplification of ultrashort optical pulses in fiber lasers. Once the pulses evolved towards the parabolic shape in the normally dispersive gain fiber, highly nonlinear propagation with B-integrals $>$ 50 rad can be obtained [Fu+17]. With this concept, pulse energies in the single-digit µJ regime with MW peak powers of the compressed pulses can be generated in Yb-doped fiber lasers [Lim+06; Liu+16]. A significantly further scaling of the pulse energy with this scheme is, however, prevented by an increasing power drainage from the pulse via Raman scattering [Fu+17]. Larger pulse energies and peak powers require the concept of chirped pulse amplification (CPA) [SM85]. Here, the impact of nonlinear effects is mitigated by a strong dispersive stretching of the low-energy pulses prior to the amplification, which effectively reduces the peak power and thus

the accumulated nonlinear phase during amplification. Once amplified, the pulses are recompressed, resulting in large peak powers. Ideally, this is achieved by an exact cancellation of all phase terms imprinted on the pulse by the stretcher, the compressor, and the fibers.

In practice, the stretched pulse duration in state of the art fiber CPA systems is limited to several nanoseconds which allows for the generation of single-digit mJ pulse energies [Eid+11]. In order to exploit a system's full potential in terms of pulse energy and peak power, a certain degree of nonlinearities should be admissible. Unfortunately, the accumulation of excessive nonlinear phase tends to reduce the peak power and degrade the pulse quality of the compressed CPA output. In this section the peculiarities of nonlinear fiber CPA systems are investigated with regard to the impact of the nonlinear phase on the output pulse quality and contrast.

3.5.1 A Simplified Model for Nonlinear CPA

Generally, the pulse propagation in a CPA system can be modeled by the SSFM as described in the previous section. However, due to the large chirp, a large temporal window T_{win} in the order of several nanoseconds is required for the simulations, instead of several picoseconds which is usually applied for the close-to-transform limited pulses. For a given number of computational grid points N, this implies that the temporal resolution $\Delta t = T_{\mathrm{win}}/N$ becomes larger, which results in inaccuracies regarding the unstretched pulse at the beginning and end of the system. This problem can be circumvented by increasing the number of computational grid points (e.g. from $N = 2^{12}$ to 2^{20}) which drastically reduces the speed of the simulations. Alternatively, the use of an analytical approach, which employs appropriate assumptions/idealisations, can give faster insights. Such models have been developed prior to this work [CKW07; Sch+09]. The corresponding assumptions comprise: (i) The pulse stretching is done predominantly by GDD, i.e. $\phi_2(\omega_0) \gg \phi_3(\omega_0)\Delta\omega/3$, where $\Delta\omega$ is the bandwidth of the pulse. (ii) The spectral shape of the input is unaffected by SPM or the gain spectrum during amplification. (iii) The spectral shape of the input is smooth. (iv) The absence of nonlinear effects apart from SPM. Assumption (i) implies that the chirp of the stretched pulse is nearly linear. By virtue thereof, the spectral shape of the input is mapped nearly linear on the temporal pulse shape and consequently

also on the acquired nonlinear phase

$$\phi_{\mathrm{NL}}(t) \propto |A(t)|^2 \propto |\tilde{A}(\omega)|^2. \tag{3.5.1}$$

Assumption (ii) can be justified by the large stretching phase. Even large nonlinear phases of 20 rad can be considered small compared to the quadratic stretching phase of >1000 rad. In the case of strong stretching, spectral broadening due to SPM is roughly proportional to the ratio of these phases and thus also small [CKW07]. As a further consequence of these assumptions, the nonlinear *spectral* phase at the output of the CPA system is well approximated by the magnitude of the acquired B-integral multiplied with the normalised spectral input shape [3]

$$\phi_{\mathrm{NL}}(\omega) \approx B \left(\frac{\tilde{A}(\omega)}{\max[\tilde{A}(\omega)]} \right)^2. \tag{3.5.2}$$

The assumed constant spectral shape and stretched pulse shape enable a much simpler treatment of the linear and nonlinear effects, as interdependencies thereof vanish. This allows for a straightforward summation of the various spectral phase terms of the stretcher, the compressor, and the linear and nonlinear propagation in the frequency domain without explicitly considering their succession. An inverse Fourier transformation then yields the pulse envelope after the compressor

$$A(t) \propto \mathcal{F}^{-1}\left\{ \underbrace{\tilde{A}(\bar{\omega})}_{\substack{\text{Spectral shape}\\ \text{of input pulse}}} \cdot \exp\left[i \left(\underbrace{\frac{\Delta\phi_2 \bar{\omega}^2}{2} + \frac{\Delta\phi_3 \bar{\omega}^3}{6}}_{\substack{\text{Residual dispersion due to}\\ \text{fiber, stretcher, and}\\ \text{compressor mismatch}}} \underbrace{+ B \left| \frac{\tilde{A}(\bar{\omega})}{\max[\tilde{A}(\bar{\omega})]} \right|^2}_{\text{Nonlinear phase}} \right) \right] \right\}. \tag{3.5.3}$$

Here, $\Delta\phi_2$ and $\Delta\phi_3$ correspond to GDD and TOD mismatch between stretcher, compressor, and fiber. In a linear CPA system, i.e. $B = 0$, the output pulse is best compressed by the choice of stretcher and compressor which zeros these dispersion phase terms. In a nonlinear CPA system, however, this approach would result in sub-optimal compression due to residual nonlinear phase. Depending on the spectral shape, the generated nonlinear phase can be partially compensated by an intentional mismatch of the dispersive phases ϕ_2 and ϕ_3. Compensation of higher-order phase terms is in principle also possible but requires more complex

[3] See [Sch+09] for a more rigorous mathematical derivation.

setups including for example spatial light modulators [Wei+92; Kar+01]. In the following Section, Equation (3.5.3) will be applied to examine the influence of the spectral shape on the compressed pulse.

3.5.2 Impact of the Spectral Shape on the Pulse Compressibility

In order to evaluate the pulse quality, the relative peak power (RPP) is usually considered, i.e. the ratio between the output peak power and the peak power of the corresponding transform limited pulse. This ratio is also often called temporal Strehl ratio. The RPP / Strehl ratio can be acquired from Equation (3.5.3) by

$$\mathrm{RPP} = \frac{\max\left[|A(t;\Delta\phi_2,\Delta\phi_3,B)|^2\right]}{\max\left[|A(t;0,0,0)|^2\right]}. \tag{3.5.4}$$

In Fig. 3.12 different initial spectral shapes are analysed in terms of their compressibility, i.e. maximum RPP, using the above model. The spectra are shown in Fig. 3.12 (a) and comprise a parabola, a Gaussian, a skewed Gaussian (skew factor $\alpha = 3$ [4]), a super-Gaussian of order 2 (i.e. a Gaussian with squared exponent), and a trimmed Gaussian, which is a Gaussian spectrum that is set to zero for frequencies beyond its FWHM [see green curve in Fig. 3.12 (a)]. The widths of all spectra are chosen to correspond to a 150 fs FWHM pulse duration. Fig. 3.12 (b) summarises the impact of the spectral shape on the maximum obtainable RPP for nonlinear propagation with B-integrals up to 30 rad. In this graph only GDD is adjusted (i.e. $\Delta\phi_2 \neq 0$ and $\Delta\phi_3 = 0$) to obtain the maximum RPP. As expected the parabolic spectrum allows for perfect compression even at high B-integral levels, since the generated nonlinear phase is purely quadratic. The trimmed Gaussian spectrum shows next to best performance in the model, which can be explained by the high congruence with the parabolic spectrum near the central part of the spectra. In theory, this enables an RPP >90 % even at a B-integral level of 20 rad. The super-Gaussian spectrum allows for RPPs of 80 % at a B-integral level of 10 rad. Gaussian and skewed Gaussian spectra perform worse and exhibit RPPs of <50 % for a B-integral of 10 rad. However, when additionally allowing for a compensation of SPM by TOD (i.e. $\Delta\phi_3 \neq 0$), the RPP of the Gaussian and the skewed Gaussian spectra can be improved from 45 to 55 % and from 35 to 63 %, respectively [see

[4] The skewed Gaussian is modeled by $\exp\left(-\bar{\omega}^2\sigma^2/2\right)[1+\mathrm{erf}(\alpha\bar{\omega}\sigma/\sqrt{2})]$.

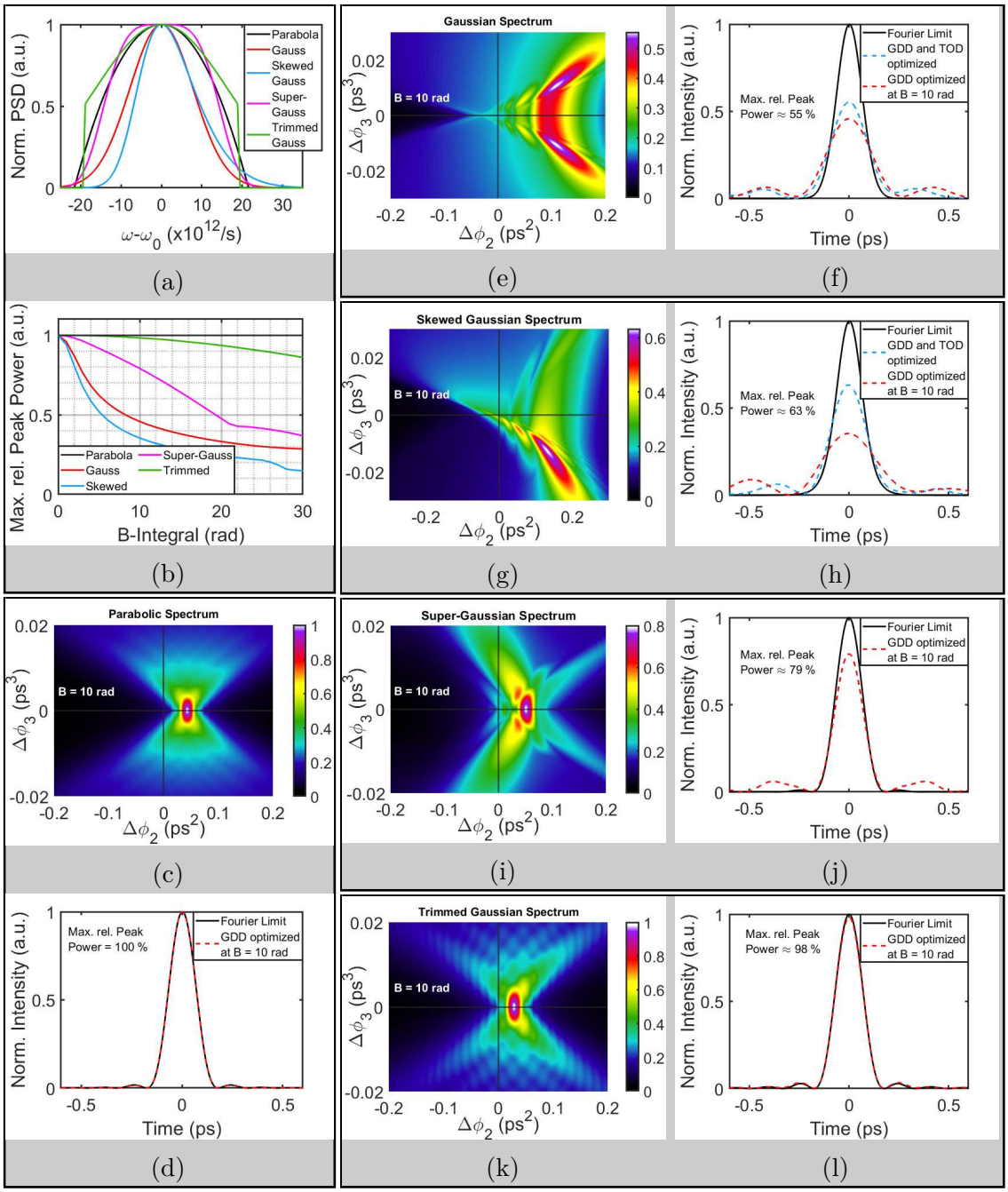

Figure 3.12: Analysis of the influence of the spectral shape on the pulse compressibility after chirped, nonlinear propagation using Equation (3.5.3). (a) Considered spectral shapes which each corresponds to a 150 fs FWHM pulse duration. (b) Maximum relative peak power for the different pulse shapes at different B-integrals with optimised GDD. (c),(e),(g),(i),(k) Relative peak power at a B-integral level of 10 rad in dependence of $\Delta\phi_2$ and $\Delta\phi_3$ for the parabolic, Gaussian, skewed Gaussian, super-Gaussian, and trimmed Gaussian seed spectra, respectively.(d),(f),(h),(j) Fourier limited (black), $\Delta\phi_2$-optimised (red dashed), and $\Delta\phi_2$-,$\Delta\phi_3$-optimised (blue dashed) pulses for the parabolic, Gaussian, skewed Gaussian, super-Gaussian, and trimmed Gaussian seed spectra, respectively.

Fig. 3.12 (e)-(h)], whereas for the other spectra the RPP decreases when $\Delta\phi_3 \neq 0$ [see Fig. 3.12 (c),(i),(k)]. The improvement of the RPP by TOD showcases two things: First, as the Gaussian shape is even (symmetric with respect to ω_0), its Taylor expansion excludes odd exponents. The fact that TOD can still improve the RPP shows that highest RPP is not necessarily obtained when the dispersion phase terms in Equation (3.5.3) cancel their corresponding nonlinear phase terms of same order, as long as other/higher-order phase terms are left uncompensated. A similar observation has already been made by [Zho+05]. From Fig. 3.12 (e) it can be seen that this can be achieved with positive and negative TOD alike. It should be noted that this kind of compensation generates asymmetric pulse profiles [see blue curve in Fig. 3.12 (f)]. Second, a skewed spectral shape can allow for a larger RPP compared to the unskewed spectral shape if TOD-compensation is admissible. For the skewed spectrum the nonlinear phase term also incorporates odd exponents in its expansion, which can be partially compensated by a deliberate TOD-offset between stretcher and compressor with the respective sign. Indeed, this technique has been used to generate compressed 500 fs pulses with 50 µJ pulse energy with a B-integral >10 rad [Sha+05].

In summary, the spectral shape of the seed pulses has a significant influence on the compressibility of the amplified pulses in a nonlinear CPA system. Close to parabolic spectra offer the highest RPP at large B-integrals, however, they also exhibit side pulses in the Fourier limited case [see Fig. 3.12 (d),(l)]. These side pulses are caused by the sharp edges in the spectra and might have adverse effects for certain applications of the laser system. In general, optimised RPP requires a mismatch of both GDD and TOD between fiber, stretcher, and compressor. Still, near-perfect compensation cannot be achieved for the vast majority of spectral shapes when the B-integral reaches a level of 10 rad and higher-order phase terms are left uncompensated. Clearly, the model's initial assumption of a constant spectral shape will be violated to some degree in a real-world CPA system, e.g. due to gain shaping, however, the analysis provides a good estimate on which kind of seed spectral shapes are preferable for nonlinear CPA.

3.5.3 Impact of Spectral and Phase Perturbations on the Pulse Contrast

Apart from the spectral shape discussed in the previous section, there are several other factors which have an impact on the nonlinear CPA. Real-world pulses are subject to perturbations during generation and amplification. For example, these perturbations include imperfect fiber components and splices, which lead to multiple reflections or back and forth coupling between the fiber axes with different group velocities. These effects lead to delayed pulse replicas, which are co-propagating and overlapping with the stretched main pulse due to a typical retardation of several to tens of picoseconds, depending on the fiber birefringence and the involved fiber lengths. Though originally weak (suppressed by 20-40 dB with respect to the main pulse), the pulse replicas can become strongly enhanced in the presence of nonlinearity and reach energies in the order of the main pulse.

Periodic Spectral and Phase Perturbations In the frequency domain, these pulse replica correspond to sinusoidal modulations of the spectrum. Again, these spectral features are transferred from the frequency domain to the pulse envelope in the time domain due to the large linear chirp. During nonlinear amplification the sinusoidal modulation of the pulse envelope causes a temporally modulated refractive index due to the Kerr effect. As is well known, a modulated refractive index causes an energy coupling between different modes. For example in diffraction gratings, a (lateral) spatial modulation of the refractive index causes a coupling between modes of different, discrete diffraction orders. Likewisely, the periodic *temporal* refractive index modulation can be regarded as a temporal phase grating, that couples energy between the main and pre-/post-pulses, which degrades the pulse contrast [Sch+08b]. Similarly, a slight modulation of the seed's spectral phase is transferred to the stretched pulse's amplitude and qualitatively leads to the same deterioration [DB08; Sch+08a]. Such phase modulations (or more generally ripples) are commonly imprinted by chirped fiber Bragg gratings used for pulse stretching [Mih+99]. The implications of both perturbations, an initial side pulse and an initial spectral phase modulation, are depicted in the first and second row of Fig. 3.13, respectively. In the SSFM simulation, the initial parabolic spectrum is chosen to correspond to a FWHM pulse duration of 150 fs. After the perturbation (side pulse

or spectral phase modulation, respectively)

$$A_{\text{SidePulse}}(t) := A(t) + \sqrt{R}A(t - \Delta t) \qquad \text{Side Pulse} \tag{3.5.5}$$

$$\tilde{A}_{\text{PhaseMod}}(\bar{\omega}) := \tilde{A}(\bar{\omega}) \exp\left[iq \cos\left(\bar{\omega}\Delta t'\right)\right] \qquad \text{Spectral Phase Modulation} \tag{3.5.6}$$

is applied, the pulses are dispersively stretched to 500 ps and amplified up to a B-integral of 10 rad. The initial side pulse intensity is suppressed by $R = 10^{-3}$ and delayed by $\Delta t = 5$ ps with respect to the main pulse [see red curves in Fig. 3.13 (a) and (b)]. The initial spectral phase modulation has a small amplitude of $q = 0.05$ rad and a spectral modulation frequency of $\Delta t' = 5$ ps [see red curves in Fig. 3.13 (d) and (e)]. Qualitatively, both types of perturbations lead to the same temporal as well as spectral features of the amplified pulses [see black curves in Fig. 3.13 (a), (b), (d), and (e)]. The reason for this is, that in both cases the stretched pulse is periodically modulated leading to the aforementioned Kerr-effect induced energy coupling to the side pulses. Due to the relative increase of the side pulse intensities the resulting spectra become strongly modulated. The choice of a parabolic input spectrum allows for a simple differentiation between a deterioration based on the modulations and effects arising from the spectral shape, as the nonlinear phase arising from the parabolic spectrum can be compensated with an appropriate GDD. In Fig. 3.13 (c) and (f) the pulse contrast degradation is numerically studied for a varying strength of the initial perturbations and the B-integral. Therefore the amplified pulses are compressed by applying the inverse of the stretcher phase and the nonlinear quadratic phase due to the propagation. From the plots, it can be seen that for an increasing B-integral the pulse contrast becomes increasingly susceptible to initial perturbations. For example, at a B-integral of 20 rad the relative energy in the main pulse decreases to below 70 % despite an initial pulse contrast of 30 dB. Thus, applications which demand a high pulse contrast require either low B-integrals and/or well controlled conditions of the seed signal.

Atmospheric Water Absorption The gain profile of Tm-doped fibers has a significant overlap with closely spaced, narrow-band (≈ 0.1 nm spectral width) absorption lines of water in the wavelength regime around 1900 nm. The broad-band spectra of ultrashort pulses originating from Tm-fiber lasers are thus affected when propagating in humid air. For example, the red curve in Fig. 3.13 (h) corresponds to the parabolic

spectrum of a 150 fs pulse centered at 1950 nm, which was subject to propagation through 1 m of humid air (relative humidity of 50 % at 20 °C, calculated using the spectroscopic data from [Rot+13]). The corresponding stretched pulse is shown in black in Fig. 3.13 (g). Despite a pulse stretching factor of >3000, the sharp spectral absorption features cannot be considered as linearly mapped onto the stretched pulse shape. Instead, the stretched pulse's intensity is rippled due to interference effects of different spectral components. These features are again imprinted on the nonlinear phase during amplification, ultimately causing the jagged output spectra as in Fig. 3.13 (h). As opposed to the periodic modulations discussed before, the irregular perturbations do not lead to discrete side pulses, but to a broad temporal background once the amplified pulses are compressed. Similarly however, energy and therefore also peak power is lost in the resulting pulse due to the initial perturbation by the molecular absorption [see Fig. 3.13 (i)].

When using a Treacy- or Martinez type setup for pulse stretching [Tre69; Mar87], the beam usually propagates through several meters of air, rendering high energy/ high contrast pulse generation challenging. Ultimately, the detrimental atmospheric effects must be circumvented by encasing the setup in a dry atmosphere, which enhances the system's complexity. For this reason, the use of a monolithic oscillator-stretcher-amplifier chain, as demonstrated in Chapter 5, becomes particularly attractive for Tm-based CPA-systems.

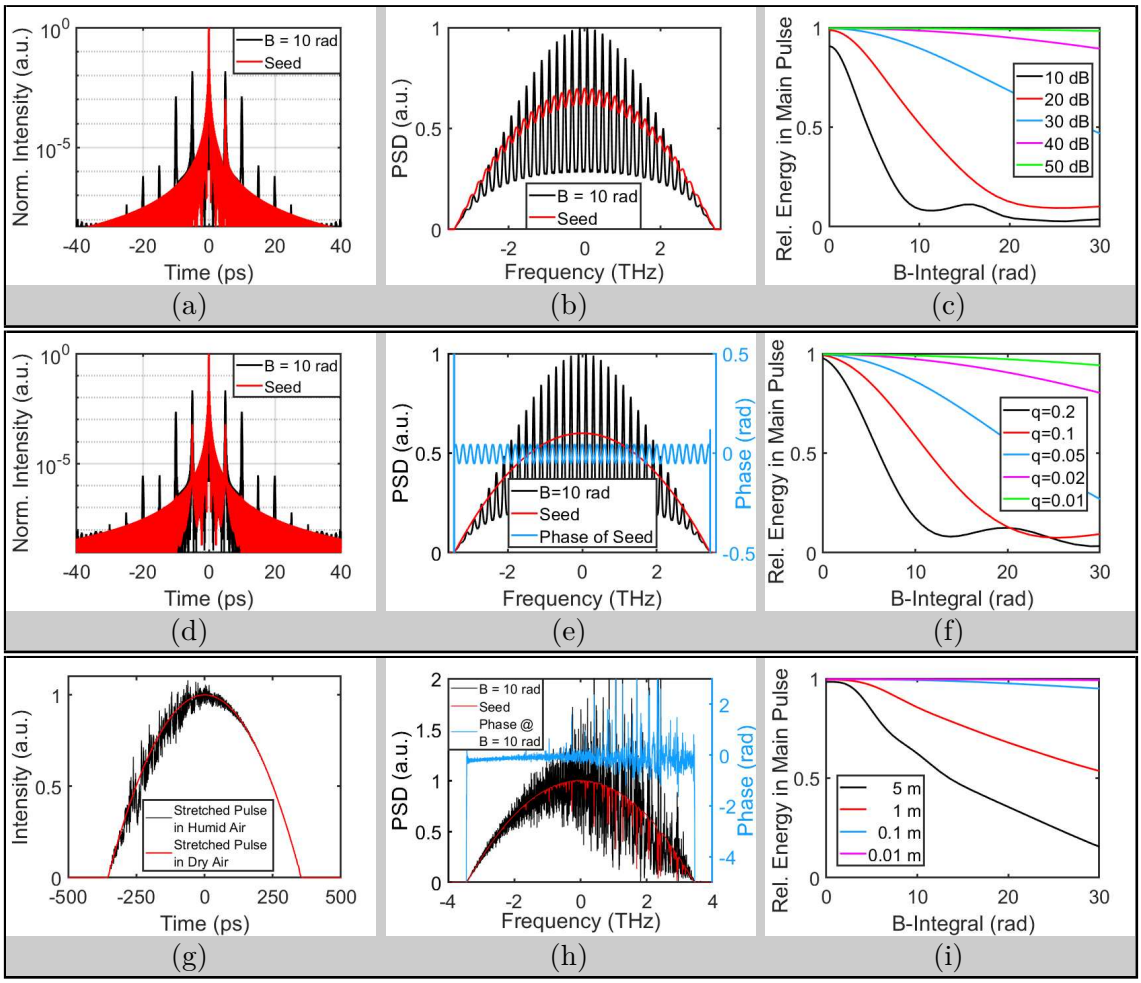

Figure 3.13: Numerical study of the influence of initial perturbations on the pulse contrast in a nonlinear CPA-system using the SSFM. (a) Initial intensity [red, t_P =150 fs pulse with a side pulse suppressed by 30 dB ($R = 10^{-3}$) at a delay of 5 ps] and transform limited output intensity (black) after CPA with a B-integral of 10 rad. (b) Corresponding initial (red) and amplified (black) spectrum. (c) Share of the pulse energy in the main pulse, i.e. in a time interval $\pm 3\,t_P$ from the pulse center, after compression of the amplified chirped pulses for different suppressions (10 to 50 dB) of the initial side pulse delayed by 5 ps. (d) Initial intensity (red, t_P =150 fs pulse with a sinusoidally modulated spectral phase of amplitude $q = 0.05$ rad / spectral modulation frequency $\Delta t' = 5$ ps) and transform limited output intensity (black) after chirped amplification with a B-integral of 10 rad. (e) Corresponding initial (red) and amplified (black) parabolic spectrum. (f) Share of the pulse energy in the main pulse after compression of the amplified chirped pulses for different modulation strengths (0.2 to 0.01 rad) at a spectral modulation frequency of $\Delta t' = 5$ ps. (g) Temporal profiles of a chirped t_P =150 fs pulse at central wavelength 1950 nm with (black) and without (red) the influence of propagation in 1 m of air at 20 °C and a relative humidity of 50 %. (h) Corresponding spectrum of the pulse after propagation in humid air, before (red) and after (black) amplification with a B-integral of 10 rad. The blue curve shows the remaining spectral phase after compression. (i) Share of the pulse energy in the main pulse after compression of the amplified chirped pulses for different propagation lengths (0.01 to 5 m) in humid air *before* the amplification.

CHAPTER 4

All-Fiber Lasers Passively Mode-Locked by a 3x3-Coupler-NALM

Tm-doped mode-locked fiber lasers generating sub-ps pulses in the 2 µm regime have received considerable attention in the past decade. So far, a multitude of mode-locking techniques has been demonstrated, without any of them being established as specifically advantageous compared to others yet. These range from intrinsic saturable absorbers such as SESAMs [Rud+12], graphene [Sot+17], carbon nanotubes [KW09], black phosphorus [Sot+15], topological insulators [LL18], or transition metal dichalcogenides [Lee+17] over artificial saturable absorbers based on NOLMs [Li+14], NALMs [Hän+18], and nonlinear polarisation rotation [Eng+08] up to hyrid versions thereof [Hax+11; Che+12; Che+14]. Recently, also the first Tm-doped Mamyshev oscillator has been demonstrated [Rep+19]. The plurality of examined saturable absorbers including many exotic materials may indicate that the approaches so far have not achieved satisfying maturity for robust generation of ultrashort pulses at 2 µm. In the following chapter, a different approach based on a 3x3-coupler-NALM is pursued experimentally and theoretically, which has enabled the first demonstration of the concept in Tm-based oscillators. The promising results obtained from these oscillators have also led to a transfer to Yb-based systems. Parts of these results have been published in [Gra+22].

4.1 Thulium Doped Fiber Laser

The experimental setup of the all-fiber, figure-8 Tm-oscillator is schematically shown in Fig. 4.1 (a). A polarisation maintaining (PM), single clad (SC) fiber with a MFD of 8 µm and a GVD of $\beta_2 = -0.085\,\mathrm{ps}^2/\mathrm{m}$ at 2 µm wavelength is employed as passive fiber. The active fiber is a 15 cm long PM, SC fiber which has a highly Tm doped ($\approx 7\%$) core and a MFD of 6.5 µm. The nominal core absorption at 1560 nm is 340 dB/m. Up to 2 W of pump light from a single-mode Er/Yb-codoped fiber amplifier with output wavelength 1565 nm can be injected into the NALM via a wavelength division multiplexer (WDM). During operation all active fibers are cooled passively by aluminium boards. The overall fiber length of the oscillator is 6.8 m, resulting in a repetition rate of 30.3 MHz and a total GDD of $-0.58\,\mathrm{ps}^2$ at 2000 nm. As no dispersion compensation is implemented, the oscillator operates in the soliton regime. A PM, fused 3x3-coupler, which is specified to be even for central wavelength 1950 nm, connects the NALM with the unidirectional part of the cavity. Herein, unidirectionality is established by an optical isolator, which additionally blocks the fast polarisation axis of the PM-fiber. The overall loss of the oscillator depends on the experienced difference of SPM between the counter-propagating fields in the NALM. In the low power limit, the overall loss is estimated to be 11 dB. For mode-locked operation, the loss is approximately 5 dB, as the energy is coupled to port 3 of the coupler more efficiently. The output of the oscillator can be monitored on port 2 as well as on port 4 of the 3x3-coupler.

The oscillator provides self-starting mode-locked operation at an initial pump power of 1.5 W. Mode-locking is initiated solely by the loss modulation of the NALM (see Section 3.2.1). At this pump power, multiple pulses oscillate in the cavity. When reducing the pump power to 790 mW only a single pulse is present in the cavity and can be preserved down to a pump power of 570 mW before mode-locked operation ceases. The output power in this regime ranges from 4 to 7 mW on port 2 and stays approximately constant at 3.9 mW on port 4 over a wide range of pump powers [see. Fig 4.1 (b)], corresponding to an output pulse energy of 130 pJ. This implies that the pulse energy incident on coupler port 1 is 390 pJ. During reduction of the pump power, the central frequency of the output spectra shifts from 2010 nm to 1994 nm [see Fig. 4.1 (c), (d)]. The spectral FWHM of the outcoupled pulses on port 4 is

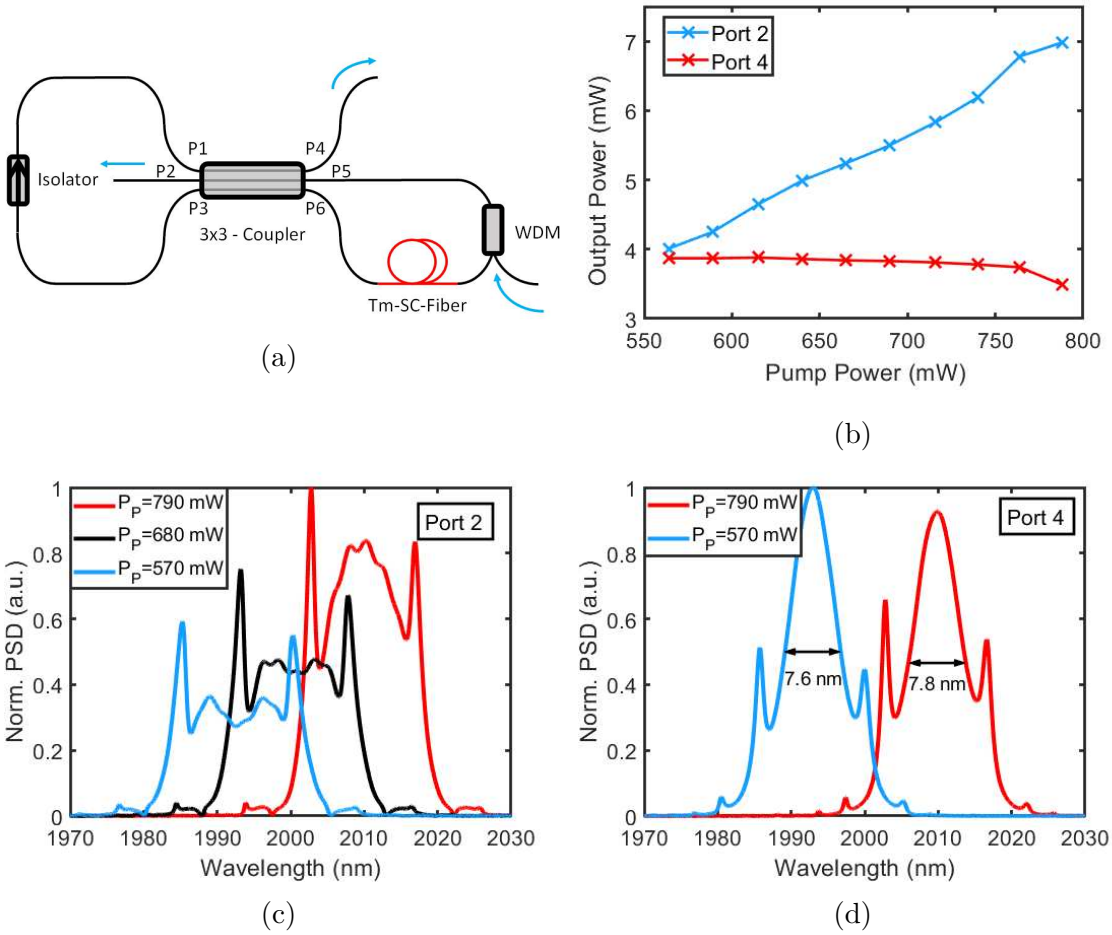

Figure 4.1: (a) Scheme of the all-fiber, figure-8 Tm-oscillator employing a 3x3-coupler. The outwardly facing blue arrows at port 2 and 4 specify signal outputs. The pump light enters the oscillator at the inwardly facing blue arrow and is reflected at the WDM towards the Tm-fiber. (b) Output power at port 2 and 4 for varying pump power in the single pulse regime. (c) Measured optical spectra on port 2 for different pump powers. (d) Measured optical spectra on port 4 for different pump powers.

7.7 ± 0.1 nm with a bandwidth limited pulse duration of approximately 540 fs. The bandwidth limited pulse duration on port 2, however, changes from 400 fs to 510 fs with increasing pump power. The Kelly sidebands in all output spectra indicate an operation in the soliton regime.

As the output wavelength deviates from 1950 nm, the coupler is not expected to act ideally symmetric with regard to the coupling ratio as well as the induced phase differences for the coupled fields. Indeed, good agreement with numerical simulations for the outcoupled spectra at port 2 could only be attained for coupler induced phase

shifts being increased from $\frac{2\pi}{3}$ by 18% (28%) for a central wavelength of 1994 nm (2010 nm) in the SSFM simulation. The pump power dependent shift of the central wavelength of the output spectra can thus be attributed to the wavelength dependent phase bias of the NALM, i.e. the larger nonlinear phase shifts generated due to a larger pump power render the NALM more efficient at longer wavelengths, as it is biased more strongly for longer wavelengths. Figure 4.1 (c) shows the obtained output spectra on port 2. Generally, port 2 enables insight on the spectral components that are rejected by the NALM and can thus provide information on the induced SPM-difference in the NALM in relation to the phase shift bias of the coupler. For example, the Kelly sidebands on port 2 are more strongly pronounced compared to the ones on port 4 [compare Fig. 4.1 (c) and (d)], as the dispersive waves experience negligible SPM in the NALM and are consequently interfered out of the oscillator to a greater extent. Moreover, for lower pump powers, the spectrum on port 2 shows a dip [see blue curve in Fig. 4.1 (c)] at the central wavelength, which is in agreement with the model introduced in Section 3.2.1 for the case of an unchirped pulse [see Fig. 3.5 (d)]. For larger pump powers, the dip turns into a peak at the central wavelength, indicating an over-driving of the NALM, with energy being coupled to port 3 less efficiently. This explanation is backed up by the fact, that the output power on port 2 grows with increasing pump power, whereas the output power on port 4 stays constant over a wide range and even slightly decreases [see Fig. 4.1 (b)]. Most efficient operation of the NALM is thus achieved at the low pump power threshold of mode-locking.

Numerical Analysis The numerical scheme outlined in Section 3.4 has been adapted to provide a complete oscillator simulation. The initial field distribution is randomly generated at a power level seven orders of magnitude below the converged pulse energy. Convergence to the same result is reliably attained within $\approx$ 100 round trip iterations. Fig. 4.2 (a) shows the simulated spectral evolution along the cavity for the counter-clockwise propagating pulse in the NALM as the steady state is reached for the case of 570 mW pump power. As mentioned before, the coupler induced phase shift in the model is changed to a value $1.18 \cdot 2\pi/3 \approx 2.47$ rad in order to obtain good agreement with the measured spectra [see Fig. 4.2 (b), (c)]. This adjustment can be justified by the fact, that the 3x3-coupler is not operating

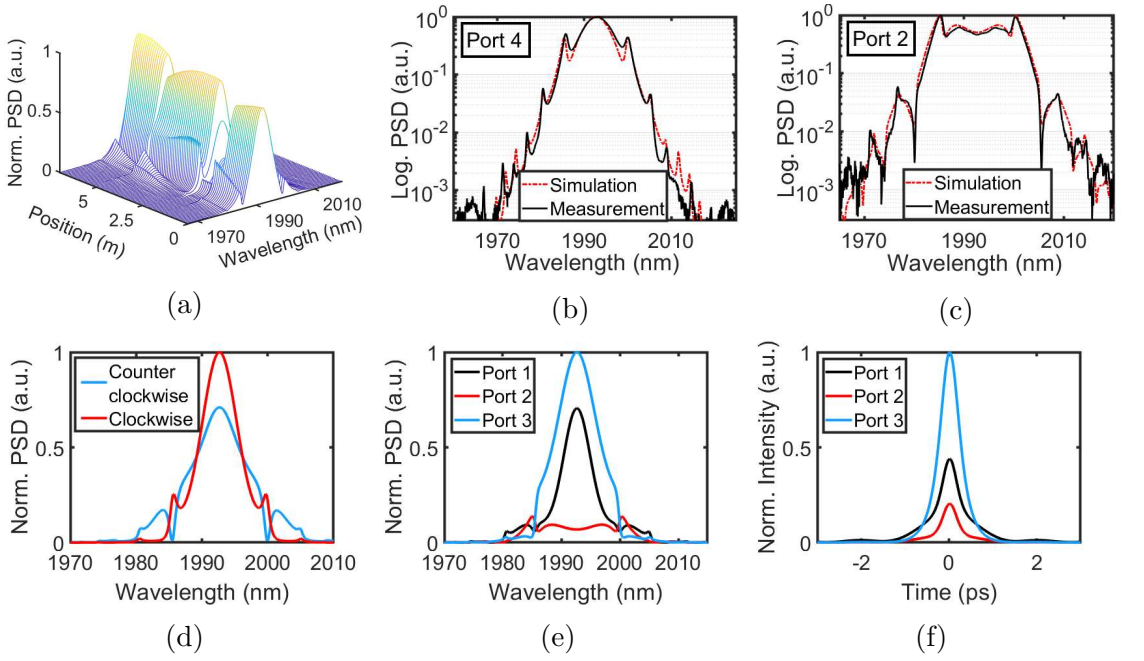

Figure 4.2: Numerical simulation of the complete oscillator mode-locked by NALM. (a) Evolution of the spectral intensity inside the cavity. The origin $z = 0$ is chosen to be at the position of the isolator in the unidirectional ring. The shown spectra are the ones of pulses propagating counter clockwise in the NALM. The pulses enter the NALM at $z = 1.5\,\mathrm{m}$ and are recombined by the 3x3-coupler at $z = 5.3\,\mathrm{m}$. (b) Comparison of simulation and measurement for the spectra obtained at port 4. (c) Comparison of simulation and measurement for the spectra obtained at port 2. (d) Simulated spectra of the clockwise and counter clockwise propagating pulses immediately before the combination at the coupler. (e) Simulated spectra obtained at the ports 1, 2, and 3 immediately after the combination at the coupler. (f) Simulated pulses obtained at the ports 1, 2, and 3 immediately after the combination at the coupler.

at its specified wavelength of 1950 nm. The simulation grants insight on otherwise hidden behaviour that is inaccessible by the experiment. For example, the counter clockwise propagating pulse experiences substantially larger SPM than the clockwise propagating pulse (calculated difference of the B-integrals between the counter-propagating pulses: $\Delta\phi_{\mathrm{NL}} = 3.88\,\mathrm{rad} - 1.33\,\mathrm{rad} = 2.55\,\mathrm{rad}$). Consequently, the two corresponding spectra of the pulses that interfere at the coupler differ profoundly [see Fig. 4.2 (d)]. The dips at the spectral position of the first order Kelly sidebands of the counter clockwise propagating pulse indicate destructive interference of the soliton with the respective dispersive waves due to the extensive nonlinear phase

shift ($\phi_{\mathrm{NL,\ ccw}} > \pi$), whereas additional frequency components are generated further away from the central frequency. When the counter-propagating pulses interfere at the coupler, the output spectrum on port 3 is thus slightly broadened ($\Delta\lambda = 8.5\,\mathrm{nm}$). Moreover, it is nearly free of spectral sidebands while the spectra on port 1 and 2 show alternating peaks and dips at the different sideband orders, i.e. port 1 shows a dip at $m = 1$ and a peak at $m = 2$ and port 2 vice versa [see Fig.4.2 (c),(e)]. Apart from the sidebands, the retrieved spectra qualitatively resemble the expected spectra from the model for an unchirped input pulse [see Fig.3.5 (d)]. The respective temporal profiles in Fig. 4.2 (f) show a clean, nearly sech^2-shaped pulse on port 3 and strong tails on ports 1 and 2, revealing the pulse shortening/cleaning effect due to the NALM. According to the simulation 56% of the total power is coupled to port 3, which is close to the maximum of 60% expected from the model in Section 3.2.1.

By virtue of the soliton area theorem [Equation (3.3.3)] a comparatively large pulse energy of

$$E_{\mathrm{p}} = \frac{2|\beta_2|}{\gamma t_0} = \frac{2 \cdot 0.085\,\mathrm{ps}^2/\mathrm{m}}{0.0013\,\mathrm{m}^2/\mathrm{W} \cdot 540\,\mathrm{fs}/1.76} \approx 430\,\mathrm{pJ} \tag{4.1.1}$$

is expected due to a large value of average dispersion and a low nonlinear parameter at 2 µm wavelength. The numerically retrieved cavity average pulse energy over one round trip (for both clockwise and counter-clockwise propagating pulses) is 440 pJ and is thereby in good agreement with the soliton area theorem.

4.1.1 Dispersion Adjustment via cFBG

The achievable minimum pulse duration in the soliton regime is to a great extent limited by the large chromatic dispersion of the fused silica fibers at 2 µm. In order to attain shorter pulse durations, a chirped fiber Bragg grating (cFBG) is included in the resonator [see Fig. 4.3 (a)]. Unidirectional propagation from port 3 to port 1 is ensured by an optical circulator. The normal dispersion introduced by the grating is $\phi_{2,\mathrm{cFBG}} = 0.53\,\mathrm{ps}^2$. The overall fiber length of the resonator is 7.9 m, resulting in a repetition rate of 26.1 MHz and an overall GDD of $-0.07\,\mathrm{ps}^2$ at 1950 nm. The grating has a peak reflectivity of 20% centered at 1950 nm with a FWHM of 40 nm. Employing the cFBG for dispersion compensation addresses two major issues: Firstly, the grating fixes the operating wavelength of the oscillator and reduces the shift of

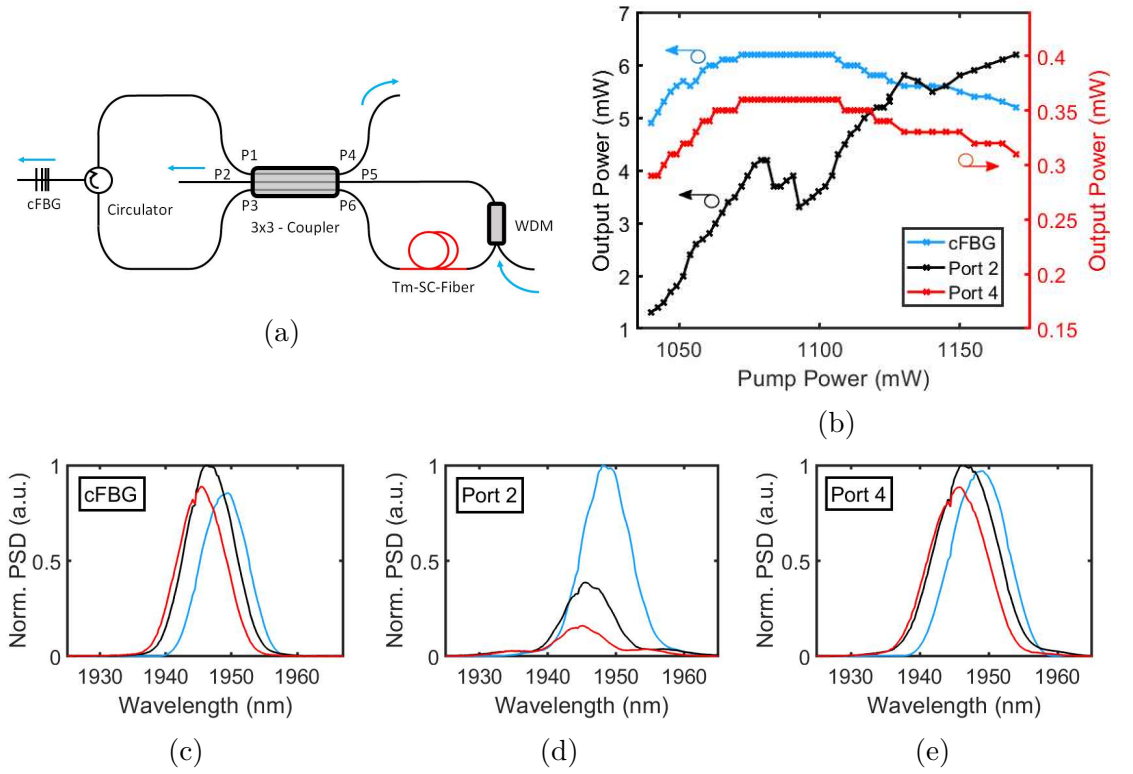

Figure 4.3: (a) Scheme of the Tm-oscillator employing the cFBG. Outwardly facing blue arrows correspond to signal outputs. The inwardly facing blue arrow corresponds to the pump light input. (b) Output power at the three different exits for a single pulse in the cavity. (c)+(d)+(e) Output spectra at the three different exits for pump powers slightly above the single pulse mode-locking threshold (1040 mW, red), in the middle of the single pulse regime (1090 mW, black) and at the upper limit of the single pulse regime (1170 mW, blue).

the spectrum's central wavelength when tuning the pump power. Secondly, it allows for the transition from the soliton to the DMS regime which enables reduced pulse durations and also a reduced coupling of energy to dispersive waves (see Section 3.3.2). On the other hand, the grating and the required optical circulator add ≈ 8 dB of loss to the cavity.

Despite the large losses, the oscillator provides self-starting operation at a pump power of 1.8 W. Single pulse operation is obtained for pump powers between 1040 mW and 1170 mW. As expected, the output power at the cFBG and port 4 follow the same trend when the pump power is varied [see Fig.4.4 (b)]. Both of them show a plateau between $P_{\mathrm{Pump}} = 1070$ and 1110 mW and decreasing output power for larger pump powers. Meanwhile, the output power at port 2 shows a dip in this pump

power regime and increases for larger pump powers. This behaviour indicates that the NALM operates most efficiently, i.e. with largest relative transmission to port 3, for a pump power of 1070 mW, as a further increase in pump power results in less signal power being coupled to port 3.

The absence of spectral sidebands indicates that the oscillator does not operate in the classical soliton regime anymore [see Fig. 4.3 (c),(d), and (e)]. Also, the spectral width at all three output ports is slightly increased compared to the soliton operation with a maximum spectral FWHM of 10.3 nm at port 4. Reassessing the numerical simulation of the oscillator, it is revealed that even wider spectra of FWHM 25 nm with corresponding shorter pulse durations of approximately 300 fs should be obtainable at different output positions of the oscillator [see Fig.4.4 (b) and (c)]. In order to exploit this behaviour, an additional 5%-tap-coupler is added inside the NALM, which allows a partial extraction of the counter clockwise propagating pulse immediately before the 3x3-coupler. In this configuration, the oscillator does not exhibit self-starting operation anymore, but can be started by a mechanical trigger, i.e. twitching at the fibers, at a pump power of ≈ 1.8 W. Apart from that, the output characteristics are similar as before. The additional output at the tap coupler provides a significantly broader, M-shaped spectrum [see Fig. 4.4 (d)] with a FWHM between 19.7 and 22.9 nm and a dip at the central wavelength that is more pronounced with increasing pump power. This spectral shape is characteristic for up-chirped pulses that experience SPM during propagating: Starting from the cFBG, the introduced up-chirp is gradually decreased due to the anomalous chromatic dispersion of the fiber [see Fig. 4.4 (c)]. Once the pulse duration approaches 1 ps, the increased peak power leads to an enhanced influence of SPM. The spectral width therefore broadens until the pulse is close to its transform limit and then decreases again due to the spectrally narrowing effect of SPM on the down-chirped pulse. Afterwards, the sign of the chirp is again flipped by the cFBG.

Pulse Duration Measurement In order to measure the compressed duration of the outcoupled pulses, a commercial SHG autocorrelator (APE pulseCheck) is used. As the output of the oscillator at the 5%-tap-coupler is below the detection threshold of the autocorrelator ($P_{\text{out}} \approx 250\,\mu$W), the pulse train needs to be amplified first. Therefore, an all-fiber CPA configuration is chosen, i.e. the pulses are temporally

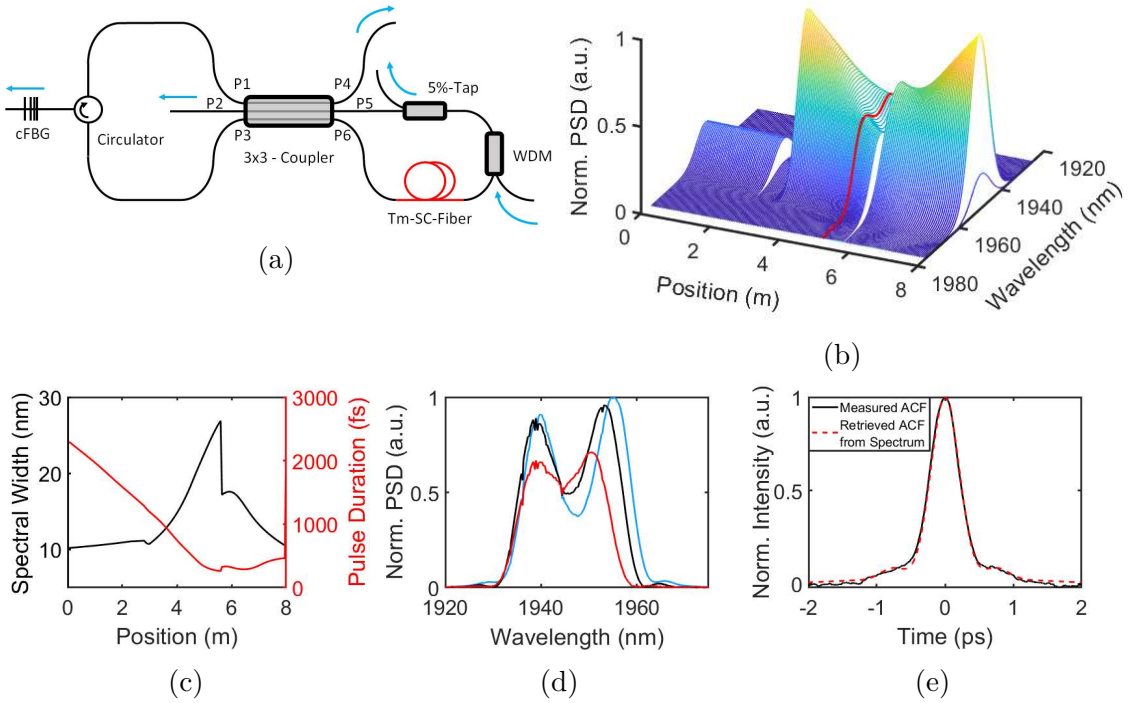

Figure 4.4: (a) Scheme of the Tm-oscillator employing the additional tap coupler in the NALM. (b) Calculated evolution of the spectral intensity inside the cavity. The origin $z = 0$ is chosen to be at the position of the cFBG. The shown spectra correspond to the counter clockwise propagating pulses in the NALM. The pulses enter the NALM at $z = 2.3\,\mathrm{m}$ and are recombined by the 3x3-coupler at $z = 5.6\,\mathrm{m}$. The red line indicates the position of the tap coupler in the NALM. (c) Calculated evolution of the spectral width and the pulse duration in the course of one round trip. (d) Measured spectra at the tap coupler for pump power powers slightly above the single pulse mode-locking threshold (red), in the middle of the single pulse regime (black) and at the upper limit of the single pulse regime (blue). (e) Measured and retrieved autocorrelation traces (ACT) corresponding to the black spectrum in (d).

stretched in a 3 m long, normally dispersive fiber with $\beta_2 = 0.095\,\mathrm{ps}^2/\mathrm{m}$ and amplified in a 2 m long Tm-doped double clad fiber co-pumped by a multi-mode fiber coupled laser diode with maximum power of 4 W at wavelength 793 nm. Afterwards, the pulses are compressed again using anomalously dispersive fiber. This order of fibers offers the advantage of propagation with lower pulse peak powers in the normally dispersive fiber, which exhibits a nonlinear parameter that exceeds the one of the anomalous dispersive fiber approximately by a factor of three. Consequently, the

influence of SPM on the spectrum and nonlinear compression can be mitigated. The resulting autocorrelation trace (ACT) of the 5%-tap-coupler output together with the reconstructed ACT from the measured spectrum is shown in Fig. 4.4 (e). Assuming the same pulse shape for measured and reconstructed pulses, a pulse duration of 325 fs can be estimated. The corresponding Fourier limited pulse duration is 315 fs. The measured pulse profile shows a slight pedestal and overall fits well with the expected ACT retrieved from the Fourier transform of the spectrum. Remaining SPM acquired during propagation and/or higher-order dispersion mismatch of the used fibers thus only show a minor influence.

4.1.2 Distributed Dispersion Compensation via cFBG and NDF

The spectral shape and the relatively small bandwidth obtained by the dispersion adjusted oscillator are still not ideal as a seed for nonlinear CPA. However, simply reducing the fiber length in order to decrease the magnitude of the overall oscillator dispersion results in self-starting issues and does not significantly increase the obtainable spectral width. Therefore, in a next step, parts of the passive fiber in the NALM are replaced by 2 m of a polarisation maintaining, normally dispersive fiber (NDF). The fiber possesses a GVD of $\beta_2 = 0.025\,\mathrm{ps}^2/\mathrm{m}$ at 1950 nm with a small core diameter of 3 µm. The overall GDD is slightly normal with a value of $0.05\,\mathrm{ps}^2$. Besides, the small core and the correspondingly large nonlinear parameter γ of the NDF in the NALM can facilitate the pulse build-up due to additional SPM. Moreover, a second 15 cm long Tm-doped single clad fiber is added before the cFBG [see Fig. 4.5 (a)]. It is pumped via a second WDM by up to 2 W of single mode power at 1565 nm. The second amplifier substantially lowers the pump power required for self-starting. The mode-locked operation starts at a pump power level of 700 mW for both amplifiers and again in multi-pulse operation. Single pulse operation can then be obtained by reducing the pump powers in both amplifiers and is maintained over a wide range of pump powers [see Fig. 4.5 (b)].

Overall, the distribution of the normal dispersion to two different positions results in a broader spectrum throughout the resonator [see Fig. 4.5 (c)]. Again, the extracted spectra at port 2 show distinct features that depend strongly on the applied pump power. These features can be used to determine the state of the NALM when the output spectra are matched to the SSFM model, i.e. the nonlinear phase

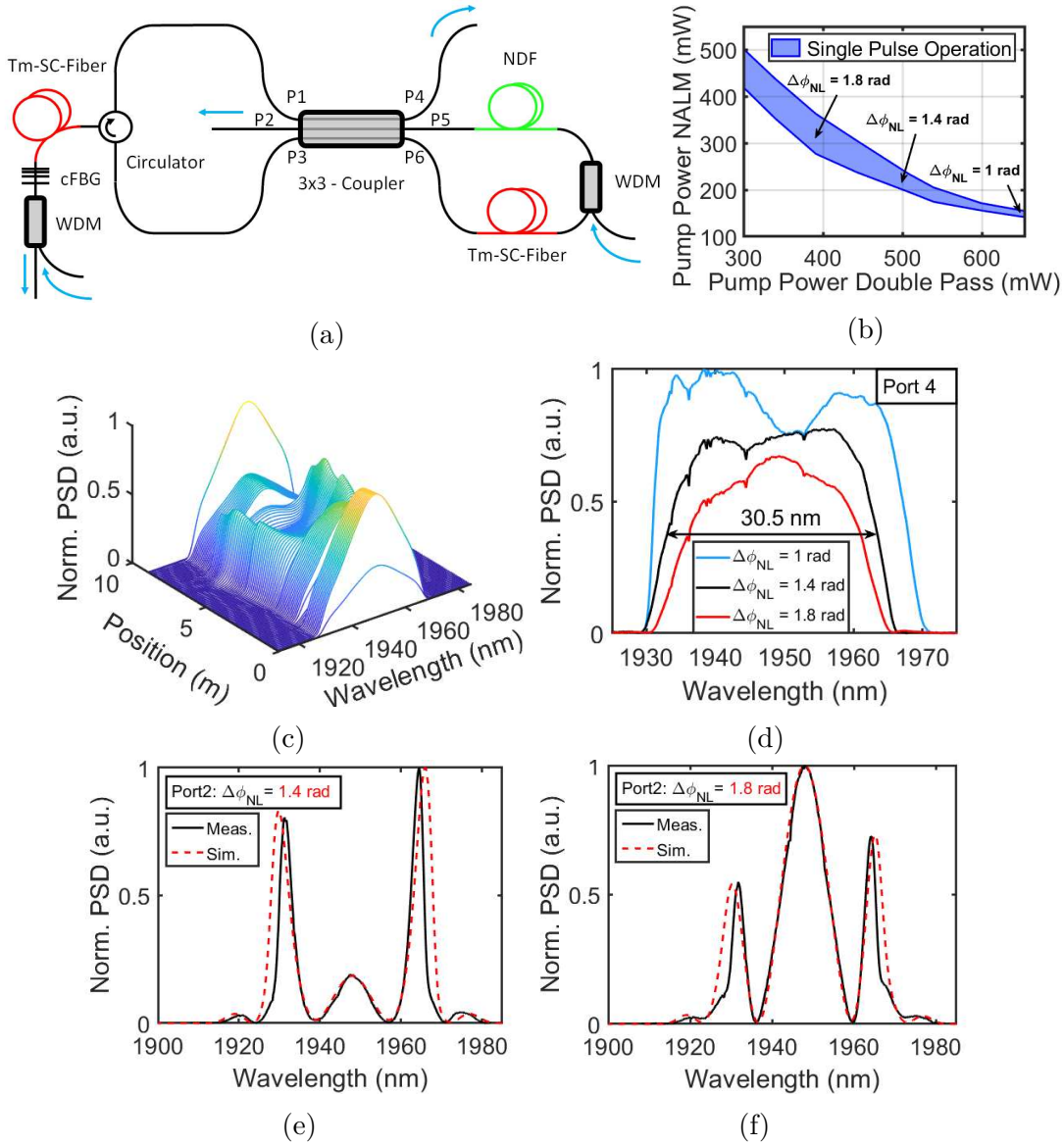

Figure 4.5: (a) Scheme of the Tm-oscillator employing the cFBG and additional NDF in the NALM for distributed dispersion compensation. (b) Pump power regime in which single pulse operation is maintained together with corresponding numerically retrieved values of the nonlinear phase difference in the NALM. (c) Calculated evolution of the spectral intensity inside the cavity. The origin $z = 0$ is chosen to be at the position of the cFBG. The shown spectra correspond to the counter clockwise propagating pulses in the NALM. (d) Measured output spectra at port 4 for different nonlinear phase differences as indicated in (b). (e)+(f) Measured and simulated output spectra at port 2 for a nonlinear phase difference of 1.4 and 1.8 rad, respectively.

difference between the counter-propagating pulses can be estimated [see for example Fig. 4.5 (e),(f)]. Generally, it can be stated that $\Delta\phi_{\mathrm{NL}}$ increases, when the pump power of the amplifier in the NALM is increased and the pump power of the second amplifier is reduced and vice versa [see Fig. 4.5 (b)]. The retrieved values of $\Delta\phi_{\mathrm{NL}}$ are between 1 and 2 rad and thereby much lower than in the previous implementations. This signifies that the usage of the second amplifier can largely expand the parameter space, as even less efficient NALM-states become accessible. For example, the oscillator can be operated at a relatively low NALM-efficiency [nonlinear phase difference of 1 rad with a low pump power of the NALM-amplifier (150 mW)] as long as the double-pass pump power is kept above 600 mW. In this state, the pulse reflected from the cFBG is amplified to a pulse energy of 1 nJ (extracted pulse energy at port 4: $E_{\mathrm{P}} = 320$ pJ) which leads to significant spectral broadening due to SPM in the fiber section between the double-pass amplifier and the 3x3-coupler. Together with the up-chirp induced by the cFBG the spectral FWHM is increased to 36 nm at port 4 [see Fig. 4.5 (d)]. The increased influence of SPM can also be seen in the onset of an M-shaped spectrum and the increasingly steep edges of the spectrum. With regard to the usage of the oscillator in a nonlinear CPA-system, this spectral shape can be detrimental to the achieved pulse quality, due to the mapping of the spectral shape on the temporal pulse shape and thus ultimately on the spectral phase. Indeed, when the formalism of Section 3.5.2 is applied to evaluate the pulse compressibility after a nonlinear CPA with B =10 rad, the spectrum of port 4 at $\Delta\phi_{\mathrm{NL}} = 1.0$ rad exhibits only a maximum RPP of 54 %. The spectrum at $\Delta\phi_{\mathrm{NL}} = 1.8$ rad, on the other hand, allows for a maximum RPP of 85 % (see Fig. 4.6), which renders it a more suitable seed for a nonlinear CPA system[1]. Moreover, in the state of $\Delta\phi_{\mathrm{NL}} = 1.0$ rad, small changes in the pump power for the NALM-amplifier lead to the loss of single pulse operation [see Fig. 4.5 (b)]. A working point with a more parabolic, yet still broad spectral shape and larger stability range should therefore

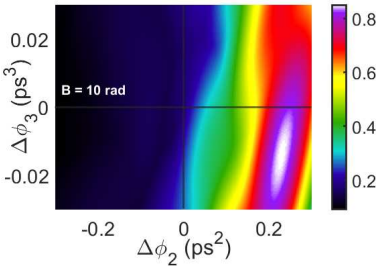

Figure 4.6: RPP when using the spectrum of port 4 at $\Delta\phi_{\mathrm{NL}} = 1.8$ rad as a seed for nonlinear CPA with B =10 rad according to the formalism in 3.5.2.

[1] However, it should be kept in mind that the pulse stretcher and gain narrowing in the subsequent amplifiers will additionally influence the spectral shape and thus the final pulse compressibility.

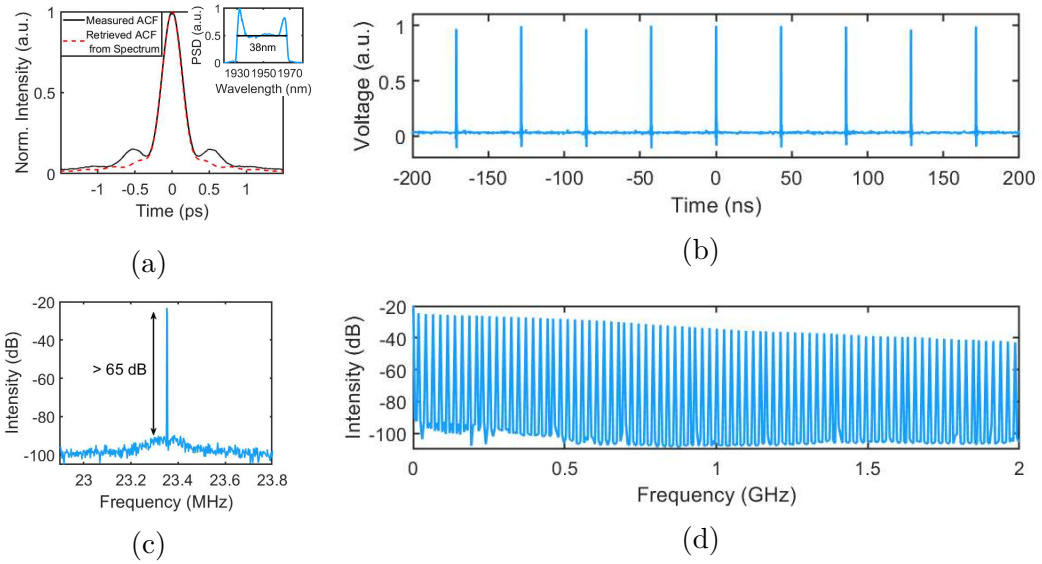

Figure 4.7: (a) Measured intensity autocorrelation trace at port 4 at $\Delta\Phi_{\mathrm{NL}} = 1.4\,\mathrm{rad}$. The FWHM of the ACT is 325 fs. The inset shows the corresponding measured spectrum of the compressed pulses. The FWHM of the ACT, that is retrieved from the spectrum, is 315 fs, which infers an estimated pulse duration of 215 fs for the measured pulse. (b) Measured oscilloscope trace of the pulse train at port 4. (c)+(d) RF-spectra of the pulse train from port 4.

be chosen. The working point with $\Delta\phi_{\mathrm{NL}} = 1.4\,\mathrm{rad}$ offers a trade-off between these traits [see Fig. 4.5 (d)]. The ACT of this working point is shown in Fig. 4.7 (a). The pulses are compressed simply by splicing additional passive fiber with anomalous dispersion to port 4. In the course of the compression, the 220 pJ pulses experience significant spectral broadening [from 30.5 nm to 38 nm FWHM, see inset of Fig. 4.7 (a)] resulting in a measured pulse duration of 215 fs. Comparing the ACT with the one that is retrieved from the spectrum, side lobes without spectral correspondence can be noticed. The origin of these side lobes is likely a higher-order dispersion mismatch of the fibers/cFBG and residual nonlinear spectral phase that stems from the compression in the fiber.

The oscilloscope trace measured at port 4 is shown in Fig. 4.7 (b). Figure 4.7 (c) and (d) show the corresponding RF-spectrum of the output pulse train. The absence of sidepeaks down to $> 65\,\mathrm{dB}$ and the monotonically decreasing harmonic peaks confirm the absence of Q-switching instabilities or multi-pulsing. Together with the autocorrelation measurement (scan range up to 150 ps) single pulse operation is verified.

4.2 Ytterbium Doped Fiber Laser

As the initial demonstration of the Tm-NALM-oscillator in the previous Chapter showed compelling results, transferring the architecture to Yb-doped fiber lasers seemed tempting. Therefore, a similar setup was realised for a central output wavelength of 1030 nm [see Fig. 4.8 (a)]. The Yb-SC-fibers are pumped by 976 nm diodes, each of which delivers up to 500 mW of pump power. In contrast to the 2 µm oscillator, a 4-port circulator is used which additionally allows for the observation

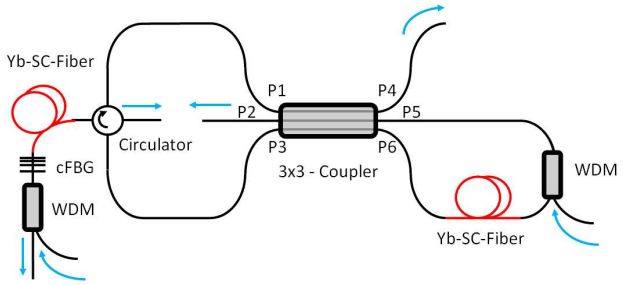

(a)

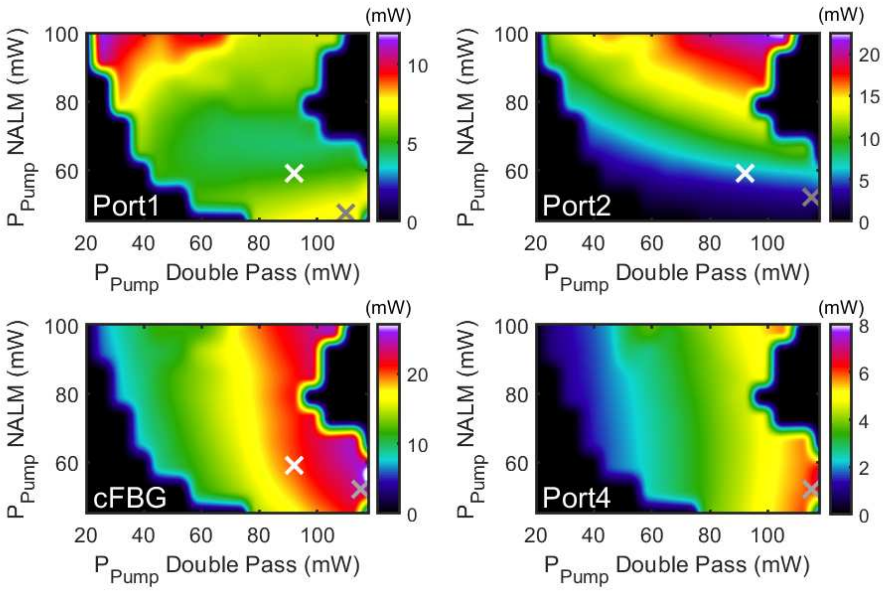

(b)

Figure 4.8: (a) Scheme of the Yb-oscillator employing a 3x3-coupler. (b) Interpolated maps of output powers at the four different output ports in dependence of the pump powers of the two amplifiers. The white crosses mark the state of the measured output spectra in Fig. 4.9 (a). The grey crosses mark the states of shortest measured pulse durations (see Fig. 4.11).

of the signal returning from port 1. Below ≈ 1270 nm wavelength, the dispersion of fused silica is normal, thus the dispersion compensation by a cFBG must be anomalous. Moreover, the magnitude of the fiber dispersion $\beta_2 = 0.02\,\mathrm{ps}^2/\mathrm{m}$ is smaller by a factor of four compared to the fiber in the 2 µm oscillator. The chosen magnitude of the GDD of the cFBG ($-0.21\,\mathrm{ps}^2$) is therefore also smaller compared to the 2 µm oscillator. The resulting overall GDD of the oscillator is again slightly positive ($0.01\,\mathrm{ps}^2$) at a repetition rate of 20.8 MHz.

4.2.1 Experimental Results

The starting behaviour is similar to the Tm-oscillator: mode-locking is initiated by increasing the pump power of both amplifiers to ≈ 200 mW whereby again multiple pulses oscillate in the cavity. Single pulse operation can then be obtained by reducing both pump powers to a level of <100 mW. Comprehensive maps of the obtained output powers during single pulse operation at all four outputs can be found in Fig. 4.8 (b). Expectedly, the output powers at the cFBG and port 4 vary largely with the double-pass pump power, whereas the output powers at port 1 and 2 show a stronger dependence on the pump power of the NALM amplifier. Interestingly, the output power at port 1 first decreases for increasing pump power in the NALM and then increases again. This can be explained by recalling the model introduced in Section 3.2.1. Therein, the relative transmission to port 1 shows a wide minimum at $\Delta\phi_{\mathrm{NL}} \approx 3.7\,\mathrm{rad}$[2]. The maximum pulse energy (1.2 nJ) can be obtained at the cFBG output.

The output spectra of the NALM on port 1 (via the optical circulator), port 2, and behind the cFBG (since port 3 cannot be accessed directly in this configuration) can be seen in Fig. 4.9 (a). The spectral shapes agree well with the model for the case of a chirped input pulse [see Fig. 3.5 (e)], as well as with the expected spectra from a full-cavity simulation [see Fig. 4.9 (b)]. The simulative replication further reveals that the nonlinear phase difference for the shown spectra is approximately 2.7 rad. Replicating the spectra near the upper and lower single pulse thresholds suggests that admissible values of $\Delta\phi_{\mathrm{NL}}$ range from approximately 1.8 to 3.4 rad.

Figure 4.10 (a) shows the evolution of the spectral as well as the temporal width

[2] It should be noted, that the position of the minimum shifts towards lower $\Delta\phi_{\mathrm{NL}}$ when gain is present in the NALM, which is not the case for the simplified model.

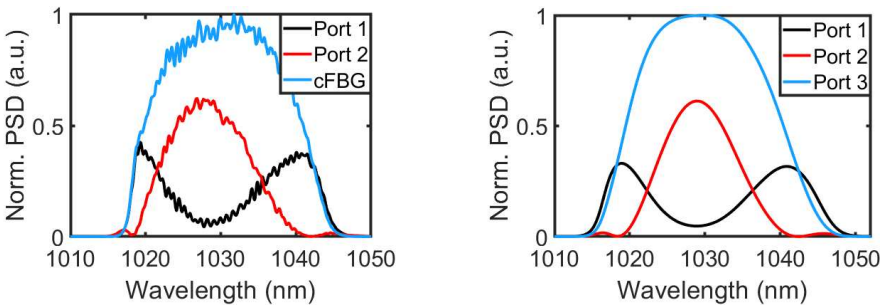

(a) (b)

Figure 4.9: (a) Measured output spectra at port 1, port 2, and the cFBG-output of the Yb-oscillator employing the 3x3-coupler. (b) Simulated output spectra at port 1, port 2, and port 3.

of the pulse in the course of one round trip. From the monotonic increase of the pulse duration during propagation which is reset by the cFBG it can be inferred that the pulse is permanently up-chirped. Thus the oscillator is not operating in the dispersion-managed regime. The parabolic output spectrum [see Fig. 4.10 (b)] together with the pronounced chirp at the cFBG output (measured uncompressed pulse duration 9.2 ps), indicate a parabolic temporal pulse profile with the oscillator operating in a self-similar regime. This conjecture is validated by continuously calculating the misfit parameter [Fin+06]

$$\chi(z) = \frac{\int \left[|A(t,z)|^2 - p(t,z)\right]^2 dt}{\int |A(t,z)|^4 dt}, \tag{4.2.1}$$

which quantifies the congruence of the pulse with a parabolic pulse fit $p(t,z)$. After the cFBG, whose effect on the pulse amplitude is modeled by a Gaussian filter, the pulse quickly evolves towards a parabolic shape [see Fig. 4.10 (c)].

Peculiarly, the evolution towards the parabolic pulse shape mostly takes place in the passive fiber which distinguishes it from the self-similar evolution in the gain fiber discussed in Section (3.3.3). Both gain fibers are rather short (35 cm and 40 cm, respectively) and highly Yb-doped, which additionally speaks against an amplifier similariton based origin of the parabolic pulse shape, that typically requires lowly doped, longer gain fibers >1 m [RCW10; OCI10; Nie+11]. Instead, the gain fiber merely increases the pulse energy, which allows the approximately Gaussian pulse to evolve towards the parabolic shape in the successive passive fiber by an interplay

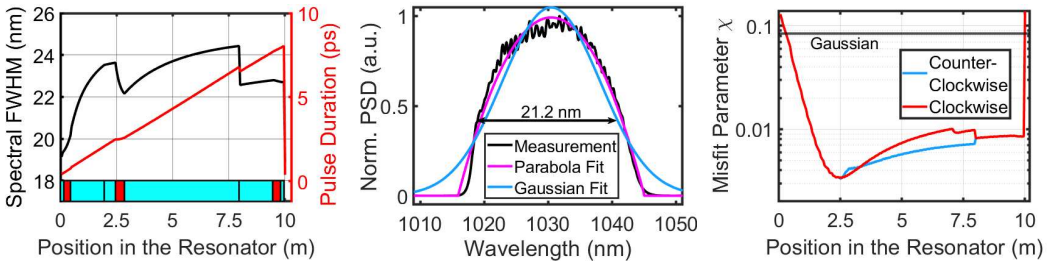

(a) (b) (c)

Figure 4.10: (a) Simulated evolution of the spectral FWHM (black line) and the pulse duration (red line). The starting point $z = 0\,\mathrm{m}$ is chosen to be at the cFBG. The sections marked with blue/red boxes correspond to passive/active fibers, respectively. Black lines in the blue boxes mark the beginning and ending of the NALM. Only the values for the counter-clockwise propagating pulse are shown. (b) Measured output spectrum at the cFBG together with Gaussian and parabolic fit. (c) Misfit parameter of the pulse during propagation.

of SPM and normal dispersion [Fin+07]. Opposed to the amplifier similariton, this pulse shaping is not asymptotically attractive and thus requires adjustment of pulse energy and passive fiber length with respect to each other. With this in mind, the length of the successive passive fiber becomes an important parameter, as too large propagation lengths at high pulse energy give rise to a loss of the parabolic shape and ultimately to wave breaking.

Temporal Pulse Characterisation The output signals are compressed using a Treacy type grating compressor [Tre69]. The transmission gratings are arranged in Littrow configuration and both have a grating period of 1000 nm. For this configuration the proportion of GDD to TOD inflicted by the compressor is fixed at $-0.354\,\mathrm{fs}^{-1}$ for the central wavelength 1030 nm. The grating distance is varied while the ACT of the compressed pulses is monitored using an autocorrelator (APE pulseCheck). At all fiber outputs, states of minimum pulse durations are obtained in the regime of high double-pass amplifier pump power and low NALM amplifier pump power [see grey marks in Fig. 4.8 (b)]. The corresponding measured compressed ACTs are shown in the first row of Fig. 4.11. Assuming the same pulse shapes as for the Fourier limited cases, the pulse durations at port 1, port 2, the cFBG output, and port 4 are 130, 155, 150, and 125 fs, respectively. Except for the signal at port 2, the pulses show a notable deviation from the Fourier limited case (red dashed lines

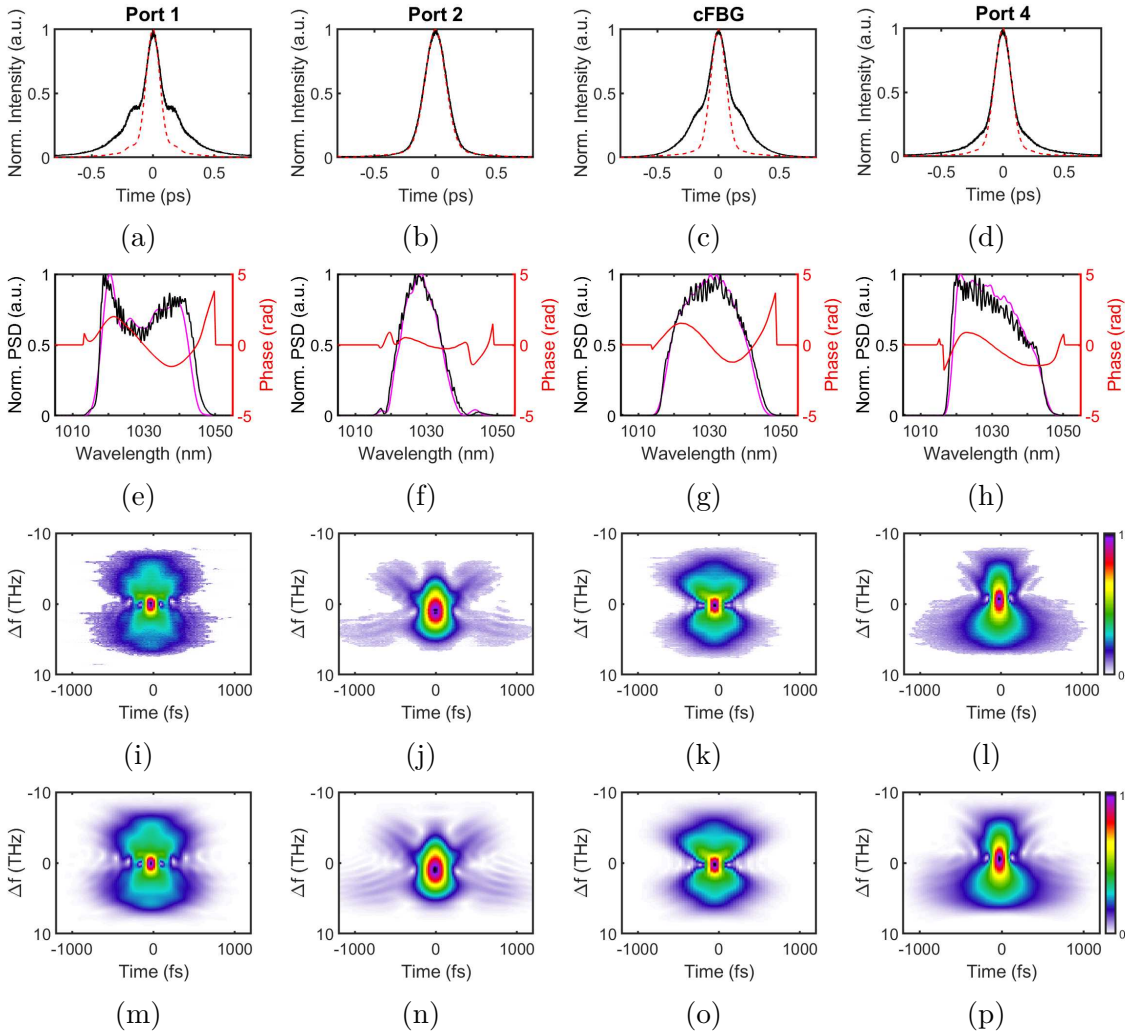

Figure 4.11: Temporal characterisation of the oscillator output. The first row shows the shortest measured ACT (black) of each output together with the Fourier limited ACT (red), retrieved from the spectra. The second row displays the corresponding measured spectra (black) together with the retrieved spectra (pink) and phases (red) from FROG measurements. The third row shows the measured and the fourth row the corresponding retrieved FROG traces.

in first row of Fig. 4.11). In order to retrace this deviation, a FROG (frequency resolved optical gating [KT93]) measurement has been performed using a FROGscan Ultra by MesaPhotonics. The measured FROG traces in the third row of Fig. 4.11 show good agreement with the retrieved FROG traces in the fourth row of Fig. 4.11. The second row of Fig. 4.11 depicts the retrieved spectra (pink) and spectral phases (red) together with the measured spectra (black) by the Yokogawa OSA from a

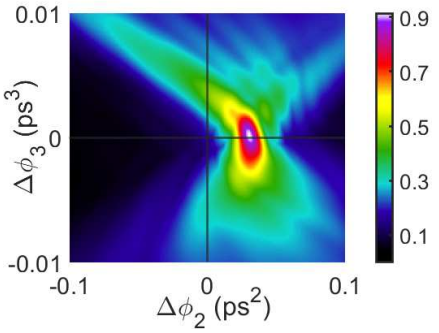

Figure 4.12: RPP when using the spectrum at the cFBG as a seed for nonlinear CPA with B =10 rad according to the formalism in 3.5.2.

parallel measurement. The retrieved pulse durations agree with the autocorrelation measurement within a range of ±10 fs. As expected, the spectral phase of the pulses at port 2 is relatively flat compared to the other output ports. The shapes of the spectral phases suggest that predominantly TOD is uncompensated. As the ratio of GDD to TOD by the grating compressor is fixed for grating distance variations, the pulses can only be further compressed by an additional pulse compressor which has a different ratio of GDD to TOD. For example, this could be done by a prism compressor [FMG84], or simpler, by using additional/less fiber at the output ports. The potentially shortest pulses are emitted by port 1 with a Fourier limited pulse duration of 95 fs.

In the regime of minimum pulse duration, the spectra exhibit short modulations ($\Delta\lambda \approx 1$ nm, corresponding to a pulse separation $\Delta t \approx 3$ ps) with a depth of up to 20 %, which are not replicated by the retrieved FROG spectra (see second row of Fig. 4.11). Theoretically, periodic modulations of this magnitude correspond to a side pulse that is suppressed by 25 dB with respect to the main pulse. A Fourier analysis of the spectrum with the strongest modulations, however, reveals that the side pulse contrast is ≈40 dB, since the modulation is not completely periodic. The origin of the modulations is likely caused by one of the components in the linear branch of the cavity as the modulation depth scales with the pump power in the double-pass amplifier. One possible source is the cFBG, which exhibits a slightly rippled reflection curve. Other explanations can be an insufficient isolation of the optical circulator allowing a fraction of the pulse energy to pass from circulator port 2 to port 1 or an imperfect splice connection, which introduces a polarisation rotation with parts of the pulse energy propagating in the fast axis and being projected back to the slow axis of the fiber at a later position, causing the time delay between the pulses. Regardless of the cause, the spectral modulations can be a limiting factor in terms of pulse energy scaling when the oscillator is used in a nonlinear CPA system (compare Section 3.5). Therefore, operation with lower double-pass amplifier pump

power and thus reduced spectral modulations might be preferable. In order to further evaluate the output spectra at the cFBG in terms of their suitability as nonlinear CPA seed, the formalism of Section 3.5.2 is applied again. Thereby, the nearly parabolic spectrum allows for a maximum RPP of 91 % after chirped amplification with a B-integral of B =10 rad (see Fig. 4.12), which suggests that the oscillator's spectra are well-suited for a deployment in a nonlinear CPA system.

4.3 Conclusion

The demonstrated novel oscillator concepts based on 3x3-coupler-NALMs possess remarkable properties. The dispersion managed setups enabled the generation of sub-ps pulses with output spectra that are appropriate for nonlinear CPA-setups for both 1 µm and 2 µm wavelength. Apart from an environmental robustness due to the all-PM-fiber setup, the oscillators are made up of components which are not known for long-term degradation effects, as is often the case for solid-state saturable absorbers operated close to their damage threshold. Moreover, solid-state saturable absorbers are often prone to optical damage by spiking and Q-switching instabilities below the mode-locking threshold, i.e. primarily during the start of the laser. Such phenomena are also observed during the start of the NALM-oscillators, however in the course of this work, no damage of any oscillator fiber component resulted. Additionally, the saturation behaviour of the NALM can be tuned flexibly via both the fiber length and the pump power, which enables mode-locking for various setups.

Yet, a drawback of the NALM-oscillators can be the comparatively large pump power required for self-starting, which exceeds the pump power at typical single pulse working points by a factor of 2. For solid-state based saturable absorbers, the mode-locking threshold is often much lower. Furthermore, some open issues should be addressed before the oscillators can be readily employed in CPA setups. In terms of large-scale production for example, it has to be verified that the typical manufacturing variations of the 3x3-couplers' parameters will not degrade the performance of the oscillators. Additionally, the usage of two pump sources comes with the problem of a hampered long-term power stabilisation of the oscillators, as the two laser diodes degrade at different velocities. Operating the oscillators with a single pump source is thus preferred.

CHAPTER 5

Monolithic Nonlinear Chirped Pulse Amplification Based on Thulium Doped Fibers

In the past decades, chirped pulse amplification (CPA) has become a prevalent method for the generation of ultrashort pulses ranging from the µJ to the J energy regime [SM85; Hor+16]. For the case of fiber lasers, where the propagating light is confined to small mode areas and interacting with the gain media over several meters, the reduction of the peak power by temporal stretching of the pulses is of particular relevance. Currently, ultrashort Yb-fiber laser systems still hold the record of 2.2 mJ in terms of obtainable pulse energy [Eid+11] and a peak power of 6.2 GW [Kle+14] from a single-channel fiber CPA system. Such magnitudes are not solely enabled by temporal stretching to 2-3 ns, but also by a spatial reduction of the peak intensity using sophisticated fiber designs. The increased core sizes in these fibers allow for an effective mode-area as large as 8600 µm^2 and also for short fiber lengths in the range of 1 m, due to an increased pump absorption, which further helps in mitigating nonlinear effects.

Tm-fiber systems, on the other hand, possess a wavelength advantage regarding the nonlinear parameter $\gamma = 2\pi n_2/(\lambda A_{\text{eff}})$. Apart from the direct dependence on the wavelength, γ also depends reciprocally on the effective mode-area A_{eff}, which by itself scales with λ^2 for constant NA and guiding properties, i.e. constant effective

V-parameter [Stu+14]. Thus it is expected, that the 2 µm systems will be able to surpass the 1 µm systems in terms of maximum pulse energy and peak power as soon as comparable effort is put in the development of appropriate Tm-doped large mode-area fibers. So far, the highest reported pulse energy and peak power from an ultrashort Tm-fiber system are 620 µJ, with a corresponding peak power of 5 GW, extracted from a 1.3 m long rod type fiber with an effective mode-area of $>3100\,\mu m^2$ [Gai+17; Jan+12a].

In terms of average power, ultrashort single-channel Tm-fiber systems have already surpassed their 1 µm counterpart with output powers exceeding 1 kW, despite the enormous heat loads (average of $\approx 100\,W/m$) evoked by the 793 nm pumping scheme [Gai+18]. Both of these outstanding demonstrations showcase the vast potential of a wavelength shift to 2 µm. The results have been enabled by direct, convective water cooling of the gain fibers in a tube and free-space coupling between the different amplifier fibers, which allow for highly effective heat removal and minimal B-integrals, respectively.

Conversely, the need for free-space to single-mode fiber coupling drastically reduces a system's stability, especially in the presence of large heat loads and an associated mechanical misalignment induced by the thermal expansion of the system's compounds. Moreover, the sharp spectral absorption lines due to water vapor in air impede a nonlinear CPA scheme, as the spectral dips in the seed spectrum are transferred to the nonlinear phase during amplification, resulting in a decreased RPP [Geb+15].

For these reasons, a monolithic amplifier chain with the different gain fibers and fiber components being linked by splice connections is highly desirable. Such a system has thus far not been demonstrated for output powers in excess of 78 W [WYL13b] and pulse energies of 54 µJ [WYL13c] in the context of ultrashort pulses. In the following Chapter, the endeavour of developing such a system with the objective of large pulse energies as well as a large average power output is outlined.

5.1 Experimental Setup

A scheme of the experimental setup of the Tm-CPA system is shown in Fig. 5.1. The seed pulses are generated in a commercial mode-locked Er-fiber laser ($f_{\mathrm{Rep}} =$

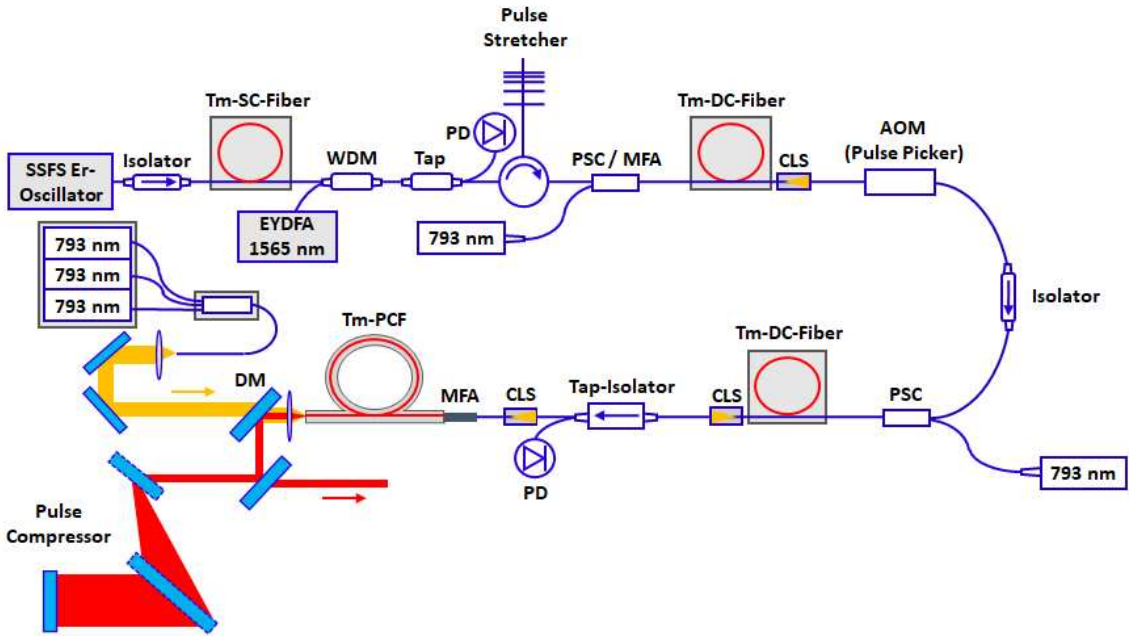

Figure 5.1: Scheme of the developed nonlinear Tm-fiber CPA system. AOM: acousto optic modulator, CLS: cladding light stripper, DC: double-clad, DM: dichroic mirror, EYDFA: erbium-ytterbium co-doped fiber amplifier, MFA: mode field adapter, PCF: photonic crystal fiber, PD: photo diode, PSC: pump signal combiner, SC: single-clad, SSFS: soliton self frequency shift, WDM: wavelength division multiplexer.

24.3 MHz), whose central frequency is tunable in a wide range from 1700-2100 nm [Sob+17] via subsequent soliton self frequency shift (SSFS) in a highly nonlinear fiber [MM86; Gor86]. This seed allows for sub-100 fs pulse durations at a central wavelength of 1955 nm, which is fixed for the experiments. The 70 pJ pulses are pre-amplified in a 20 cm long, first Tm-SC-amplifier stage to an average power of 10 mW prior to being stretched to a FWHM pulse duration of 650 ps using a cFBG. The impact of nonlinear effects is further reduced by switching from a SC-fiber with a MFD of 8 µm (core diameter of 7 µm, NA of 0.2) to a DC-fiber with MFD of 11 µm (core diameter of 10 µm, core NA of 0.15). The average power can then be boosted to a level of 1.5 W by two 2 m and 2.5 m long Tm-DC amplifiers co-pumped by 793 nm multi-mode diodes with a maximum power of 4 W and 8 W. As the pump light in the DC fibers is guided by the fiber coating with low refractive index, removing the coating and placing the fiber in a transparent silicone with a larger refractive index allows for efficient extraction of residual pump light after the DC-amplifiers. The gain fibers are cooled passively by taping them to aluminium boards. Between the

DC-amplifiers, the pulse repetition rate can be optionally reduced by an acousto optic modulator (AOM). After the SC-amplifier and the second DC-amplifier, tap couplers are used to monitor the pulse clock signal via photo diodes. In case of loss of the clock signal, the pump power of subsequent amplifiers is turned off in order to mitigate the risk of spiking damage. The 3.4 m long main amplifier is a Tm-doped photonic crystal fiber (PCF) which is coiled to a diameter of 40 cm. The PM-fiber is fixed on a water cooled aluminium cassette using a cured silicone and is counter-pumped by three combined multi-mode pump modules at wavelength 793 nm with 90 W output power each. In order to prevent surface damage due to high optical intensities, an anti-reflection coated glass end cap is spliced to the end face of the PCF. The end cap reduces the optical intensity at the air-glass interface as the signal beam expands spatially before leaving the glass. Furthermore, the protective coating of the PCF is stripped over a length of several centimeters at the fiber end. This allows for a stripping of pump light, which is not coupled into the pump cladding of the fiber, by virtue of the high-index silicone. The stretched output pulses are compressed in a Treacy type compressor with transmission gratings that have a grating period of 1250 nm.

Fabrication and Characterisation of the MFA in front of the PCF The transition to the Tm-doped PCF main amplifier is non-trivial, since the connected fibers differ largely in their outer diameters, as well as in their MFDs and guiding structures. Getting a handle on this transition is the enabling step towards a monolithic high-power amplifier chain. For this purpose, a short section of a step-index transition fiber with increased core and cladding diameters (20/400 µm, core NA = 0.1) is used [see Fig. 5.2 (a)]. The motivation for this transition fiber is manifold: Firstly, a step-wise change of the MFD allows for lower overall splice losses. The minimum splice loss between two single-mode fibers due to a MFD-mismatch can be approximated by [Mar77]

$$\alpha = \left(\frac{\mathrm{MFD}_1^2 - \mathrm{MFD}_2^2}{\mathrm{MFD}_1^2 + \mathrm{MFD}_2^2} \right)^2 . \tag{5.1.1}$$

With the step-wise increase of the MFD from 11 to 36 µm the splice loss can be reduced from a theoretical value of 5 dB of a direct splice connection to a measured

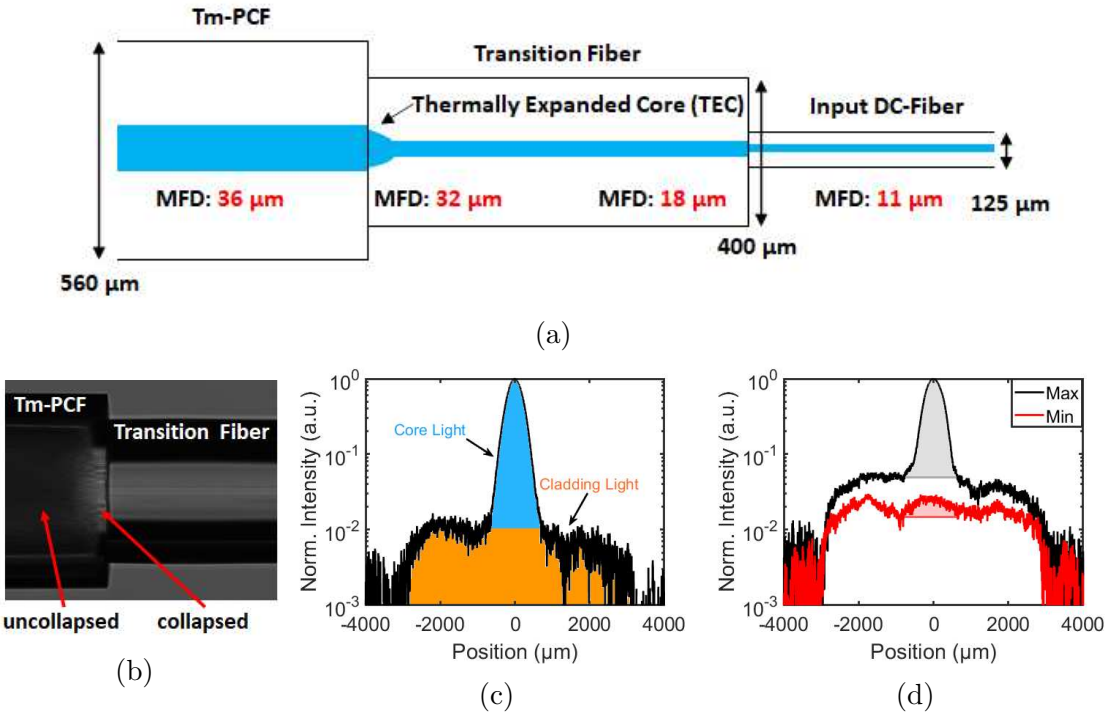

Figure 5.2: (a) Scheme of the MFA in front of the main amplifier. (b) Photography of the splice connection between the PCF and the transition fiber. Splice parameters were chosen to get both minimum collapse of the PCF's air structure and mechanical stability of the splice. (c) Measurement of the core-cladding-ratio after the PCF at a central wavelength of 2050 nm. The blue and orange shaded regions indicate the power in the core and cladding, respectively. (d) Measurement of the PER after the PCF at central wavelength 1950 nm. The two depicted signals correspond to the waveplate position of maximum and minimum transmission, respectively. For the determination of the PER, the signal is corrected for the cladding light, i.e. only the shaded regions are taken into account.

value of ≈ 2 dB (power in the core of the PCF, measured at central wavelength 2050 nm). Secondly, residual pump power in the 260 µm pump cladding of the PCF would hit the 125 µm input fiber and its coating in an uncontrolled manner. The 400 µm transition fiber allows for controlled outcoupling of the residual pump by acid roughening of its side surface. Thirdly, the signal and pump guidance in the PCF relies on air structures in the fiber which are easily damaged during the splice process. Splicing the PCF to a fiber of comparable size allows for a shift of the heated zone away from the PCF which reduces the collapse of the air structures without substantially weakening the resulting splice connection [see Fig. 5.2 (b)].

Before the splice process, the transition fiber is processed to contain an adiabati-

cally expanded core [Kih+96]. For this purpose, the beam of a CO_2-laser is focused on the fiber for several hours in order to thermally expand the fiber core, and thereby the MFD, locally. Afterwards, the fiber is cut back in small steps ($\approx 0.5\,\mathrm{mm}$) near the heat affected region while the output MFD is measured. With the used fiber, a maximum MFD of $32\,\mu\mathrm{m}$ could be obtained without a noticeable weakening of the structural integrity of the fiber. After splicing the fibers, the surface of the transition fiber is etched with hydroflouric acid which enables lateral outcoupling of residual pump light of the counter-pumped main amplifier.

In order to characterise the MFA, the wavelength-shifted and tunable Er-based seed was spliced to the input fiber and used as a light source for the measurements. In passive measurements (i.e. no pump power is applied to the Tm-PCF), the ratio between power that is propagating in the core and power that is propagating in the cladding of the PCF, as well as the polarisation extinction ratio (PER) of the core light were measured. For this purpose, the output signal of the PCF is imaged onto a scanning slit beam profiler in a 4-f-setup. The core-cladding-ratio strongly depends on the central wavelength used for the measurement, as the Tm-ions in the core partially absorb the signal light and re-emit the fluorescence light virtually at a random solid angle. Due to the large NA of the pump cladding (> 0.4), the re-emitted light is partially guided therein and distorts the measurement at the fiber exit. In order to mitigate this effect, the core-cladding-ratio measurement was performed at a central wavelength of 2050 nm, where the absorption cross section σ_a of the Tm-doped glass is reduced considerably [see Fig. 5.2 (c)]. The core-cladding-power-ratio at this wavelength is evaluated to be $\approx 80\,\%$.

For the measurement of the PER, a $\lambda/2$-waveplate and a polariser were inserted between the imaging lenses. These optics are specified for a central wavelength of 1950 nm and perform worse when used at deviating wavelengths. The measurement is thus performed at a central wavelength of 1950 nm and it is assumed, that the core signal loss due to fluorescence affects both polarization axes in the same manner. When rotating the waveplate to the position of minimum transmission through the polariser, the core signal nearly vanishes relative to the cladding signal [see Fig. 5.2 (d)]. Thereby, the exact determination of the PER is impeded. Yet the measurement allows for a determination of a lower bound of 18 dB, which indicates that the excitation of the unwanted polarization mode is well prevented.

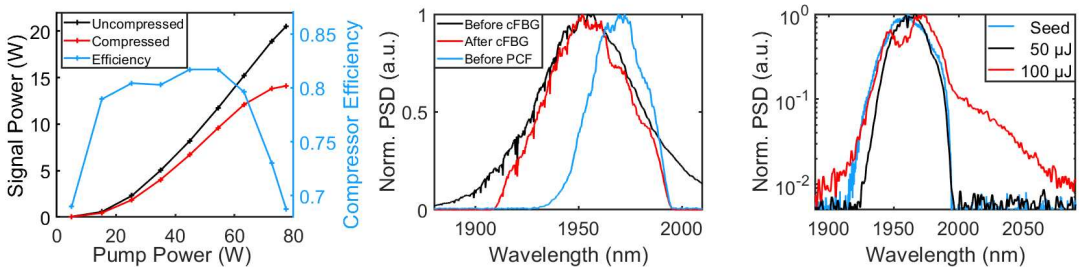

(a) (b) (c)

Figure 5.3: (a) Measured output power of the Tm-PCF pumped at 793 nm at a pulse repetition rate of 200 kHz before and after the compressor (i.e. uncompressed and compressed pulses). The blue line indicates the compressor efficiency. (b) Measured spectra of the seed signal before (black) / after (red) the cFBG and before the main amplifier (blue). (c) Measured seed and output spectra of the Tm-PCF at a pulse energy level of 50 and 100 µJ, respectively. The measurement resolution is low which hides short modulations generated by side pulses [see e.g. Fig. 5.9 (e)] but allows for an identification of the other spectral changes.

5.2 High Pulse Energy Operation

In a first experiment, the CPA-system is modified for high pulse energy output. For this purpose, the pulse repetition rate is reduced to 200 kHz via the AOM. High pulse energy operation is typically limited by the accumulation of a large nonlinear phase which becomes increasingly difficult to compress using a grating compressor, as the temporal pulse shape deviates from a parabola [see Section (3.5)]. In order to minimise the accumulated nonlinear phase before and in the main amplifier, the seed power / seed pulse energy for the Tm-PCF is preferably chosen small. On the other hand, if the seed power is too small, the saturation of the main amplifier, and thus the efficiency, becomes low. Therefore an input power of 50 mW is chosen, corresponding to a pulse energy of 250 nJ. In this configuration, the Tm-PCF allows for an amplification to 20.5 W, corresponding to an output pulse energy of 102 µJ. The pump power is not increased further at this output power level as the slope efficiency starts to decrease from 39.5 % to 33 %. Also, when compressing the output power in the grating compressor, a decline in the compressor efficiency from >80 % to <70 % at maximum pulse energy can be noticed [see Fig. 5.3 (a)], resulting in a maximum compressed output pulse energy of 70 µJ.

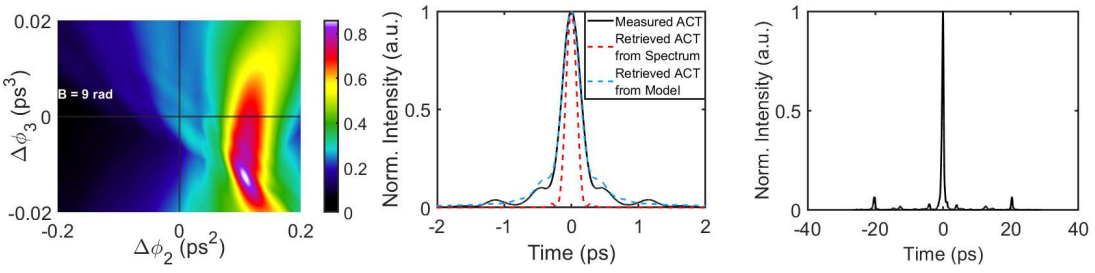

(a) (b) (c)

Figure 5.4: (a) Relative peak power of the output pulses as a function of the dispersive stretcher/compressor phase mismatch for a B-integral of 9 rad according to the model in Section (3.5). (b) Measured ACT of the compressed output pulses at a 100 µJ level together with the Fourier limited ACT retrieved by the spectrum. (c) Measured ACT of the same state at a wider temporal scanning range.

Analysis of the Output Spectra Figure 5.3 (b) shows the spectra before/after the fiber stretcher and also directly in front of the main amplifier. The curves indicate a significant spectral shaping by the gain in the pre-amplifiers. As these amplifiers are operated at a low pump power and consequently low inversion, the effective gain shifts towards longer wavelengths. Consequently, the spectral FWHM reduces from 48 nm to 34 nm, resulting in a reduction of the chirped pulse duration from 650 to <500 ps, which significantly enhances the impact of nonlinear effects.

At the pulse energy level of 100 µJ, additional changes in the output spectra become apparent [see Fig. 5.3 (c)]. Apart from a spectral dip near the central frequency, a broad long-wavelength background is generated. These spectral components are clipped by the second compressor grating which leads to the decline in compressor efficiency. Possible origins of the spectral changes are amplified spontaneous emission (ASE), SRS and/or modulation instability [Li+15].

ASE does not deliver an explanation for the spectral dip near the center frequency. Moreover, an increase in seed power enhances both spectral modifications, which evidently indicates that not an insufficient saturation of the amplifier causes the modifications but rather a nonlinear effect. The Raman gain spectrum in silica exhibits a broad peak near 13 THz, which would correspond to a wavelength shift of ≈ 170 nm to the wavelength regime >2100 nm. In this wavelength regime, no spectral components are observed. However, as Raman scattering is a phonon mediated process, the scattered Stokes Raman intensity exhibits a temperature dependence,

which enhances the Raman scattering cross section for lower frequency shifts at larger temperatures T [MK79]. At the output power level of 20 W, the end of the fiber amplifier reaches a surface temperature of >180 °C due to the large heat load induced by the 793 nm pump. The increased probability for spontaneous generation of low energy phonons at high temperatures might thus act as seed for SRS which could reduce its threshold significantly. Alternatively, a different nonlinear process based on degenerate four-wave mixing phase-matched by SPM, i.e. modulation instability, is known to limit the large peak power propagation in the anomalous dispersion regime [Li+15; Sin+18]. Taking into account that the observed spectral changes occur primarily for larger wavelengths might also indicate an interplay between both effects, e.g. a modulation instability seeded by Raman scattering. Ultimately, further examination will be needed to doubtlessly identify the limiting nonlinear mechanism.

A further scaling of the pulse energy requires additional mitigation of nonlinearities by either a further peak intensity reduction during amplification (spatial and/or temporal) or a reduced fiber length. The fiber length of 3.4 m is not optimised for high pulse energy operation but rather dictated by the used cooling cassette. With an optimised design incorporating a fiber length of 2-2.5 m, an amplification to the same power level would still be admissible even though the accumulated nonlinear phase would be reduced. Additionally, an edge filter in front of the main amplifier could be used to prevent the seeding of SRS by previous amplifier stages.

Temporal Output Characterisation Despite a large nonlinear phase of 9 rad, which is estimated via the signal power $P(z)$ obtained from a rate-equation based calculation of the fiber, i.e.

$$B = \frac{2n_2}{\lambda_c f_{\mathrm{Rep}} t_p w^2} \int_0^L P(z)\mathrm{d}z, \tag{5.2.1}$$

a compression to 220 fs [see Fig. 5.4 (b), Fourier limit of 170 fs] is possible using the Treacy type compressor. The autocorrelation trace, however, shows pulse shoulders and tails that could not be compensated for by iteratively tuning the compressor incidence angle and the distance between the compressor gratings. This indicates that there is residual higher-order nonlinear phase, which cannot be compensated by the grating compressor. In fact, when applying the input spectrum to the model from Section (3.5) and assuming a B-integral of 9 rad, a resulting maximum RPP

of ≈85 % can be estimated [see Fig. 5.4 (a)]. From this plot, it also becomes clear that the slightly asymmetric input spectrum demands a partial compensation of SPM by TOD in order to reach the maximum RPP. The retrieved ACF of the model at maximum RPP is also plotted in Fig. 5.4 (b) and qualitatively shows good agreement with the measured ACT, despite the substantial spectral changes during amplification.

Moreover, the wide-range ACT reveals side pulses with a suppression of 12 dB at 20 ps and >17 dB at 13 ps delay [see Fig. 5.4 (c)[1]]. Care has to be taken when interpreting the side-pulses in the ACT due to the convolution of the pulses during the measurement. A side-pulse suppression of 12 dB in the symmetric intensity ACT, for example, can be caused by a single pre- *or* post-pulse that is suppressed by 12 dB or by a pre- *and* a post-pulse that are suppressed by 15 dB each. Typically, the latter is the case, as pre- and post-pulses are coupled via the nonlinear amplification [Did+08; KCJ20]. In both cases, however, the energy content missing from the main pulse is approximately the same, assuming the same pulse shape and duration for the main and side pulses. Thus, the side pulse energy content is estimated to about 6 %. The resulting peak power of the main pulse is, however, additionally decreased due to the signal absorption by water vapor and the respective distortion of the refractive index, i.e. the pulse's phase via the Kramers-Kronig-relations in the free-space compressor [Geb+15]. The amount of the decrease can be estimated by the loss of average power, i.e. the relative loss of peak power is approximately twice as large as the relative absorbed average power at a relative humidity of 60 % [Geb+15]. From the known theoretical compressor efficiency of 88 % and Fig. 5.3 (a), it can be estimated that a maximum of 6 % of the average power is dissipated by the water absorption during pulse compression. The resulting peak power is thus reduced by an additional 6 % and can be conservatively estimated to be 250 MW.

The emergence of side pulses is a familiar feature of CPA systems operating at large B-integral levels [Gal+01; KCJ20]. As discussed in Section 3.5, their noticeable onset can be shifted towards larger nonlinear phase shifts by a higher side-pulse contrast and/or a lower modulation of the seed's spectral phase. However, as the energy in the side pulses scales overproportionally with the B-integral, i.e. the pulse contrast degrades with increasing B-integral, the side pulses eventually become

[1] The smaller side pulses at 4 ps delay are an artefact of the autocorrelator, which are present in every AC measurement and stem from a broadband metal mirror inside the device.

apparent, setting an additional upper limit for high pulse energy operation of the system.

Nearly Diffraction-Limited Beam Quality In general, the parameters of the main amplifier do not allow for the exclusive propagation and amplification of the fundamental transverse fiber mode (V-number ≈ 3.2). However, due to a smaller overlap of higher-order modes with the doped core [SO99; Lim+12], i.e. higher-order mode discrimination by amplification, an effective single-mode operation can be obtained. Nevertheless, if for example the launching conditions due to the splice connection are not ideal, higher-order modes of the PCF can be excited significantly and decrease the output beam quality. In order to confirm the suppression of higher-order modes, the output beam is characterised using a scanning slit beam profiler (see Fig. 5.5). For this purpose, the collimated beam is focused by a lens and the 4σ-beam-width d is evaluated in two perpendicular axes along the resulting beam caustic. Fitting the squared beam width along the z-axis to a parabola allows for the extraction of the beam quality factor M^2 [EDE04]:

$$d_{x/y}^2(z) = A_{x/y}z^2 + B_{x/y}z + C_{x/y} \quad \longrightarrow \quad M_{x/y}^2 = \frac{\pi\sqrt{4A_{x/y}C_{x/y} - B_{x/y}^2}}{8\lambda}. \quad (5.2.2)$$

The near diffraction-limited beam quality factor $M^2 \approx 1.1$ measured for both axes at 20 W output power confirms a strong suppression of higher-order modes. Moreover, the good beam quality indicates negligible beam deterioration by thermal blooming induced by signal absorption of water molecules in air at this power level [Smi77]. This can be attributed to the choice of the large central wavelength which prevents an overlap of the signal spectrum with strong water vapor absorption lines.

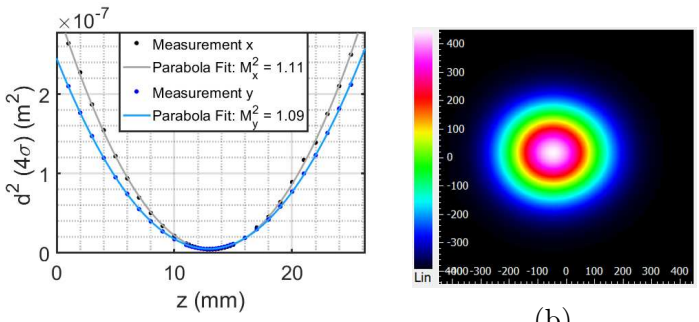

(a) (b)

Figure 5.5: Examination of the beam profile after the main amplifier. (a) Measurement of the (squared) 4σ-beam-width along the beam caustic together with a parabola fit. The measurement was performed at an output power of 20 W using a scanning slit beam profiler. (b) Reconstruction of the beam profile from the x- and y-cuts of the scanning slit measurement at $z = 5$ mm.

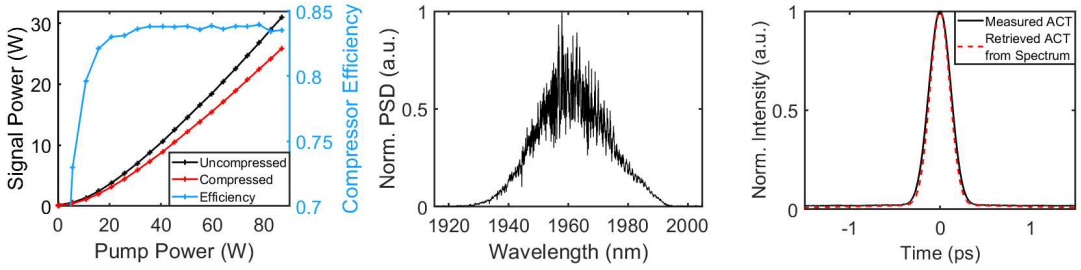

(a) (b) (c)

Figure 5.6: (a) Measured output power of the Tm-PCF pumped at 793 nm at a pulse repetition rate of 1.52 MHz before and after the compressor, i.e. uncompressed and compressed pulses. The blue line indicates the compressor efficiency. (b) Measured output spectrum of the Tm-PCF (resolution 50 pm) at a pulse energy level of 20 µJ. (c) Measured ACT of the compressed output pulses at a 20 µJ (16 µJ compressed) level together with the Fourier limited ACT retrieved from the spectrum.

5.3 High Average Power Operation

As the limits in terms of extractable pulse energy at borderline acceptable pulse quality are identified, the average power limitation of the system shall be explored in a next step. For this purpose, the pulse repetition rate is increased to 1.52 MHz. The seed power for the main amplifier is increased to 0.6 W corresponding to a seed pulse energy of 0.4 µJ. Due to the increased saturation of the main amplifier, the slope efficiency of the main amplifier now increases from previously 39 % up to 47 % at an output power of 31 W and a corresponding pulse energy of 20 µJ [see Fig. 5.6 (a)]. The compressor efficiency at this power level is still well above 80 % and the 185 fs compressed output pulses exhibit a good pulse quality without noticeable side pulses or pulse tails in the ACT [see Fig. 5.6 (c)]. However, the spectrum already reveals the onset of the nonlinear amplification in the shape of the high frequency spectral modulations, which reveal a decreased side pulse contrast [see Fig. 5.6 (b)]. The corresponding B-integral is estimated to a level of 2 rad via the rate-equation based calculation.

At the maximum average power, the end of the main amplifier, which experiences the largest heat load due to the counter pumping scheme, reaches a surface temperature of >180 °C [see Fig. 5.7 (a)]. The silicone, which is used to embed the PCF and thermally connect it to the cooling cassette, is specified to operate up to temperatures of ≈200 °C, why a further increase of pump power has been refrained from. An even stricter limit to the upper temperature is set by the protective coating of the PCF; a maximum temperature of 80 °C is specified by the manufacturer under long-term operation. Based on the rate-equation calculation, a maximum heat load of 35 W/m can be estimated at the fiber end in the current setup [see Fig. 5.7 (b)]. Ultimately, an alternative cooling concept with a better thermal connection of the fiber to the cooling cassette is inevitable, since maximum thermal loads in the range of 100 W/m are expected when aiming for the 100 W signal power regime.

Thermal Considerations Apart from the damage concerns and the increased Raman scattering, the temperature of the Tm-PCF affects the amplification process in different ways: As the refractive index of silica is temperature dependent ($\mathrm{d}n/\mathrm{d}T \approx 1.1 \cdot 10^{-5}\,\mathrm{K}^{-1}$ [WN69]), the heat load in the fiber core leads to a change in

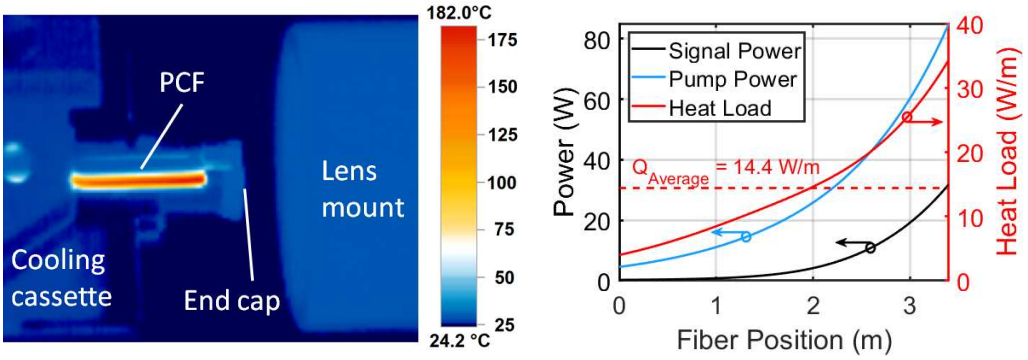

(a) (b)

Figure 5.7: (a) Thermal image of the end of the main amplifier at an output power of 30 W. (b) Rate-equation based calculation of the signal power and heat load along the PCF.

the lateral refractive index profile, which can considerably reduce the mode-area of the fundamental fiber mode at high power operation of large mode-area fibers (MFD $> 50\,\mu m$) [Jan+12b] and thus enhance the impact of nonlinearities. As the effect is caused by the temperature gradient inside the fiber, it scales with the heat load and can hardly be mitigated by external cooling conditions. The mode shrinkage is reportedly larger for the case of a large mode-area Tm-fiber [Jan+12a], presumably due to the larger heat load compared to Yb-fibers [Gai+21]. However, the PCF used in this work has a comparatively small MFD ($\approx 36\,\mu m$) and no shrinkage thereof was observable at any output power level.

Moreover, high-power fiber lasers are subject to transverse mode instabilities (TMI), which limit the achievable output power at stable, near diffraction limited beam quality [JSL20]. According to a broadly accepted explanation, the effect stems from a thermally induced refractive index grating along the fiber which is caused by the beating of different transverse modes [SS11; Jau+12]. For Tm-fiber lasers pumped at 790 nm, a numerical evaluation indicates that the heat load evoked TMI-threshold is notably higher than for Yb-lasers [SS16]. This is attributed partially to a λ^{-1} scaling of the mode coupling between the fundamental and higher-order modes and partially to the shape of the transverse heat load profile, which is favourably affected by cross-relaxation in Tm-fibers. Additionally, photodarkening has been revealed as a significant heat source that reduces the TMI-threshold in Yb-fiber lasers [Ott+15]. A smaller influence of photodarkening in Tm-fibers pumped at 790 nm might also

impact the TMI-threshold beneficially [SS16]. Experimentally, the higher resilience to TMI in Tm-doped fibers prevents many observations of the effect and extreme average heat loads as large as 300 W/m have been reported before the onset of TMI [Gai+21]. For comparison, the average heat load threshold of Yb-fiber lasers is at a level of <35 W/m [Jau+15]. As the desired output power of the Tm-PCF is at a level of 100 W, an average heat load of <40 W/m is anticipated, which is still well below the TMI-threshold in a Tm-fiber. However, it should be kept in mind that the reported results rely on direct, convective water cooling of the amplifier fibers. The impact of a decreased cooling has revealed a reduction of the TMI-threshold by up to a factor of 2/3 in Yb-fiber lasers [WRD12].

Apart from that, the fiber temperature affects the emission and absorption of the Tm-ions due to a modified population distribution of the energy level manifolds by thermal excitation. According to the McCumber relation, the stimulated emission and absorption cross sections of the upper and lower laser levels (σ_e and σ_a, respectively) are linked by a temperature dependent exponential term [McC64]:

$$\frac{\sigma_\mathrm{e}(\lambda, T)}{\sigma_\mathrm{a}(\lambda, T)} \propto \exp\left(\frac{E_\mathrm{ZPL} - \frac{hc}{\lambda}}{k_\mathrm{B} T}\right). \tag{5.3.1}$$

Here, E_ZPL is the zero-phonon-line energy, which can be approximated to be at the wavelength where $\sigma_\mathrm{e}(\lambda, T) = \sigma_\mathrm{a}(\lambda, T)$ [Kou07], i.e. at a wavelength < 1800 nm for the considered transition ($^3\mathrm{F}_4 \leftrightarrow {}^3\mathrm{H}_6$) in the Tm-doped fiber. Therefore, an increase of the fiber temperature generally leads to a reduced emission cross section and/or an increased absorption cross section at the signal wavelength, which can notably reduce the overall efficiency of the amplification process in Tm-doped fibers [FL06; Tur+08].

Scaling to >100 W Average Power With these points in mind and in order to prevent thermal damage of the main amplifier, an improved cooling scheme becomes necessary to further scale the output power. The silicone, that has been used to thermally connect the fiber with the cooling cassette so far, has the advantage of a very low viscosity in the uncured state, which allows for mitigation of air cavities during casting. Air cavities in the silicone can create local hot-spots due to the low thermal conductivity of air. Moreover, the silicone has the advantage of being transparent at

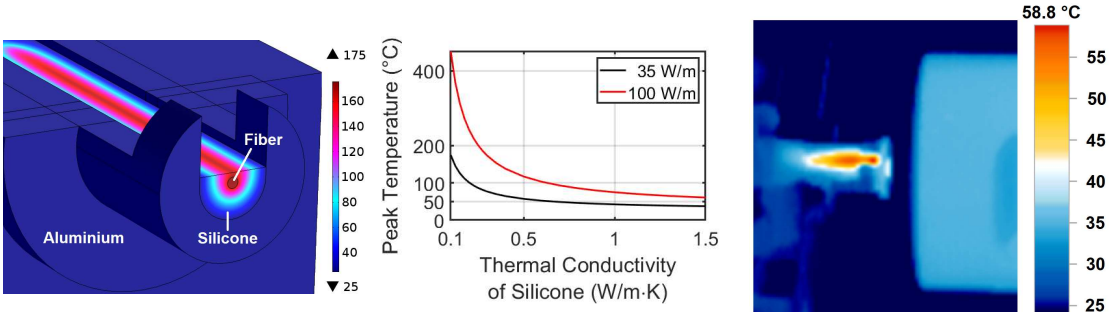

(a) (b) (c)

Figure 5.8: (a) Thermal FEM simulation of the fiber amplifier embedded by the silicone in the cooling cassette. The coolant temperature of the cassette is 25 °C, the thermal conductivity is $\kappa = 0.1\,\mathrm{W/(m \cdot K)}$, and the heat load q in the fiber is 35 W/m. (b) Dependence of the silicone peak temperature on the thermal conductivity of the silicone simulated for two different heat loads 35 W/m and 100 W/m. (c) Thermal image of the end of the main amplifier at an output power of 100 W.

the pump wavelength, which prevents strongly localised heating at the fiber-silicone interface due to absorption of miss-coupled pump light. However, the main drawback of the silicone is its low thermal conductivity of $\kappa \approx 0.1\,\mathrm{W/(m \cdot K)}$, which impedes the conductive heat removal and thereby causes the high fiber temperatures. Figure 5.8 (a) shows a thermal simulation of the end-piece of the amplifier based on the finite element method (FEM)[2]. The fiber is modeled as a glass rod with a diameter of 560 µm. The heat density deposited in its core is $Q = q/(\pi r_{\mathrm{core}}^2)$ with $r_{\mathrm{core}} = 25\,\mu\mathrm{m}$. It is embedded in the silicone which thermally connects it to the aluminium cassette. To simulate the water cooling of the cassette, its bottom face is kept at a constant temperature of 25 °C. Despite a comparatively low heat load of $q = 35\,\mathrm{W/m}$ along the fiber, the temperature at the fiber-silicone interface rises to a value of >170 °C. In Fig. 5.8 (b) a parameter scan of the simulation is shown for different thermal conductivities of the silicone and also for a larger heat load of 100 W/m. The results show, that even high thermal loads, and thus average powers, can be handled when increasing the thermal conductivity to a value around $1.5\,\mathrm{W/(m \cdot K)}$.

In a second iteration, the transparent silicone is thus replaced by a thermally conductive silicone [$\kappa = 1.4\,\mathrm{W/(m \cdot K)}$]. In order to increase the thermal conductivity,

[2] The simulation was done with the heat transfer module of the commercial software COMSOL. https://uk.comsol.com/heat-transfer-module Accessed: 2021-11-08

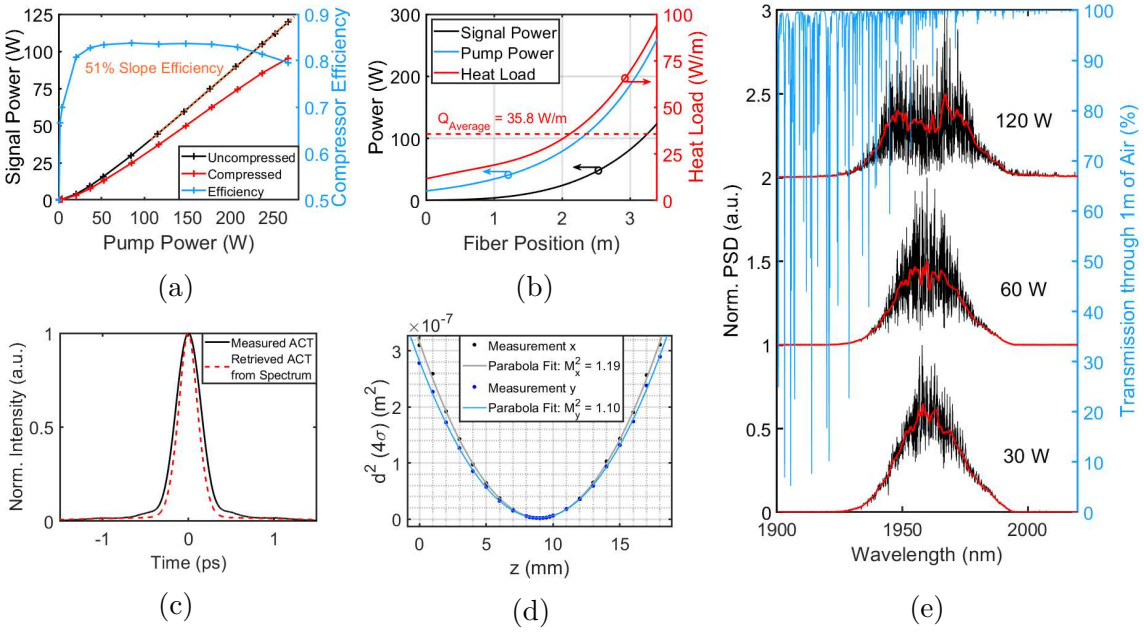

Figure 5.9: (a) Output power of the main amplifier in dependence of the pump power at a pulse repetition rate of 2.43 MHz. (b) Rate-equation based calculation of the signal power and heat load along the PCF at an output power of 120 W. (c) Measured ACT at an output power of 60 W (50 W compressed power) together with the Fourier limit retrieved from the corresponding spectrum. (d) Measurement of the (squared) 4σ-beam-width along the beam caustic together with a parabola fit. The measurement was performed at an output power of 100 W using a scanning slit beam profiler. (e) Output spectra of the main amplifier at different power levels measured in high (black line, 100 pm) and smoothed, low (red line, 400 pm) resolution. Blue curve corresponds to the transmission spectrum through 1 m of air by a uniform white light source at a water vapour pressure of 20 hPa based on [Rot+13].

such silicones typically contain metallic particles, which simultaneously render them intransparent in the visible / near infrared region and increase their viscosity in the uncured state. In order to allow for an air-cavity-free casting, a compromise between thermal conductivity and viscosity of the silicone must be made. Additionally, the cured state of the silicone needs to be soft enough to avoid stress on the fiber, which would induce a coupling between the two polarisation modes of the fiber [NOS86] or between the fundamental and higher-order modes.

With the silicone exchanged in the experimental setup and a larger repetition rate of 2.43 MHz, the output power can now be increased up to a pump power limited value of 120 W [see Fig. 5.9 (a)], despite low temperatures of $< 70\,^{\circ}\mathrm{C}$ at the end of the amplifier [see Fig. 5.8 (c)]. From the rate-equation based simulation, a

corresponding average heat load of 36 W/m can be estimated with a peak of 95 W/m at the fiber end [see Fig. 5.9 (b)]. In this setup, the seed power is increased to a value of 0.8 W (330 nJ seed pulse energy) in order to allow for a better saturation of the amplifier, however, at the cost of a larger B-integral. Due to these measures the slope efficiency is increased to 51 %. The resulting maximum pulse energy is 49 µJ, which corresponds to a numerically retrieved B-integral of 6 rad. At this nonlinearity level, the compressor efficiency starts to decline again due to the power transfer to longer wavelengths. Yet, the compressor efficiency of 80 % still enables a compressed output power of 95 W. However, the measured ACT fluctuates on a sub-second scale which prohibits the determination of the pulse duration. When the output power is reduced to 60 W the pulse duration can be measured [see Fig. 5.9 (c)]. Although attenuated, the pulse duration fluctuations at this power level are still present. The observed phenomenon can be traced back to beam distortions caused by thermal blooming [Smi77]. During free-space propagation, the narrow-band, molecular absorption lines, discussed in Section 3.5 cause a change of the refractive index of air by virtue of the Kramers-Kronig relations. Despite the large central wavelength of 1965 nm, the short-wavelength side of the spectrum still has an overlap with the absorption lines [see blue curve in Fig. 5.9 (e)]. The overlap can give rise to significant distortions of the output beam at high power operation and long propagation distances [Geb+15], as the turbulent heated air induces fluctuating thermal lenses [AR19]. The effect can be mitigated by purging the compressor compartment with e.g. dry air or helium [Gai+18]. Figure 5.9 (d) displays the measurement of the beam quality immediately after the main amplifier at an output power of 100 W. The beam quality factor M^2 exhibits only a minor deterioration and is still below 1.2, which also signals that the disturbance of the pulse compression is a result of propagation effects experienced in the compressor compartment and excludes TMI as a possible source.

5.4 Summary

In summary, an ultrafast, all-fiber Tm-CPA-system was realised, with the purpose of achieving pulse energies >50 µJ as well as average output powers in the regime of 100 W. The system consists of a commercially available, wavelength-shifted Er-fiber laser, whose output pulses are subsequently stretched to 650 ps via a cFBG,

amplified in three pre-amplifiers and one main-amplifier, and recompressed in a grating compressor. The repetition rate of the system can be tuned via an AOM-based pulse picker.

In order to examine the limitation in terms of compressible pulse energy, a low repetition rate of 200 kHz was chosen. The compressed output power showed a saturation around 14 W corresponding to a maximum compressed pulse energy of 70 µJ. The respective spectrum reveals a nonlinear power transfer towards longer wavelengths which prevents further pulse energy and peak power scaling. Despite a large B-integral of 9 rad, the pulses could be compressed to a pulse duration of 220 fs resulting in an estimated peak power of 250 MW.

At a larger repetition rate of 2.43 MHz, the system enabled a pump power limited average power of 120 W corresponding to a compressed pulse energy of 39 µJ. The respective large thermal load could be handled by embedding the fiber in a silicone with a large thermal conductivity of $1.4\,\mathrm{W/(m \cdot K)}$. For increasing output power, the overlap of the spectrum with the water absorption lines led to an onset of heat-induced fluctuations of the beam in the free-space compressor, which manifests in a varying pulse duration. The results indicate that the shift of the central wavelength beyond 1950 nm alone is insufficient to avoid this effect. Further shifting the wavelength towards 2000 nm, however, largely reduces the amplification efficiency due to the decreasing emission cross-section in the Tm-fiber, ultimately rendering the humidity control in the free-space compartment of the system imperative.

CHAPTER 6

Conclusion

Ultrashort pulse Tm-doped fiber laser technology is still not on a par with the Yb-doped counterpart in terms of many important aspects. This is strongly reflected in the availability of key components, such as SESAMs or very large mode-area fibers. In recent years, however, the interest in and performance level of Tm-doped systems is gradually growing. With the single-channel 2 µm systems already excelling in terms of average power scalability [Gai+18], the established state might soon change.

The novel all-PM-fiber oscillator concepts based on 3x3-coupler-NALMs which have been examined theoretically and experimentally in this work can prove a viable route for simple and standardised generation of ultrashort pulses at various wavelengths without the need for SESAM-technology. The output parameters of the demonstrated Yb- and Tm-based oscillators are summarised in Table 6.1. The

	Repetition Rate (MHz)	Pulse Duration (fs)	Pulse Energy (pJ)
Tm-doped (soliton)	30.3	≈ 540	130
Tm-doped (dispersion managed)	23.3	215	320
Yb-doped	20.8	125	290

Table 6.1: Summary of the output parameters at port 4 of the 3x3-coupler NALM-oscillators in this work.

pulses of the dispersion managed Tm-oscillator represent the shortest pulses in the 2 µm spectral regime directly obtained from an oscillator that is mode-locked by a fiber loop, i.e. NALM or NOLM [Ma+19].

The intrinsic phase characteristics of the 3x3-coupler enable largely relaxed self-starting properties which have, up to now, impeded a prevalent employment of the NALM technology. In the course of this work, an understanding of these characteristics has been attained, which also allows for quantitative predictions and future optimisations of the oscillators. An employment of a second amplifier outside of the NALM has been shown to further enlarge the accessible parameter space and thus increased the oscillators' versatility and flexibility. Moreover, the all-fiber realisation discards any need for and stability risk of free-space component adjustments, which renders the oscillator concepts extremely robust. The obtainable near-parabolic spectral shapes are well suited for a deployment in CPA-systems where large nonlinear phases are generated during amplification. As such pulse sources, consisting of off-the-shelf components, become readily available, the way is paved for Tm-systems with up-scaled output parameters in subsequent amplifier stages to become more widespread.

Still, challenges exist concerning the average and peak power scaling of Tm-doped fiber amplifiers. The unfavourable pumping near 790 nm, where high-power pump diodes are available, generates considerable heat loads and in practise limits the achievable slope efficiencies to <80 % even when cross-relaxation mechanisms are harnessed excessively [JM03]. An effective cooling scheme of the amplifier becomes mandatory in order to allow for operation below critical temperatures. Moreover, the adverse effects of absorption by atmospheric water vapor add a level of complexity to the system layout, which affects both the achievable peak power as well as beam quality, if left unaddressed. A monolithic CPA setup, including an all-fiber oscillator, in which free-space propagation is avoided until after the last amplifier stage, largely reduces the peak power issues and simultaneously enhances the setup's robustness significantly. In this context, the demonstrated all-fiber Tm-CPA-setup is capable of delivering peak powers of 250 MW at a repetition rate of 200 kHz as well as average powers of >100 W at a repetition rate of 2.4 MHz, which represent record values from a monolithic, ultrashort pulse CPA-system in this spectral regime. The average power scaling up to this level is enabled by a thermally conductive silicone that

allows for efficient extraction of the generated waste heat without the need for direct water cooling of the fiber. With this approach, even larger average powers become possible when further increasing the thermal conductivity of the embedding silicone. However, average output powers considerably larger than 10 W will also require either purging of the compressor compartment or shifting the central wavelength further towards 2000 nm in order to avoid the detrimental effects of water vapor absorption. A further scaling of the peak power of the system requires mitigation of nonlinearities which can be achieved directly by using a shorter main amplifier in the range of 2-2.5 m at the cost of a reduced average power at equal pump power or by either temporally or spatially reducing the intensity during amplification.

Bibliography

[Agr07] G. P. Agrawal. *Nonlinear Fiber Optics*. Academic Press, 2007.

[AR19] B. F. Akers and J. A. Reeger. "Numerical simulation of thermal blooming with laser-induced convection". In: *Journal of Electromagnetic Waves and Applications* 33 (2019), pp. 96–106. DOI: https://doi.org/10.1080/09205071.2018.1528183.

[And+93] D. Anderson et al. "Wave-breaking-free pulses in nonlinear-optical fibers". In: *J. Opt. Soc. Am. B* 10 (1993), pp. 1185–1190. DOI: https://doi.org/10.1364/JOSAB.10.001185.

[Bau+09] E. Baumann et al. "High-performance, vibration-immune,fiber-laser frequency comb". In: *Optics Letters* 34 (2009), pp. 638–640. DOI: https://doi.org/10.1364/OL.34.000638.

[BD91] K. J. Blow and N. J. Doran. "Average Soliton Dynamics and the Operation of Soliton Systems with Lumped Amplifiers". In: *IEEE Photonics Technology Letters* 3 (1991), pp. 369–371. DOI: https://doi.org/10.1109/68.82115.

[Bou+20] V. Boulanger et al. "All-fiber Mamyshev oscillator enabled by chirped fiber Bragg gratings". In: *Opt. Lett.* 45 (2020), pp. 3317–3320. DOI: https://doi.org/10.1364/OL.396218.

[Boy20] R. W. Boyd. *Nonlinear Optics*. Academic Press, 2020.

[BH01] D.C. Brown and H.J. Hoffman. “Thermal, stress, and thermo-optic effects in high average power double-clad silica fiber lasers”. In: *IEEE Journal of Quantum Electronics* 37 (2001), pp. 207–217. DOI: https://doi.org/10.1109/3.903070.

[Cai+01] D. Cairns et al. “Mode-locked operation of a figure-of-eight erbium-doped fiber laser based on a 3×3 non-linear loop mirror”. In: Optical Society of America, 2001, CWA48. URL: http://www.osapublishing.org/abstract.cfm?URI=CLEO-2001-CWA48.

[Caj+18] J. Cajzl et al. “Thulium-Doped Silica Fibers with Enhanced Fluorescence Lifetime and Their Application in Ultrafast Fiber Lasers”. In: *Fibers* 6 (2018). DOI: https://doi.org/10.3390/fib6030066.

[Che+12] M. A. Chernysheva et al. “Thulium-doped mode-locked all-fiber laser based on NALM and carbon nanotube saturable absorber”. In: *Opt. Express* 20 (2012), B124–B130. DOI: https://doi.org/10.1364/OE.20.00B124.

[Che+14] M. A. Chernysheva et al. “SESAM and SWCNT Mode-Locked All-Fiber Thulium-Doped Lasers Based on the Nonlinear Amplifying Loop Mirror”. In: *IEEE Journal of Selected Topics in Quantum Electronics* 20 (2014), pp. 448–455. DOI: https://doi.org/10.1109/JSTQE.2014.2313606.

[Chi+12] N. B. Chichkov et al. “Pulse duration and energy scaling of femtosecond all-normal dispersion fiber oscillators”. In: *Optics Express* 20 (2012), pp. 3844–3852. DOI: https://doi.org/10.1364/OE.20.003844.

[CKW07] A. Chong, L. Kuznetsova, and F. W. Wise. “Theoretical optimization of nonlinear chirped-pulse fiber amplifiers”. In: *J. Opt. Soc. Am. B* 24 (Aug. 2007), pp. 1815–1823. DOI: https://doi.org/10.1364/JOSAB.24.001815.

[CRW07] A. Chong, W. Renninger, and F. Wise. “All-normal-dispersion femtosecond fiber laser with pulse energy above 20 nJ”. In: *Optics Letters* 32 (2007), pp. 2408–2410. DOI: https://doi.org/10.1364/OL.32.002408.

[CWW15] A. Chong, L. G Wright, and F. W Wise. "Ultrafast fiber lasers based on self-similar pulse evolution: a review of current progress". In: *Reports on Progress in Physics* 78 (2015), p. 113901. DOI: https://doi.org/10.1088/0034-4885/78/11/113901.

[Cho+06] A. Chong et al. "All-normal-dispersion femtosecond fiber laser". In: *Optics Express* 14 (2006), pp. 10095–10100. DOI: https://doi.org/10.1364/OE.14.010095.

[Col+18] J. M. Cole et al. "Experimental Evidence of Radiation Reaction in the Collision of a High-Intensity Laser Pulse with a Laser-Wakefield Accelerated Electron Beam". In: *Phys. Rev. X* 8 (1 2018), p. 011020. DOI: https://doi.org/10.1103/PhysRevX.8.011020.

[DD94] M. L. Dennis and I. N. Duling. "Experimental Study of Sideband Generation in Femtosecond Fiber Lasers". In: *IEEE Journal of Quantum Electronics* 30 (1994), pp. 1469–147. DOI: https://doi.org/10.1109/3.299472.

[Did+08] N.V. Didenko et al. "Contrast degradation in a chirped-pulse amplifier due to generation of prepulses by postpulses". In: *Opt. Express* 16 (2008), pp. 3178–3190. DOI: https://doi.org/10.1364/OE.16.003178.

[DW88] N. J. Doran and D. Wood. "Nonlinear-optical loop mirror". In: *Optics Letters* 13 (1988), pp. 56–58. DOI: https://doi.org/10.1364/OL.13.000056.

[DB08] C. Dorrer and J. Bromage. "Impact of high-frequency spectral phase modulation on the temporal profile of short optical pulses". In: *Opt. Express* 16 (2008), pp. 3058–3068. DOI: https://doi.org/10.1364/OE.16.003058.

[Dua+20] D. Duan et al. "Approach to high pulse energy emission of the self-starting mode-locked figure-9 fiber laser". In: *Opt. Express* 28 (2020), pp. 33603–33613. DOI: https://doi.org/10.1364/OE.409406.

[Eic05] M. Eichhorn. "Numerical modeling of Tm-doped double-clad fluoride fiber amplifiers". In: *IEEE Journal of Quantum Electronics* 41 (2005), pp. 1574–1581. DOI: https://doi.org/10.1109/JQE.2005.858469.

[EDE04] J. Eichler, L. Dünkel, and B. Eppich. "Die Strahlqualität von Lasern – Wie bestimmt man Beugungsmaßzahl und Strahldurchmesser in der Praxis?" In: *Laser Technik Journal* 1 (2004), pp. 63–66. DOI: https://doi.org/10.1002/latj.200790019.

[Eid+11] T. Eidam et al. "Fiber chirped-pulse amplification system emitting 3.8 GW peak power". In: *Opt. Express* 19 (2011), pp. 255–260. DOI: https://doi.org/10.1364/OE.19.000255.

[Eng+08] M. Engelbrecht et al. "Ultrafast thulium-doped fiber-oscillator with pulse energy of 4.3 nJ". In: *Opt. Lett.* 33 (2008), pp. 690–692. DOI: https://doi.org/10.1364/OL.33.000690.

[FCI96] X. Fang, R. O. Claus, and G. Indebetouw. "Interferometric model for phase analysis in fiber couplers". In: *Applied Optics* 35 (1996), pp. 4510–4515. DOI: https://doi.org/10.1364/AO.35.004510.

[Fer+90] M. E. Fermann et al. "Nonlinear amplifying loop mirror". In: *Optics Letters* 15 (1990), pp. 752–754. DOI: https://doi.org/10.1364/OL.15.000752.

[Fer+00] M.E. Fermann et al. "Self-Similar Propagation and Amplification of Parabolic Pulses in Optical Fibers". In: *Physical Review Letters* 84 (2000), pp. 6010–6013. DOI: https://doi.org/10.1103/PhysRevLett.84.6010.

[Fin+06] C. Finot et al. "Parabolic pulse evolution in normally dispersive fiber amplifiers preceding the similariton formation regime". In: *Opt. Express* 14 (2006), pp. 3161–3170. DOI: https://doi.org/10.1364/OE.14.003161.

[Fin+07] C. Finot et al. "Parabolic pulse generation through passive nonlinear pulse reshaping in a normally dispersive two segment fiber device". In: *Opt. Express* 15 (2007), pp. 852–864. DOI: https://doi.org/10.1364/OE.15.000852.

[FMG84] R. L. Fork, O. E. Martinez, and J. P. Gordon. "Negative dispersion using pairs of prisms". In: *Opt. Lett.* 9 (1984), pp. 150–152. DOI: https://doi.org/10.1364/OL.9.000150.

[FL06] G. P. Frith and D. G. Lancaster. “Power scalable and efficient 790-nm pumped Tm3+-doped fiber lasers”. In: *Fiber Lasers III: Technology, Systems, and Applications*. Ed. by Andrew J. W. Brown et al. Vol. 6102. International Society for Optics and Photonics. SPIE, 2006, pp. 44–53. DOI: https://doi.org/10.1117/12.660932.

[Fu+17] W. Fu et al. “Limits of femtosecond fiber amplification by parabolic pre-shaping”. In: *J. Opt. Soc. Am. B* 34 (2017), A37–A42. DOI: https://doi.org/10.1364/JOSAB.34.000A37.

[Fu+18] W. Fu et al. “Several new directions for ultrafast fiber lasers [Invited]”. In: *Opt. Express* 26 (2018), pp. 9432–9463. DOI: https://doi.org/10.1364/OE.26.009432.

[Gai+17] C. Gaida et al. “90 fs pulses with GW peak power from a high repetition rate Tm-doped fiber CPA system”. In: *Laser Congress 2017 (ASSL, LAC)*. Optical Society of America, 2017, ATh3A.5. DOI: https://doi.org/10.1364/ASSL.2017.ATh3A.5.

[Gai+18] C. Gaida et al. “Ultrafast thulium fiber laser system emitting more than 1kW of average power”. In: *Opt. Lett.* 43 (2018), pp. 5853–5856. DOI: https://doi.org/10.1364/OL.43.005853.

[Gai+21] C. Gaida et al. “Transverse mode instability and thermal effects in thulium-doped fiber amplifiers under high thermal loads”. In: *Opt. Express* 29 (2021), pp. 14963–14973. DOI: https://doi.org/10.1364/OE.421954.

[Gal+01] A. Galvanauskas et al. “Generation of high-energy femtosecond pulses in multimode-core Yb-fiber chirped-pulse amplification systems”. In: *Opt. Lett.* 26 (2001), pp. 935–937. DOI: https://doi.org/10.1364/OL.26.000935.

[GM08] R. R. Gattass and E. Mazur. “Femtosecond laser micromachining in transparent materials”. In: *Nature Photonics* 2 (2008), pp. 219–225. DOI: https://doi.org/10.1038/nphoton.2008.47.

[Geb+15] M. Gebhardt et al. “Impact of atmospheric molecular absorption on the temporal and spatial evolution of ultra-short optical pulses”. In: *Opt. Express* 23 (2015), pp. 13776–13787. DOI: https://doi.org/10.1364/OE.23.013776.

[Gor86] J. P. Gordon. “Theory of the soliton self-frequency shift”. In: *Opt. Lett.* 11 (1986), pp. 662–664. DOI: https://doi.org/10.1364/OL.11.000662.

[Gra+22] Florian Graf et al. “Femtosecond fiber oscillator based on a 3× 3-coupler-NALM: numerical model and realizations at 1 and 2 μm”. In: *Optics express* 30 (2022), pp. 12555–12564. DOI: https://doi.org/10.1364/OE.446457.

[Hän+18] W. Hänsel et al. “All polarization-maintaining fiber laser architecture for robust femtosecond pulse generation”. In: *Exploring the World with the Laser*. Springer, 2018, pp. 331–340.

[Hän+13] W. Hänsel et al. “Laser with nonlinear optical loop mirror”. In: *Eur. Pat. Appl. EP 2637265* (2013).

[Hau75a] H. A. Haus. “Theory of mode locking with a fast saturable absorber”. In: *Journal of Applied Physics* 46 (1975), pp. 3049–3058. DOI: https://doi.org/10.1063/1.321997.

[Hau75b] H. A. Haus. “Theory of mode locking with a slow saturable absorber”. In: *IEEE Journal of Quantum Electronics* 11 (1975), pp. 736–746. DOI: https://doi.org/10.1109/JQE.1975.1068922.

[Hau+95] H. A. Haus et al. “Stretched-pulse additive pulse mode-locking in fiber ring lasers: theory and experiment”. In: *IEEE Journal of Quantum Electronics* 31 (1995), pp. 591–598. DOI: https://doi.org/10.1109/3.364417.

[Hau00] H.A. Haus. “Mode-locking of lasers”. In: *IEEE Journal of Selected Topics in Quantum Electronics* 6 (2000), pp. 1173–1185. DOI: https://doi.org/10.1109/2944.902165.

[Hax+11] F. Haxsen et al. “Hybrid mode-locked thulium soliton fiber laser”. In: *IEEE Photonic Society 24th Annual Meeting*. 2011, pp. 885–886. DOI: https://doi.org/10.1109/PHO.2011.6110842.

[Hay+00] R.A. Hayward et al. “Efficient cladding-pumped Tm-doped silica fibre laser with high power singlemode output at 2 µm”. In: *Electronics Letters* 36 (2000), pp. 711–712. DOI: https://doi.org/10.1049/el:20000577.

[Hor+16] M. Hornung et al. “54 J pulses with 18 nm bandwidth from a diode-pumped chirped-pulse amplification laser system”. In: *Opt. Lett.* 41 (2016), pp. 5413–5416. DOI: https://doi.org/10.1364/OL.41.005413.

[Hoy+14] C. Hoy et al. “Clinical ultrafast laser surgery: Recent advances and future directions”. In: *IEEE Journal on Selected Topics in Quantum Electronics* 20 (2014). DOI: https://doi.org/10.1109/JSTQE.2013.2287098.

[Hug68] G.R. Huggett. “MODE-LOCKING OF CW LASERS BY REGENERATIVE RF FEEDBACK”. In: *Applied Physics Letters* 13 (1968), pp. 186–187.

[Ipp94] E. P. Ippen. “Principles of Passive Mode Locking”. In: *Appl. Phys. B* 58 (1994), pp. 159–170. DOI: https://doi.org/10.1007/BF01081309.

[IHL89] E. P. Ippen, H. A. Haus, and L. Y. Liu. “Additive pulse mode locking”. In: *J. Opt. Soc. Am. B* 6 (1989), pp. 1736–1745. DOI: https://doi.org/10.1364/JOSAB.6.001736.

[Jac04] S. D. Jackson. “Cross relaxation and energy transfer upconversion processes relevant to the functioning of 2 µm Tm3+-doped silica fibre lasers”. In: *Optics Communications* 230 (2004), pp. 197–203. DOI: https://doi.org/10.1016/j.optcom.2003.11.045.

[JK99] S. D. Jackson and T. A. King. “Theoretical Modeling of Tm-Doped Silica Fiber Lasers”. In: *J. Lightwave Technol.* 17 (1999), p. 948.

[JM03] S. D. Jackson and S. Mossman. “Efficiency dependence on the Tm3+ and Al3+ concentrations for Tm3+-doped silica double-clad fiber lasers”. In: *Appl. Opt.* 42 (2003), pp. 2702–2707. DOI: https://doi.org/10.1364/AO.42.002702.

[Jan+12a] F. Jansen et al. “High-power very large mode-area thulium-doped fiber laser”. In: *Opt. Lett.* 37 (2012), pp. 4546–4548. DOI: https://doi.org/10.1364/OL.37.004546.

[Jan+12b] F. Jansen et al. “Thermally induced waveguide changes in active fibers”. In: *Opt. Express* 20 (2012), pp. 3997–4008. DOI: https://doi.org/10.1364/OE.20.003997.

[JSL20] C. Jauregui, C. Stihler, and J. Limpert. “Transverse mode instability”. In: *Adv. Opt. Photon.* 12 (2020), pp. 429–484. DOI: https://doi.org/10.1364/AOP.385184.

[Jau+12] C. Jauregui et al. “Physical origin of mode instabilities in high-power fiber laser systems”. In: *Opt. Express* 20 (2012), pp. 12912–12925. DOI: https://doi.org/10.1364/OE.20.012912.

[Jau+15] C. Jauregui et al. “Simplified modelling the mode instability threshold of high power fiber amplifiers in the presence of photodarkening”. In: *Opt. Express* 23 (2015), pp. 20203–20218. DOI: https://doi.org/10.1364/OE.23.020203.

[Jia+16] T. Jiang et al. “All PM Fiber Laser Mode Locked With a Compact Phase Biased Amplifier Loop Mirror”. In: *IEEE Photonics Technologies Letters* 28 (2016), pp. 1786–1789. DOI: https://doi.org/10.1109/LPT.2016.2572167.

[KT93] D.J. Kane and R. Trebino. “Characterization of arbitrary femtosecond pulses using frequency-resolved optical gating”. In: *IEEE Journal of Quantum Electronics* 29 (1993), pp. 571–579. DOI: https://doi.org/10.1109/3.199311.

[Kar+01] N. Karasawa et al. “Optical pulse compression to 5.0 fs by use of only a spatial light modulator for phase compensation”. In: *J. Opt. Soc. Am. B* 18 (2001), pp. 1742–1746. DOI: https://doi.org/10.1364/JOSAB.18.001742.

[Kel+96] U. Keller et al. “Semiconductor saturable absorber mirrors (SESAM’s) for femtosecond to nanosecond pulse generation in solid-state lasers”. In: *IEEE Journal of Selected Topics in Quantum Electronics* 2 (1996), pp. 435–453. DOI: https://doi.org/10.1109/2944.571743.

[Kel92] S. M. J. Kelly. “Characteristic sideband instability of periodically amplified average soliton”. In: *Electronics Letters* 28 (1992), pp. 806–807. DOI: https://doi.org/10.1049/el:19920508.

[Kel+91] S. M. J. Kelly et al. “Average soliton dynamics of a high-gain erbium fiber laser”. In: *Optics Letters* 16 (1991), pp. 1337–1339. DOI: https://doi.org/10.1364/OL.16.001337.

[KW09] K. Kieu and F. W. Wise. “Soliton Thulium-Doped Fiber Laser With Carbon Nanotube Saturable Absorber”. In: *IEEE Photonics Technology Letters* 21 (2009), pp. 128–130. DOI: https://doi.org/10.1109/LPT.2008.2008727.

[Kih+96] M. Kihara et al. “Characteristics of thermally expanded core fiber”. In: *Journal of Lightwave Technology* 14 (1996), pp. 2209–2214. DOI: https://doi.org/10.1109/50.541209.

[Kim+19] D. Kim et al. “Polarization-maintaining nonlinear-amplifying loop-mirror mode-locked fiber laser based on a 3x3 coupler”. In: *Optics Letters* 44 (2019), pp. 1068–1071. DOI: https://doi.org/10.1364/OL.44.001068.

[KCJ20] S. Kim, Y.-H. Cha, and D.-Y. Jeong. “Development of a Femtosecond High-Power Ytterbium-doped Fiber Laser System and Study on Spiky Spectral Modulation in Highly Nonlinear Chirped-Pulse Fiber Amplifiers”. In: *Journal of the Korean Physical Society* 77 (2020), pp. 1135–1142. DOI: https://doi.org/10.3938/jkps.77.1135.

[Kle+14] A. Klenke et al. “22 GW peak-power fiber chirped-pulse-amplification system”. In: *Opt. Lett.* 39 (2014), pp. 6875–6878. DOI: https://doi.org/10.1364/OL.39.006875.

[KKG00] J. P. Koplow, D. A. V. Kliner, and L. Goldberg. “Single-mode operation of a coiled multimode fiber amplifier”. In: *Opt. Lett.* 25 (2000), pp. 442–444. DOI: https://doi.org/10.1364/OL.25.000442.

[Kou07] D. Kouznetsov. “Broadband laser materials and the McCumber relation”. In: *Chin. Opt. Lett.* 5 (2007), S240–S242. URL: http://www.osapublishing.org/col/abstract.cfm?URI=col-5-101-S240.

[Kri65] M.A. Krivoglaz. “Theory of broadening of spectral lines and nonradiative transitions in systems with weak coupling”. In: *Soviet Physics JETP* 21 (1965), pp. 204–214.

[Kru+02] V. I. Kruglov et al. “Self-similar propagation of parabolic pulses in normal-dispersion fiber amplifiers”. In: *J. Opt. Soc. Am. B* 19 (2002), pp. 461–469. DOI: https://doi.org/10.1364/JOSAB.19.000461.

[LL18] J. Lee and J. H. Lee. “Femtosecond Tm-Ho co-doped fiber laser using a bulk-structured Bi2Se3 topological insulator”. In: *Chinese Physics B* 27 (2018), p. 094219. DOI: https://doi.org/10.1088/1674-1056/27/9/094219.

[Lee+17] J. Lee et al. “All-fiberized, femtosecond laser at 1912 nm using a bulk-like MoSe2 saturable absorber”. In: *Opt. Mater. Express* 7 (2017), pp. 2968–2979. DOI: https://doi.org/10.1364/OME.7.002968.

[Li+14] J. Li et al. “All-fiber passively mode-locked Tm-doped NOLM-based oscillator operating at 2-µm in both soliton and noisy-pulse regimes”. In: *Opt. Express* 22 (2014), pp. 7875–7882. DOI: https://doi.org/10.1364/OE.22.007875.

[Li+15] L. Li et al. “1 mJ nanosecond all-fiber thulium-doped fiber laser at 2.05 µm”. In: *Opt. Express* 23 (2015), pp. 18098–18105. DOI: https://doi.org/10.1364/OE.23.018098.

[Lim+06] J. Limpert et al. “High-power ultrafast fiber laser systems”. In: *IEEE Journal of Selected Topics in Quantum Electronics* 12 (2006), pp. 233–244. DOI: https://doi.org/10.1109/JSTQE.2006.872729.

[Lim+12] J. Limpert et al. “Yb-doped large-pitch fibres: effective single-mode operation based on higher-order mode delocalisation”. In: *Light: Science and Applications* 1 (2012). DOI: https://doi.org/10.1038/lsa.2012.8.

[Liu+19] W. Liu et al. “Femtosecond Mamyshev oscillator with 10-MW-level peak power”. In: *Optica* 6 (2019), pp. 194–197. DOI: https://doi.org/10.1364/OPTICA.6.000194.

[LDM97] X. Liu, D. Du, and G. Mourou. “Laser ablation and micromachining with ultrashort laser pulses”. In: *IEEE Journal of Quantum Electronics* 33 (1997), pp. 1706–1716. DOI: https://doi.org/10.1109/3.631270.

[Liu+16] Y. Liu et al. “Generation of 33 fs 93.5 W average power pulses from a third-order dispersion managed self-similar fiber amplifier”. In: *Opt. Express* 24 (2016), pp. 10939–10945. DOI: https://doi.org/10.1364/OE.24.010939.

[Liu+17] Z. Liu et al. “Megawatt peak power from a Mamyshev oscillator”. In: *Optica* 4 (2017), pp. 649–654. DOI: https://doi.org/10.1364/OPTICA.4.000649.

[Ma+19] J. Ma et al. “Review of mid-infrared mode-locked laser sources in the 2.0 µm–3.5 µm spectral region”. In: *Applied Physics Reviews* 6 (2019), p. 021317. DOI: https://doi.org/10.1063/1.5037274.

[MBP13] A. Macchi, M. Borghesi, and M. Passoni. “Ion acceleration by superintense laser-plasma interaction”. In: *Rev. Mod. Phys.* 85 (2 2013), pp. 751–793. DOI: https://doi.org/10.1103/RevModPhys.85.751.

[Mam98] P.V. Mamyshev. “All-optical data regeneration based on self-phase modulation effect”. In: *24th European Conference on Optical Communication. ECOC ’98 (IEEE Cat. No.98TH8398)*. Vol. 1. 1998, pp. 475–476. DOI: https://doi.org/10.1109/ECOC.1998.732666.

[Mar09] J. R. Marciante. “Gain Filtering for Single-Spatial-Mode Operation of Large-Mode-Area Fiber Amplifiers”. In: *IEEE Journal of Selected Topics in Quantum Electronics* 15 (2009), pp. 30–36. DOI: https://doi.org/10.1109/JSTQE.2008.2010272.

[Mar77] D. Marcuse. “Loss Analysis of Single-Mode Fiber Splices”. In: *Bell Labs Technical Journal* (1977). DOI: https://doi.org/10.1002/j.1538-7305.1977.tb00534.x.

[Mar87] O. Martinez. “3000 times grating compressor with positive group velocity dispersion: Application to fiber compensation in 1.3-1.6 µm region”. In: *IEEE Journal of Quantum Electronics* 23 (1987), pp. 59–64. DOI: https://doi.org/10.1109/JQE.1987.1073201.

[McC64] D. E. McCumber. “Einstein Relations Connecting Broadband Emission and Absorption Spectra”. In: *Phys. Rev.* 136 (1964), A954–A957. DOI: https://doi.org/10.1103/PhysRev.136.A954.

[Mih+99] S.J. Mihailov et al. “Comparison of fiber Bragg grating dispersion-compensators made with holographic and e-beam written phase masks”. In: *IEEE Photonics Technology Letters* 11 (1999), pp. 572–574. DOI: https://doi.org/10.1109/68.759402.

[MK79] S. Miller and I. Kaminow. *Optical Fiber Telecommunications*. Academic Press, 1979.

[Min+12] I. Mingareev et al. “Welding of polymers using a 2 µm thulium fiber laser”. In: *Optics and Laser Technology* 44 (2012), pp. 2095–2099. DOI: https://doi.org/10.1016/j.optlastec.2012.03.020.

[MM86] F. M. Mitschke and L. F. Mollenauer. “Discovery of the soliton self-frequency shift”. In: *Opt. Lett.* 11 (1986), pp. 659–661. DOI: https://doi.org/10.1364/OL.11.000659.

[Neg+15] J.-P. Negel et al. “Ultrafast thin-disk multipass laser amplifier delivering 1.4 kW (4.7 mJ, 1030 nm) average power converted to 820 W at 515 nm and 234 W at 343 nm”. In: *Opt. Express* 23 (2015), pp. 21064–21077. DOI: https://doi.org/10.1364/OE.23.021064.

[Nej+05] A. H. Nejadmalayeri et al. “Inscription of optical waveguides in crystalline silicon by mid-infrared femtosecond laser pulses”. In: *Opt. Lett.* 30 (2005), pp. 964–966. DOI: https://doi.org/10.1364/OL.30.000964.

[Nel+97] L.E. Nelson et al. “Ultrashort-pulse fiber ring lasers”. In: *Appl. Phys. B* 65 (1997), pp. 277–294. DOI: https://doi.org/10.1007/s003400050273.

[NA06] J. W. Nicholson and M. Andrejco. “A polarization maintaining, dispersion managed, femtosecond figure-eight fiberlaser”. In: *Optics Express* 14 (2006), pp. 8160–8167. DOI: https://doi.org/10.1364/OE.14.008160.

[Nie+11] B. Nie et al. “Generation of 42-fs and 10-nJ pulses from a fiber laser with self-similar evolution in the gain segment”. In: *Opt. Express* 19 (2011), pp. 12074–12080. DOI: https://doi.org/10.1364/OE.19.012074.

[NOS86] J. Noda, K. Okamoto, and Y. Sasaki. “Polarization-maintaining fibers and their applications”. In: *Journal of Lightwave Technology* 4 (1986), pp. 1071–1089. DOI: https://doi.org/10.1109/JLT.1986.1074847.

[OCI10] B. Oktem, C.Ülgüdür, and F.Ö. Ilday. "Soliton–similariton fibre laser". In: *Nature Photonics* 4 (2010), pp. 307–311. DOI: https://doi.org/10.1038/nphoton.2010.33.

[Ott+15] H.-J. Otto et al. "Impact of photodarkening on the mode instability threshold". In: *Opt. Express* 23 (2015), pp. 15265–15277. DOI: https://doi.org/10.1364/OE.23.015265.

[Pan+92] N. Pandit et al. "Characteristic Instability of Fibre Loop Soliton Lasers". In: *Electronic Letters* 28 (1992), pp. 455–457. DOI: https://doi.org/10.1049/el:19920287.

[PI95] B. Peng and T. Izumitani. "Optical properties, fluorescence mechanisms and energy transfer in Tm3+, Ho3+ and Tm3+ -Ho3+ doped near-infrared laser glasses, sensitized by Yb3+". In: *Optical Materials* 4 (1995), pp. 797–810. DOI: https://doi.org/10.1016/0925-3467(95)00032-1.

[Pet+04] P. Peterka et al. "Theoretical modelling of S-band thulium-doped silica fibre amplifiers". In: *Optical and Quantum Electronics* 36 (2004), pp. 201–212. DOI: https://doi.org/10.1023/B:OQEL.0000015640.82309.7d.

[Pet+92] R. R. Petrin et al. "Spectral dynamics of laser-pumped Y3Al5O12:Tm,Ho lasers". In: *Optical Materials* 1 (1992), pp. 111–124. DOI: https://doi.org/10.1016/0925-3467(92)90008-B.

[Pie89] J. Pietzsch. "Scattering Matrix Analysis of 3 x 3 Fiber Couplers". In: *Journal of Lightwave Technology* 7 (1989), pp. 303–307. DOI: https://doi.org/10.1109/50.17771.

[Pri82] R. G. Priest. "Analysis of Fiber Interferometer Utilizing 3x3 Fiber Coupler". In: *IEEE Transactions on Microwave Theory and Techniques* 30 (1982), pp. 1589–1591. DOI: https://doi.org/10.1109/TMTT.1982.1131294.

[Pul+15] B. Pulford et al. "400-W near diffraction-limited single-frequency all-solid photonic bandgap fiber amplifier". In: *Opt. Lett.* 40 (2015), pp. 2297–2300. DOI: https://doi.org/10.1364/OL.40.002297.

[RCW07] W. H. Renninger, A. Chong, and F. W. Wise. “Dissipative solitons in normal-dispersion fiber lasers”. In: *Physical Review A* 77 (2007), p. 023814. DOI: https://doi.org/10.1103/PhysRevA.77.023814.

[RCW10] W. H. Renninger, A. Chong, and F. W. Wise. “Self-similar pulse evolution in an all-normal-dispersion laser”. In: *Phys. Rev. A* 82 (2010), p. 021805. DOI: https://doi.org/10.1103/PhysRevA.82.021805.

[Rep+19] P. Repgen et al. “Sub-50 fs, µJ-level pulses from a Mamyshev oscillator–amplifier system”. In: *Opt. Lett.* 44 (2019), pp. 5973–5976. DOI: https://doi.org/10.1364/OL.44.005973.

[Rot+13] L.S. Rothman et al. “The HITRAN2012 molecular spectroscopic database”. In: *Journal of Quantitative Spectroscopy and Radiative Transfer* 130 (2013), pp. 4–50. DOI: https://doi.org/10.1016/j.jqsrt.2013.07.002.

[Rud+12] C. W. Rudy et al. “Thulium-doped Germanosilicate Mode-locked Fiber Lasers”. In: Optical Society of America, 2012, FTh4A.4. DOI: https://doi.org/10.1364/FILAS.2012.FTh4A.4.

[Rus+10] P. Russbueldt et al. “Compact diode-pumped 1.1 kW Yb:YAG Innoslab femtosecond amplifier”. In: *Opt. Lett.* 35 (2010), pp. 4169–4171. DOI: https://doi.org/10.1364/OL.35.004169.

[Rus03] P. Russell. “Photonic Crystal Fibers”. In: *Science* 299 (2003), pp. 358–362. DOI: https://doi.org/10.1126/science.1079280.

[SBG17] I. Samartsev, A. Bordenyuk, and V. Gapontsev. “Environmentally stable seed source for high power ultrafast laser”. In: *Components and Packaging for Laser Systems III*. Vol. 10085. SPIE, 2017, pp. 201–209. DOI: https://doi.org/10.1117/12.2250641.

[SC07] R. T. Schermer and J. H. Cole. “Improved Bend Loss Formula Verified for Optical Fiber by Simulation and Experiment”. In: *IEEE Journal of Quantum Electronics* 43 (2007), pp. 899–909. DOI: https://doi.org/10.1109/JQE.2007.903364.

[Sch+08a] D. N. Schimpf et al. “Decrease of pulse-contrast in nonlinear chirped-pulse amplification systems due to high-frequency spectral phase ripples”. In: *Opt. Express* 16 (June 2008), pp. 8876–8886. DOI: https://doi.org/10.1364/OE.16.008876.

[Sch+08b] D. N. Schimpf et al. “The impact of spectral modulations on the contrast of pulses of nonlinear chirped-pulse amplification systems”. In: *Opt. Express* 16 (July 2008), pp. 10664–10674. DOI: https://doi.org/10.1364/OE.16.010664.

[Sch+09] D. N. Schimpf et al. “Self-phase modulation compensated by positive dispersion in chirped-pulse systems”. In: *Opt. Express* 17 (2009), pp. 4997–5007. DOI: https://doi.org/10.1364/OE.17.004997.

[Set+04] S.Y. Set et al. “Ultrafast fiber pulsed lasers incorporating carbon nanotubes”. In: *IEEE Journal of Selected Topics in Quantum Electronics* 10 (2004), pp. 137–146. DOI: https://doi.org/10.1109/JSTQE.2003.822912.

[Sha+05] L. Shah et al. “High energy femtosecond Yb cubicon fiber amplifier”. In: *Opt. Express* 13 (2005), pp. 4717–4722. DOI: https://doi.org/10.1364/OPEX.13.004717.

[Sid+18] P. Sidorenko et al. “Self-seeded, multi-megawatt, Mamyshev oscillator”. In: *Opt. Lett.* 43 (2018), pp. 2672–2675. DOI: https://doi.org/10.1364/OL.43.002672.

[Sil62] R. H. Silsbee. “Thermal Broadening of the Mössbauer Line and of Narrow-Line Electronic Spectra in Solids”. In: *Phys. Rev.* 128 (1962), pp. 1726–1733. DOI: https://doi.org/10.1103/PhysRev.128.1726.

[Sin+18] A. Sincore et al. “Experimental investigation on varying spectral bandwidth when amplifying a pulsed superfluorescent 2-µm source in Tm:fiber”. In: *Fiber Lasers XV: Technology and Systems*. Ed. by I. Hartl and A. L. Carter. International Society for Optics and Photonics. SPIE, 2018, pp. 102–108. DOI: https://doi.org/10.1117/12.2290217.

[SS11] A. V. Smith and J. J. Smith. “Mode instability in high power fiber amplifiers”. In: *Opt. Express* 19 (2011), pp. 10180–10192. DOI: https://doi.org/10.1364/OE.19.010180.

[SS16] A. V. Smith and J. J. Smith. “Mode instability thresholds for Tm-doped fiber amplifiers pumped at 790 nm”. In: *Opt. Express* 24 (2016), pp. 975–992. DOI: https://doi.org/10.1364/OE.24.000975.

[Smi77] D.C. Smith. “High-power laser propagation: Thermal blooming”. In: *Proceedings of the IEEE* 65 (1977), pp. 1679–1714. DOI: https://doi.org/10.1109/PROC.1977.10809.

[SL83] A. W. Snyder and J. Love. *Optical Waveguide Theory*. Springer, Boston, MA, 1983. DOI: https://doi.org/10.1007/978-1-4613-2813-1.

[Sob+17] G. Soboń et al. “Generation of sub-100 fs pulses tunable from 1700 to 2100 nm from a compact frequency-shifted Er-fiber laser”. In: *Photon. Res.* 5 (2017), pp. 151–155. DOI: https://doi.org/10.1364/PRJ.5.000151.

[Sot+15] J. Sotor et al. “Ultrafast thulium-doped fiber laser mode locked with black phosphorus”. In: *Opt. Lett.* 40 (2015), pp. 3885–3888. DOI: https://doi.org/10.1364/OL.40.003885.

[Sot+17] J. Sotor et al. “All-polarization-maintaining, stretched-pulse Tm-doped fiber laser, mode-locked by a graphene saturable absorber”. In: *Opt. Lett.* 42 (2017), pp. 1592–1595. DOI: https://doi.org/10.1364/OL.42.001592.

[SO99] J. M. Sousa and O. G. Okhotnikov. “Multimode Er-doped fiber for single-transverse-mode amplification”. In: *Applied Physics Letters* 74 (1999), pp. 1528–1530. DOI: https://doi.org/10.1063/1.123605.

[SM85] D. Strickland and G. Mourou. “Compression of amplified chirped optical pulses”. In: *Optics Communications* 55 (1985), pp. 447–449. DOI: https://doi.org/10.1016/0030-4018(85)90151-8.

[Stu+14] F. Stutzki et al. “Designing advanced very-large-mode-area fibers for power scaling of fiber-laser systems”. In: *Optica* 1 (2014), pp. 233–242. DOI: https://doi.org/10.1364/OPTICA.1.000233.

[Sve10] O. Svelto. *Principles of Lasers*. Springer, 2010.

[Tam+93] K. Tamura et al. “77-fs pulse generation from a stretched-pulse mode-locked all-fiber ring laser”. In: *Optics Letters* 18 (1993), pp. 1080–1082. DOI: https://doi.org/10.1364/OL.18.001080.

[Tan+05] D. Y. Tang et al. “Mechanism of multisoliton formation and soliton energy quantization in passively mode-locked fiber lasers”. In: *Phys. Rev. A* 72 (2005), p. 043816. DOI: https://doi.org/10.1103/PhysRevA.72.043816.

[TSJ85] W. J. Tomlinson, R. H. Stolen, and A. M. Johnson. “Optical wave breaking of pulses in nonlinear optical fibers”. In: *Opt. Lett.* 10 (1985), pp. 457–459. DOI: https://doi.org/10.1364/OL.10.000457.

[Tre69] E. Treacy. “Optical pulse compression with diffraction gratings”. In: *IEEE Journal of Quantum Electronics* 5 (1969), pp. 454–458. DOI: https://doi.org/10.1109/JQE.1969.1076303.

[TBF12] S. K. Turitsyn, B. G. Bale, and M. P. Fedoruk. “Dispersion-managed solitons in fibre systems and lasers”. In: *Physics Reports* 521 (2012), pp. 135–203. DOI: https://doi.org/10.1016/j.physrep.2012.09.004.

[Tur+08] G. Turri et al. “Temperature-dependent spectroscopic properties of Tm3+ in germanate, silica, and phosphate glasses: A comparative study”. In: *Journal of Applied Physics* 103 (2008), pp. 093104–093104. DOI: https://doi.org/10.1063/1.2912952.

[VRR14] K. Viskontas, K. Regelskis, and N. Rusteika. “Slow and fast optical degradation of the SESAM for fiber laser mode-locking at 1 µm”. In: *Lithuanian Journal of Physics* 54 (2014), pp. 127–135. DOI: https://doi.org/10.3952/physics.v54i3.2951.

[WYL13a] P. Wan, L.-M. Yang, and J. Liu. “All fiber-based Yb-doped high energy, high power femtosecond fiber lasers”. In: *Opt. Express* 21 (2013), pp. 29854–29859. DOI: https://doi.org/10.1364/OE.21.029854.

[WYL13b] P. Wan, L.-M. Yang, and J. Liu. “High power 2 µm femtosecond fiber laser”. In: *Opt. Express* 21 (2013), pp. 21374–21379. DOI: https://doi.org/10.1364/OE.21.021374.

[WYL13c] P. Wan, L.-M. Yang, and J. Liu. "High pulse energy 2 µm femtosecond fiber laser". In: *Opt. Express* 21 (2013), pp. 1798–1803. DOI: https://doi.org/10.1364/OE.21.001798.

[WRD12] B. Ward, C. Robin, and I. Dajani. "Origin of thermal modal instabilities in large mode area fiber amplifiers". In: *Opt. Express* 20 (2012), pp. 11407–11422. DOI: https://doi.org/10.1364/OE.20.011407.

[WBR00] B. R. Washburn, J. A. Buck, and S. E. Ralph. "Transform-limited spectral compression due to self-phase modulation in fibers". In: *Opt. Lett.* 25 (2000), pp. 445–447. DOI: https://doi.org/10.1364/OL.25.000445.

[Wei+92] A.M. Weiner et al. "Programmable shaping of femtosecond optical pulses by use of 128-element liquid crystal phase modulator". In: *IEEE Journal of Quantum Electronics* 28 (1992), pp. 908–920. DOI: https://doi.org/10.1109/3.135209.

[WN69] J. H. Wray and J. T. Neu. "Refractive Index of Several Glasses as a Function of Wavelength and Temperature". In: *J. Opt. Soc. Am.* 59 (1969), pp. 774–776. DOI: https://doi.org/10.1364/JOSA.59.000774.

[Zho+05] S. Zhou et al. "Compensation of nonlinear phase shifts with third-order dispersion in short-pulse fiber amplifiers". In: *Opt. Express* 13 (2005), pp. 4869–4877. DOI: https://doi.org/10.1364/OPEX.13.004869.

Danksagung (Acknowledgements)

An dieser Stelle möchte ich mich bei all den Menschen bedanken, die mich auf meinem Weg unterstützt haben und damit zum Gelingen dieser Arbeit beigetragen haben.

Mein Dank gilt dabei zuerst Thomas Dekorsy, der diese Arbeit hervorragend betreut hat und dabei immer für mich erreichbar war. Weiterhin danke ich Marc Eichhorn für die Übernahme des Zweitgutachtens.

Seitens Trumpf, möchte ich mich bei Aleksander Budnicki für die Möglichkeit bedanken, meine Arbeit in einem exzellenten Umfeld durchführen zu können, sowie für die Betreuung und die zahlreichen technischen Diskussionen. Weiterhin möchte ich bei meinen Kollegen Holger Diekamp, Florian Jansen, Sören Kumkar, Maike Proßotowicz und Raphael Scelle bedanken, die maßgeblich zu diesem Umfeld beigetragen haben und dafür gesorgt haben, dass mir die Zeit während und abseits der Arbeit in angenehmer Erinnerung bleiben wird. Ebenso möchte ich mich bei allen anderen Kollegen und Mitarbeitern am Standort Schramberg für die gute Zusammenarbeit bedanken.

Ein besonderer Dank gilt meinen Eltern Andrea und Herbert und meinen Geschwistern Tatjana, Fabian und Julian für die Unterstützung und Ermutigung weit über das Studium hinaus.

Curriculum Vitae

Personal Details

Name:	Florian Graf	Nationality:	German
Date of birth:	11.12.1990	Place of birth:	Freudenstadt

Education

Jun 2010	Abitur, Gymnasium Dornstetten

Community Service

Nov 2010 - Sep 2011	Volunteer for the German Red Cross

University Education

Oct 2011 - Oct 2015	Studies of physics, Karlsruhe Institute of Technology degree: Bachelor of Science
Nov 2015 - Mar 2018	Studies of physics, Karlsruhe Institute of Technology degree: Master of Science Thesis title: *Electromagnetically Dual Nanostructures for Enhanced Circular Dichroism Spectroscopy*
Jul 2018 - Dec 2021	Industrial Ph.D. student, University of Stuttgart in corporation with Trumpf Laser GmbH

Professional Affiliations

Jan 2022 - today	Developer of ultrashort pulse fiber lasers at Trumpf Laser GmbH, Schramberg